Search for the Decay $B^+ \to a_1^+ K^{*0}$ at the *BABAR* Experiment

Fakultät Physik
der Technischen Universität Dortmund

DISSERTATION

zur Erlangung des akademischen Grades eines
Doktors der Naturwissenschaften

vorgelegt von
Diplom-Physiker Jesko Friedrich Merkel

Dortmund
März 2009

Gutachter: Prof. Dr. Bernhard Spaan
Priv.-Doz. Dr. Reiner Klingenberg.

Eingereicht am: 6. März 2009

Abstract

The thesis presents the procedure and the result of a search for the decay $B^{\pm} \to a_1^{\pm} K^{*0}$. The data, collected with the *BABAR* detector at the Stanford Linear Accelerator Center, represent 465 million $B\overline{B}$ pairs produced in e^+e^- annihilation at the $\Upsilon(4S)$ energy. The result for the branching fraction is:

$$\mathcal{B}(B^+ \to a_1^+ K^{*0}) \times \mathcal{B}(a_1^+ \to \pi^+\pi^-\pi^+) = (0.7^{+0.5+0.7}_{-0.4-0.7}) \times 10^{-6},$$

corresponding to an upper limit at 90% confidence level of 1.6×10^{-6}. The first uncertainty quoted is statistical, the second systematic. The method used to obtain the results is a maximum likelihood fit technique with different discriminating variables to distinguish between signal and background components.

Kurzfassung

In dieser Arbeit werden die Prozedur und die Resultate für die Suche nach dem Zerfall $B^{\pm} \to a_1^{\pm} K^{*0}$ vorgestellt. Die zugrunde liegenden Daten wurden mit dem *BABAR* Detektor am Stanford Linear Accelerator Center in e^+e^- Vernichtung bei einer Energie enstprechend der $\Upsilon(4S)$ Resonanz aufgezeichnet. Die Daten entsprechen 465 Millionen $B\overline{B}$ Paaren. Das Ergebnis für das Verzweigungsverhältnis ist:

$$\mathcal{B}(B^+ \to a_1^+ K^{*0}) \times \mathcal{B}(a_1^+ \to \pi^+\pi^-\pi^+) = (0.7^{+0.5+0.7}_{-0.4-0.7}) \times 10^{-6}.$$

Dieses Ergebnis entspricht einer oberen Grenze von 1.6×10^{-6} bei einem Vertrauensniveau von 90% . Hierbei ist die erste oben erwähnte Unsicherheit statistischer und die zweite systematischer Natur. Die Methode die hierbei Verwendung findet ist ein Maximum Likelihood Anpassung mit verschiedenen diskriminierende Variablen um zwischen Signal und Untergrund Komponenten zu unterscheiden.

Contents

1 Preface

The goal of this analysis is the measurement of the branching fraction and polarization of the charmless quasi-two-body B decay $B^+ \to a_1^+ K^{*0}$ using data collected with the BABAR detector at the Stanford Linear Accelerator Center (SLAC)[1] [2]. Since there never have been attempts to measure this decay before, this is the first search for that decay.

The charged B meson decay $B^+ \to a_1^+ K^{*0}$ is a rare hadronic decay of the B meson. It's branching fraction is expected to be of the order of one in one million, which makes it's analysis a challenging task. On the other side, since it is a rare decay, it is sensitive to new physics (NP) that could significantly raise the branching fraction. The small expected branching fraction for the standard model of elementary particle physics (SM) arise from the fact that the decay is only possible due to loop contributions. These loop or penguin contributions are strongly suppressed. The polarization measurement is connected directly to the angular distribution of the B meson decay to two mesons with non-zero spin. This is of special interest since it is sensitive to the quark-spin alignment in the decay transition, and reflects the weak- and strong-interaction dynamics. Moreover new physics could also change the expected polarization in the decay.

From the experimental point of view, this rare decay is not easy to measure and hence the strategy for the analysis is given by the requirements to find a small signal in a sea of background events. In the past it turned out that an analysis based on a maximum likelihood fit technique using a hand full of different discriminating variables is able to distinguish signal events from background components. Therefore, this kind of analysis technique is used. The analysis is performed as a blind analysis, in which the final result, and the data on which it is based, are kept hidden until the analysis is essentially completed. The principal motivation is to avoid experimenter's bias.

All this leads to the outline of the thesis, where it is organized beside this chapter as follows: In chapter 2 the theoretical concepts concerning the decay

[1]The laboratory was recently renamed to SLAC National Accelerator Laboratory (SLAC).
[2]Inclusion of the charge conjugate mode is implied except where explicitly stated otherwise.

$B^+ \to a_1^+ K^{*0}$ are introduced, beginning with a short introduction into the standard model of particle physics, followed by some details of B meson physics leading to the details of the decay $B^+ \to a_1^+ K^{*0}$ and the theoretical approach to calculate a branching fraction. In chapter 3 the experimental foundations of the measurement, namely the relevant aspects of the *BABAR* detector are presented. Beside the hardware detector aspects some software aspects like particle candidate reconstruction and event simulation are discussed. Chapter 4 contains the main part of the thesis and the details about the analysis. There the event selection and B meson candidate reconstruction are presented, then the different backgrounds for the decay are classified. Followed by the introduction of the maximum likelihood fit technique. In order to be able to trust the results the maximum likelihood fit is validated with toy experiments before the fit procedure is used on the data and the results are shown. The results are then cross checked. The systematic uncertainties which arise for the analysis are subsequently discussed. Finally, chapter 5 is devoted to the conclusions for the analysis and an outlook.

2 Theoretical Background

This chapter gives an overview on the theoretical aspects of this work, starting with a short introduction into particles and interactions with a focus on electroweak interactions and B meson physics. In addition the decay $B^+ \to a_1^+ K^{*0}$ is reviewed, followed by a discussion of the theoretical approach to estimate a branching fraction for this decay. Finally it is looked into the properties of the involved a_1 meson.

2.1 Particles and Interactions

The standard model of particle physics reflects today's knowledge of interactions between the fundamental particles. The elementary fermions are leptons and quarks, they can be separated into three generations. The six different types of quarks, known as flavors, u, d, c, s, t and b and the six flavours of leptons are shown in table 2.1. Together with the exchange particles, the gauge bosons,

Table 2.1: *Fundamental fermions: leptons and quarks.*

	generation 1	2	3	charge
quarks	u	c	t	$+2/3$
	d	s	b	$-1/3$
leptons	e	μ	τ	-1
	ν_e	ν_μ	ν_τ	0

shown in table 2.2, matter is build and fundamental processes can be described. The standard model is extremely successful in predicting present-day high energy results. With this fundamental parts non-elementary particles – hadrons – are build up. The binding for these particles is realized by the strong interaction via gluon exchange. For the strong interaction the underlying theory is the quantum chromo dynamic (QCD), a non-Abelian SU(3) gauge field theory [1]. As a

Table 2.2: *Fundamental bosons: the exchange particles for the interaction. Given is also the relative strength with respect to the strong interaction. The graviton is hypothetically.*

interaction	exchange particles	relative strength
strong	gluon, g	1
electromagnetic	photon, γ	10^{-2}
weak	$W^{\pm}$, Z^0	10^{-7}
gravity	(graviton, G)	10^{-39}

result of the theory, the QCD coupling constant α_s decreases logarithmically with higher energies. This also leads to the confinement, that quarks cannot be isolated singularly, and therefore cannot be directly observed. Quarks, by default, clump together to form hadrons. Hadrons which are made up from a quark and an anti-quark are called mesons.

An important concept for the SM are symmetries. Three of the symmetries are usually referred to as charge conjugation C, parity P, and time reversal T. Charge conjugation C means reversing the electric charge and all the internal quantum numbers. Parity P is the reversal of the space coordinates, but not the time. Time reversal T is replacing time t by $-t$, so this reverses time derivatives like momentum and angular momentum. The SM violates each of these symmetries individually at certain points and the SM shows even a slight violation of CP symmetry, which is the combination of C and P symmetry. The slight CP violation result in differences between matter and anti-matter and makes up a fraction of the necessary CP violation for the creation of the universe [2].

2.2 The Electroweak Interaction and Quark Mixing Matrix

In the SM fermion masses are created by the so-called Yukawa-Coupling to the Higgs-field. As a result of this coupling a quark mass-mixing matrix follows which is commonly known as the Cabibbo-Kobayashi-Maskawa (CKM) matrix. The CP violation is incorporated in the SM by including a complex phase in the CKM matrix. The quark mass-mixing means that the CKM matrix relates the vector of the quark mass eigenstates $(d, s, b)^T$ to the vector of their weak interaction eigenstates:

$$\begin{pmatrix} d' \\ s' \\ b' \end{pmatrix} = \begin{pmatrix} V_{ud} & V_{us} & V_{ub} \\ V_{cd} & V_{cs} & V_{cb} \\ V_{td} & V_{ts} & V_{tb} \end{pmatrix} \cdot \begin{pmatrix} d \\ s \\ b \end{pmatrix}.$$

The flavor changing charged quark transitions are carried by the exchange particles of the electroweak interaction, the $W^{\pm}$ boson with a mass m_W. The probability for a transition between and within the generations is given by the matrix elements. By construction the complex 3×3 CKM matrix is unitary ($VV^{\dagger} = 1$) and by using all possible constraints, only four free real parameters remain: three angles and the one phase. These are free parameters of the SM and need to be determined by measurements. The phase is responsible for the CP violating reactions in the SM. The CKM matrix shows a strong hierarchy such that transitions within the same generation are favored and transitions between the first and third generation are strongly suppressed.

2.3 B Meson Physics

B mesons, where one of the quarks is a b or anti-b quark type, offer a wide field of interesting physics studies. The main field of B meson physics is CP violation studies and measuring the four parameters of the CKM matrix. In addition there is an interest in high-precision test of the SM, e.g. understanding higher order QCD effects, and perform searches for new physics. Nowadays searches for new physics are especially interesting since the measured phase in CKM matrix is not large enough to explain the matter-anti-matter-asymmetry in universe.

The B meson production at the BABAR detector, which will be described later in section 3, is achieved in B meson pairs by the reaction

$$e^+e^- \to \Upsilon(4S) \to B\overline{B}$$

at a center-of-mass-energy of $\sqrt{s} = 10.58$ GeV. Only a fraction of the e^+e^- collision actually produces an $\Upsilon(4S)$, all other events produced quark anti-quark or lepton anti-lepton pairs. The cross section for this is given in table 2.3. This table gives an overview of the resonant $b\overline{b}$ compared to all other non-resonant production of fermion pairs at the $\Upsilon(4S)$ resonance energy. With total angular momentum of $J = 0$ and odd parity, the B mesons are pseudoscalar mesons (P) and mainly decay via a $b \to c$ quark transition, thus resulting in D or D^* mesons in the final state [4].

Table 2.3: *Resonant ($b\bar{b}$) and non-resonant (others) e^+e^- production cross-sections at $\sqrt{s} = M(\Upsilon(4S))$ within the experimental acceptance of the BABAR detector [3].*

$e^+e^- \rightarrow$	$b\bar{b}$	$c\bar{c}$	$s\bar{s}$	$u\bar{u}$	$d\bar{d}$	$\tau^+\tau^-$	$\mu^+\mu^-$	e^+e^-
Cross-section [nb]	1.05	1.30	0.35	1.39	0.35	0.94	1.16	~ 40

2.4 The Decay $B^+ \rightarrow a_1^+ K^{*0}$

The charged B meson decay $B^+ \rightarrow a_1^+ K^{*0}$ is a rare hadronic decay of the B meson. Such decays are often referred to as quasi-two-body decays, since both mesons in the final state are intermediate resonance states. It's branching fraction is of the order of one in one million, which makes its analysis a challenging task. On the other side, since it is a rare decay, it is sensitive to new physics that could significantly raise the branching fraction.
The $a_1^+(1260)$ meson in the final state is an axial-vector meson (A), with a set of quantum numbers $J^{PC} = 1^{++}$. Where J is the angular momentum, P is the eigenvalue of the intrinsic parity, and C the eigenvalue of the charge conjugation parity. The a_1 is expected to decay into $\rho\pi$, but not fully verified by measurements [4]. This assumption is used throughout the thesis and a systematic uncertainty is estimated later for the results for the case that the a_1 is not decaying with a branching fraction of 100% into $\rho\pi$. More on the nature of the a_1 will follow at the end of this chapter (see section 2.6). The other particle in the final state, the K^{*0} is an excited strange meson, this implies that one of the quark or anti-quark for the meson content is an s or $\bar{s}$ type quark. The set of related quantum numbers is $J^P = 1^-$, thus this meson behaves as a vector meson (V). The K^* decays almost with a branching fraction of 100% into $K\pi$ [4].

Two typical Feynman diagrams for the decay are shown in figure 2.1 and figure 2.2. Both diagrams include a loop and represent in terms of coupling constants lowest order Feynman diagrams, since there are no low order tree diagrams contributing to this decay. This kind of Feynman diagram is often called penguin diagram. The diagram in figure 2.1 illustrates a gluonic contribution with an anti-top quark running in the loop and the corresponding quark mixing matrix elements V_{tb} and V_{ts}. The diagram in figure 2.2 illustrates an electroweak process with an anti-charm quark propagator inside the virtual loop and the corresponding CKM matrix elements V_{cb} and V_{cs}. Both diagrams are just

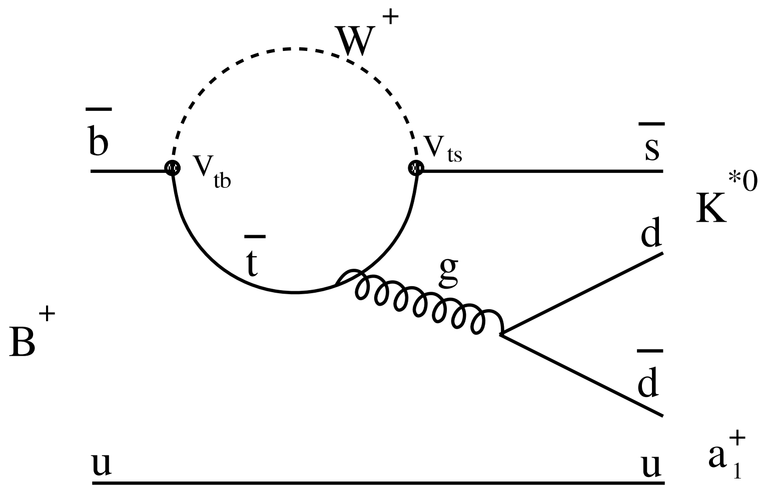

Figure 2.1: *A gluonic $b \to s$ loop Feynman diagram that is contributing in lowest order to $B^+ \to a_1^+ K^{*0}$ decay. In this example diagram a top quark is running in the loop and the corresponding quark mixing matrix elements V_{tb} and V_{ts} are contributing at the weak interaction vertices.*

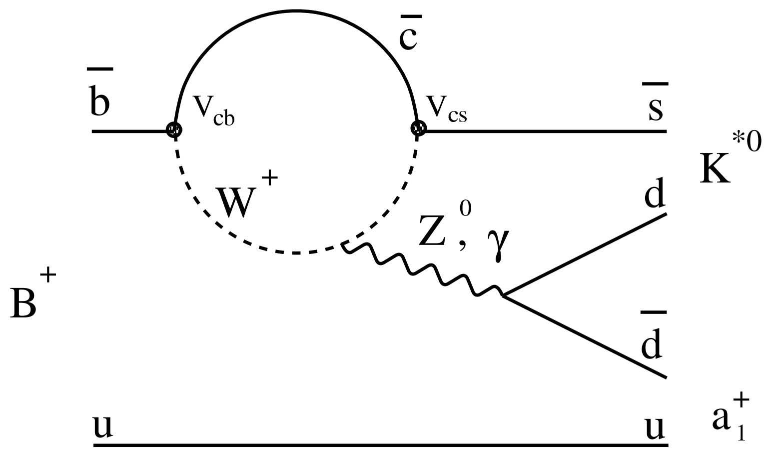

Figure 2.2: *A electroweak $b \to s$ loop Feynman diagram contributing in lowest order to $B^+ \to a_1^+ K^{*0}$ decay, where the W^+ boson emit either a Z^0 boson or a photon. In this example diagram a charm quark is running in the loop and the corresponding quark mixing matrix elements V_{cb} and V_{cs} are contributing at the weak interaction vertices.*

examples and there is also a gluonic contribution with an anti-charm quark propagating inside the loop. Contributions with an anti-charm or anti-top quark are the dominating contributions due to the mass and the corresponding quark mixing matrix elements. In general tree diagrams can not contribute to the $B^+ \to a_1^+ K^{*0}$ decay, since by emitting a W^+ boson from the $\overline{b}$ quark the $\overline{b}$ quark propagator changes to a $\overline{u}$ quark and the W^+ boson decays into a $u\overline{s}$ quark pair. With this a u quark and a $\overline{u}$ quark instead of a d quark and $\overline{d}$ quark in the final-state it is not possible to form a_1^+ and K^{*0} mesons directly. But it is possible with final-state interactions (FSIs), where the $u\overline{u}$ quark pair evolve into a $d\overline{d}$ quark pair. Generally for hadronic B decays the FSIs are expected to play only a minor role, as the energy release in the energetic B decay is so large that the final-state particles are moving fast and hence they do not have adequate time for getting involved in final-state rescattering.

In particular this decay is potentially sensitive to new physic beyond the standard model, due to the $b \to s$ loop transition. The reason is that new heavy non-SM particles can contribute via loop diagrams and for example increase the branching fraction.

A very important aspect for the $B^+ \to a_1^+ K^{*0}$ decay is that it is a pseudoscalar meson to vector meson and axial-vector meson ($P \to VA$) decay. For such a decay the differential decay width dΓ has three complex amplitudes A_λ corresponding to the vector or axial-vector meson helicities $\lambda = 0$ and ± 1 [5]. The latter two are usually rewritten as $A_{\parallel,\perp} = (A_{+1} \pm A_{-1})/\sqrt{2}$. This spin alignment can also be defined with the parameter

$$f_L \quad = \quad \frac{|A_0|^2}{\sum\limits_{\lambda} |A_\lambda|^2},$$

where f_L is called the longitudinal polarization fraction and range from 0 to 1.

The differential decay width can be expressed for this $P \to VA$ transition as

$$\begin{aligned} \frac{9}{8\Gamma}\frac{d^2\Gamma}{d\mathcal{H}_1 d\mathcal{H}_2} &= \mathcal{P}_{VA}^{ang}(\mathcal{H}_1, \mathcal{H}_2) \\ &= f_L \cdot (1-\mathcal{H}_1^2)\mathcal{H}_2^2 + \frac{1}{4}(1-f_L)\cdot(1+\mathcal{H}_1^2)(1-\mathcal{H}_2^2) \qquad (2.1) \end{aligned}$$

where $\mathcal{H}_1$ and $\mathcal{H}_2$ is defined as

$$\mathcal{H}_i = \cos\theta_i$$

with $i = 1$ and 2 in case for the a_1 meson and for the K^* meson, respectively. The derivation for the differential decay width is given in [6] and $\mathcal{P}_{VA}^{ang}$ is referred to as $B \to VA$ angular distribution. The helicity angles θ_1 and θ_2 are depicted in figure 2.3 to illustrate the definition. The helicity angle θ_1 is the angle between

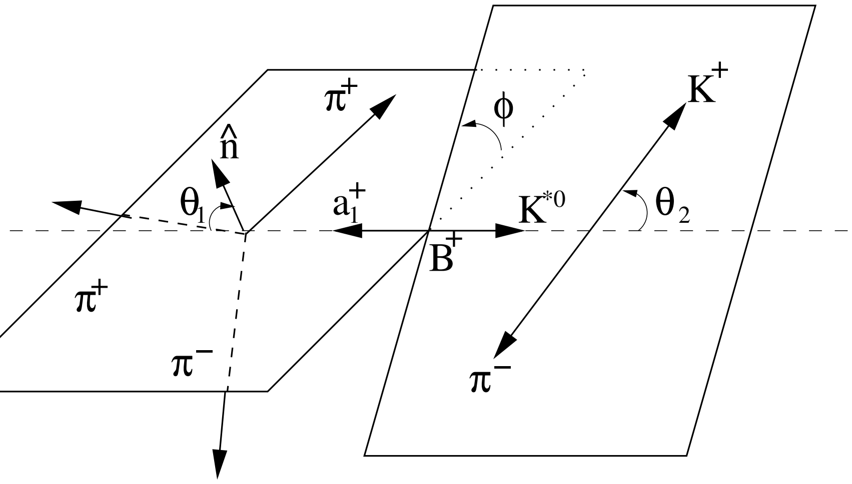

Figure 2.3: *Figure to illustrate the definitions of the helicity angles in the decay $B \to a_1^+ K^{*0}$, where both angles θ_1 and θ_2 are defined in the rest-frame of the decaying meson. Also shown is the angles ϕ, which is the helicity angle between the decay planes of the two systems (see text).*

the decay plane normal of the a_1 meson three body decay ($\hat{\mathrm{n}}$) and the direction opposite the B meson 3-momentum in the a_1 rest frame. The helicity angle θ_2 is defined as the angle between the direction of the K meson 3-momentum and the direction opposite the B meson 3-momentum in the K^* meson rest frame. Figure 2.3 also shows the helicity angle ϕ, which is the angle between the decay planes of the two systems, where the decay plane for the a_1 decay is defined by the B meson decay axis and the normal to the three body decay plane. In principle one is able to obtain the angle ϕ in the decay and extract the additional information[1] associated with the angle ϕ with a 3-dimensional partial helicity distribution, but on the one hand it is expected that to determine ϕ is not an easy task and would result in a large systematic uncertainty on the final branching fraction results [7], and on the other hand it is not essential for a longitudinal polarization fraction and a branching fraction measurement. Generally, only the longitudinal polarization fraction is the common value used to compare results between

[1]Taking into account the helicity angle ϕ generally one is able to measure six real parameters that describe the three complex amplitudes A_0, $A_{\parallel}$ and $A_{\perp}$.

experiment and theory. Thus here the 2-dimensional partial decay distribution, which is given in equation 2.1, where ϕ is already integrated out, is used. The ideal angular distributions in case of longitudinal and transversal polarization for a $P \to VA$ decay are shown in figure 2.4. Here longitudinal polarization denotes a longitudinal polarization fraction of 1 and transversal polarization denotes a longitudinal polarization fraction of 0.

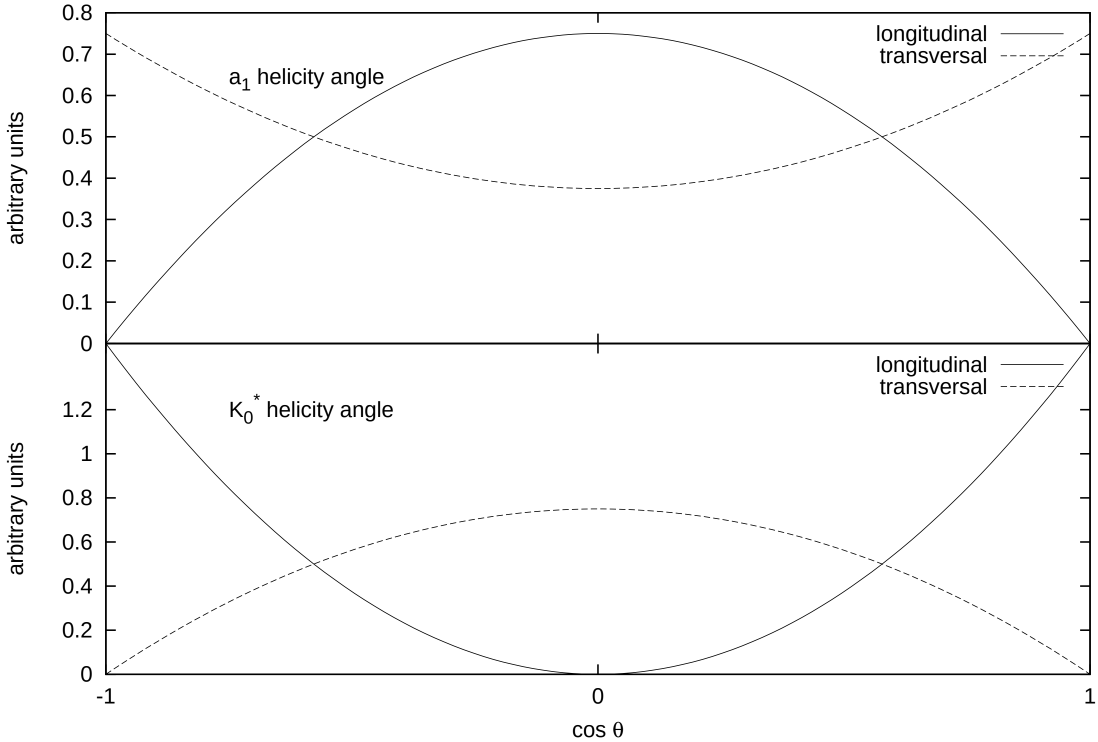

Figure 2.4: *The ideal* $\mathcal{H}_i = \cos\theta_i$ *distribution in case of longitudinal and transversal polarization for the* $P \to VA$ *decay* $B \to a_1^+ K^{*0}$*, with* $i = 1$ *and* 2 *in case for the* a_1 *meson and for the* K^* *meson, respectively. The distributions shown are normalized to integrated area for comparison.*

Very similar to the decay $B^+ \to a_1^+ K^{*0}$ would be a scalar meson to vector meson and tensor meson ($P \to VT$) decay $B \to a_2 K^*$. This decay is a possible background to a $B \to a_1 K^*$ signal decay, because the a_2 meson leads to the same final state. The properties for the a_2 meson are discussed later with the ones for the a_1. The 2-dimensional differential decay distribution for a $P \to VT$ decay becomes [6]:

$$\frac{9}{45\Gamma}\frac{d^2\Gamma}{d\mathcal{H}_1 d\mathcal{H}_2} = \mathcal{P}^{ang}_{VT}(\mathcal{H}_1,\mathcal{H}_2)$$
$$= f_L \cdot \mathcal{H}_1^2(1-\mathcal{H}_1^2)\mathcal{H}_2^2 + \frac{1}{4}(1-f_L)\cdot\frac{1}{3}(4\mathcal{H}_1^2 - 3\mathcal{H}_1^2 + 1)(1-\mathcal{H}_2^2)$$

These ideal angular distributions in case of longitudinal and transversal polarization for a $P \to VT$ decay are visualized in figure 2.5.

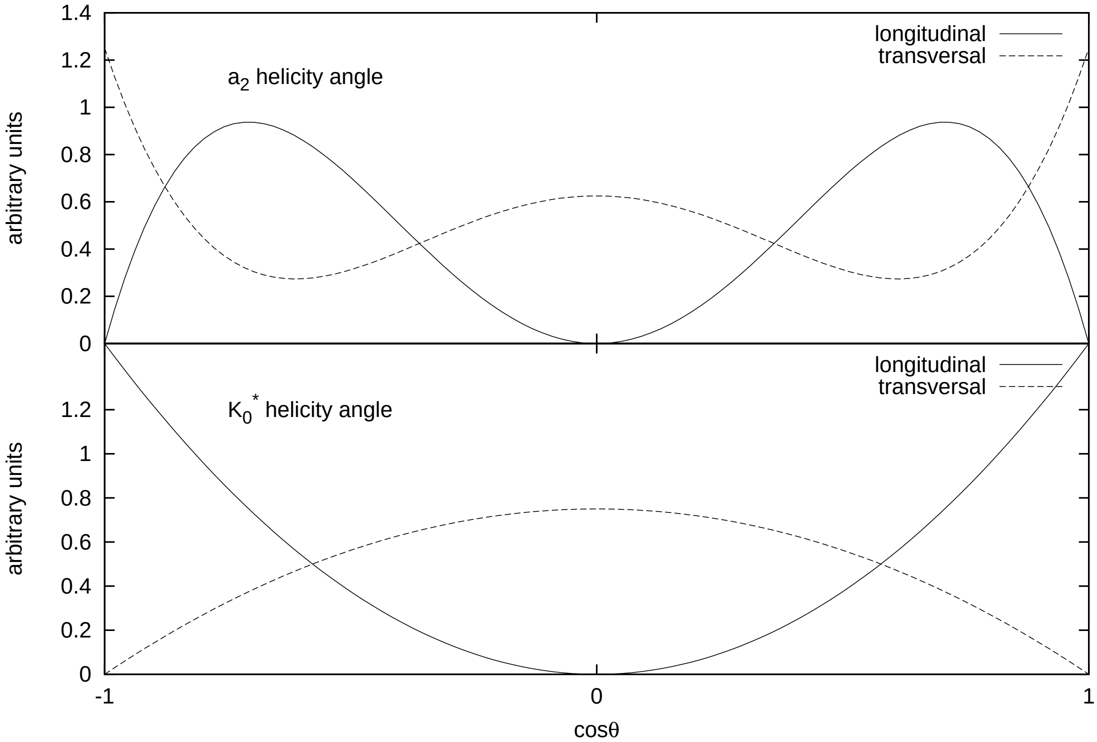

Figure 2.5: *The ideal $\mathcal{H}_i = \cos\theta_i$ distribution in case of longitudinal and transversal polarization for the $P \to VT$ decay $B \to a_2^+ K^{*0}$, with $i = 1$ and 2 in case for the a_2 meson and for the K^* meson, respectively. The distributions shown are normalized to integrated area for comparison.*

There have been no experimental measurements for the $B^+ \to a_1^+ K^{*0}$ decay so far, as well as none for a $B \to a_2 K^*$ decay. An overview of the theoretical expectations for this decay is discussed in the following section.

2.5 The QCD Factorization Approach

This section gives a condensed overview of the theoretical treatment of exclusive charmless quasi-two-body B decays into light mesons and a summary of the recent theoretical results on branching fractions and longitudinal polarization. The theoretical treatment is generally complicated, because of the QCD dynamics related to the pure hadronic final state. The important simplification in order to be able to calculate a branching fraction occurs in the heavy-quark limit $m_b \gg \Lambda_{QCD}$, when the b quark mass is large compared to the strong interaction scale Λ_{QCD}.

A powerful tool to investigate the interaction is the Operator Product Expansion (OPE). The OPE allows to remove the heavy degrees of freedom in low energy processes and simplifies the theory. In fact, one can replace the Hamiltonian of the SM by an effective Hamiltonian. The matrix element for a B meson decaying into two light mesons M_1 and M_2 would be:

$$\mathcal{M}(B \to M_1 M_2) = \langle M_1 M_2 | \mathcal{H}_{\text{eff}} | B \rangle \ .$$

The expression for the effective weak Hamiltonian describing B decays is given by

$$\mathcal{H}_{\text{eff}} = \frac{G_F}{\sqrt{2}} \sum_{p=u,c,t} \lambda_p^{(D)} \left(\sum_i C_i(\mu) \cdot Q_i(\mu) \right) \ ,$$

where $\lambda_p^{(D)} = V_{pb} V_{pD}^*$ and $D = d, s$ can be a d or s quark depending on the decay mode under consideration and $p = u, c, t$. Q_i are local operators, e.g. QCD and electroweak penguin operators, and C_i the corresponding Wilson coefficients. The parameter μ is the scale at which the expansion is applied to. The elegance of this technique comes from the separation of perturbative and non perturbative effects. All the short distance contributions are concentrated in the Wilson coefficients $C_i(\mu)$, which can be calculated using perturbative QCD. On the other side, all the long distance effects are expressed in the matrix elements of the effective operators $Q_i(\mu)$, once the effective Hamiltonian is contracted on the initial and final states one is interested in. The scale μ represents the separation between long distance and short distance effects and is not related to any feature of the SM Hamiltonian. This means that the dependence of C_i and Q_i on it is unphysical and has to cancel out in the final expression of physical quantities.

The QCD factorization formalism now allows to compute systematically the matrix elements of the weak Hamiltonian in the heavy-quark limit for certain two-body final states. In condensed notation, the matrix element of every operator in the effective Hamiltonian is evaluated as [8]:

$$\langle M_1 M_2 | Q_i | B \rangle = \sum_{M_1', M_2'} F_j^{B \to M_1'} T_{ij}^I * f_{M_2'} \Phi_{M_2'} + T_i^{II} * f_B \Phi_B * f_{M_1} \Phi_{M_1} * f_{M_2} \Phi_{M_2} \; .$$

Where $F_j^{B \to M_1'}$ is an appropriate $B \to M_1'$ form factor, Φ_M are leading-twist light-cone distribution amplitudes. Light-cone meson distribution amplitudes are defined in terms of matrix elements of non-local light-ray operators stretched along a certain light-like direction and sandwiched between the vacuum and the meson state [9] that describe the momentum-fraction distribution of the quarks in the meson. The star products ($*$) imply an integration over the light-cone momentum fraction of the constituent quarks inside the mesons. f_M is the decay constant for a meson M. A justification of the factorization formula for final states with two light mesons, like the a_1 and K^* meson, has been proved at order α_s [10], but a complete proof has not yet been given.

The factorization approach reduces the complicated hadronic matrix elements of four-operators to simpler non-perturbative quantities and calculable hard-scattering kernels T_{ij}^I and T_i^{II}. The attempt of a graphical representation of the QCD factorization formalism is shown in figure 2.6. The kernels T_{ij}^I take

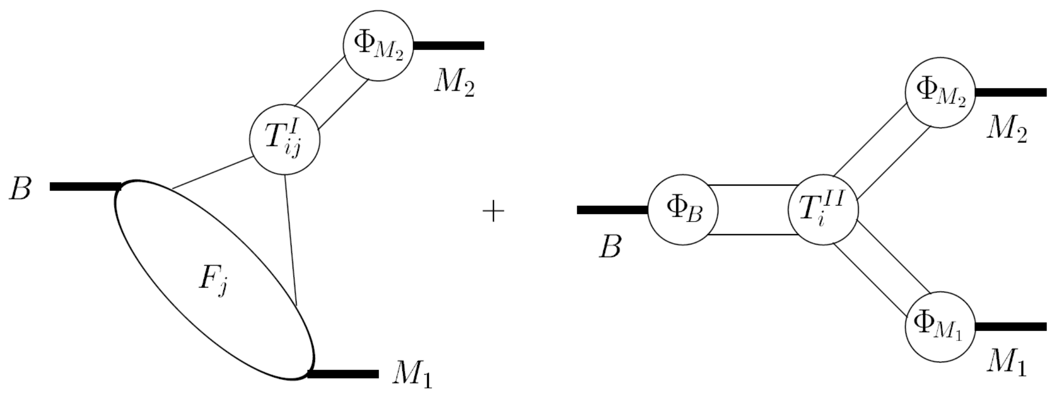

Figure 2.6: *Graphical representation of the factorization formula for a B meson decay into two mesons M_1 and M_2. Only one of the two form-factor terms F_j is shown for simplicity. Φ_M are the light-cone distribution amplitudes and T_{ij}^I and T_i^{II} the hard-scattering kernels [11].*

care topologically of all four fermion interactions and the calculations are well understood [8]. Contribution here are e.g. from tree graphs, penguin and vertex corrections. The kernels T_i^{II} in the second part of the factorization formula takes care of all six fermion interaction. So these kernels account for the interaction with the light spectator quark and implies non-factorizable soft interactions. Contribution here are e.g. weak annihilations, where one sub-contribution is so-called penguin annihilation contribution. Difficulties for the calculation of these contributions arise from logarithmically diverging integrals and lead also to large uncertainties for these contributions.

All the theoretical details as the calculation of the Wilson coefficients and the hard-scattering kernels as well as an explanation of the light-cone formalism are not touched here, these topics are well explained in theoretical papers [8, 10, 11].

More important for this experimental work are the recent results within this theoretical framework of QCD factorization for $B \to VA$. The available theoretical estimates of the branching fraction of B^+ mesons decaying to $a_1^+ K^{*0}$ come from calculations based on QCD factorization and are done by different groups. The branching fraction estimation for $B^+ \to a_1^+ K^{*0}$ from Calderon et al. is 0.51×10^{-6}. They do not give an uncertainty on their value and do not quote a longitudinal polarization fraction [12]. Cheng et al. predicts beside the branching fraction a longitudinal polarization for the decay $B^+ \to a_1^+ K^{*0}$. Also the predicted branching fractions on the charmless two-body decays $B \to a_1 \pi$ and $B \to a_1 K$ from this group are in quite good agreement with the measurements from *BABAR* [13, 14, 15]. The expected branching fraction for $B^+ \to a_1^+ K^{*0}$ from Cheng et al. is $(9.7^{+4.9+32.9}_{-3.5-2.4}) \times 10^{-6}$ with a prediction for the longitudinal polarization fraction $f_L = 0.38^{+0.51}_{-0.40}$. For the branching fraction the first uncertainty corresponds to the uncertainties due to the variation of Gegenbauer moments, decay constants, quark masses, form factors and a B meson wave function parameter and the second uncertainty corresponds to the uncertainties due to the variation of penguin-annihilation parameters [16]. For the longitudinal polarization fraction, all kinds of uncertainties are added in quadrature, since the theoretical uncertainty is dominated by far by uncertainties in the size of the penguin-annihilation amplitude contribution. The most recent predictions for $\mathcal{B}(B^+ \to a_1^+ K^{*0})$ and the longitudinal polarization fraction are from Yang et al., where the focus is especially on the penguin-annihilation amplitude contribution. The expected branching fraction is $(11.2^{+6.1+31.9}_{-4.4-9.0}) \times 10^{-6}$ with penguin annihilation turned on and $(4.1^{+2.0+1.7}_{-1.6-0.1}) \times 10^{-6}$ without penguin annihilation amplitudes. The corresponding longitudinal polarization fraction is $f_L = 0.37^{+0.48}_{-0.37}$ and $f_L = 0.62^{+0.13}_{-0.34}$, respectively [17].

2.6 Properties of the a_1 and a_2 Mesons

The properties, the invariant mass and width, of the $a_1(1260)$ meson are not accurately known. Relatively large differences for the a_1 parameters are observed for measurements related to hadronic interactions compared to results extracted through τ-decays. The differences are mainly seen in the width, which varies from 250 MeV to 600 MeV. The central a_1 mass value from τ-decays is in relatively good agreement compared to the results from hadronic decays. More details on the different properties are summarized elsewhere [4, 18]. For this analysis, the following parameters are used for the simulation: The a_1 meson mass is $m_{a_1} = 1230\ \mathrm{MeV}/c^2$ and the width is $\Gamma = 400$ MeV, chosen to be consistent with the BABAR measurement in the charmless decay $B \rightarrow a_1^+\pi^-$ [19]. This invariant mass value is in good agreement with $M_{a_1} = (1250 \pm 80)\,\mathrm{MeV}/c^2$ determined using lattice QCD calculations [20]. The a_1 meson is assumed to decay mainly to a ρ and a π meson. It was also seen that the a_1 meson decays through $f^0(600)\pi$[2] as well [4]. The possible decay through $f^0(600)\pi$ is not taken directly into account for the analysis procedure, but as a systematic uncertainty contribution (see section 4.8), since the $f^0(600)$ is not provided within BABAR simulation software.

In general the appropriate description for a broad resonance is a relativistic Breit-Wigner function

$$RBW = \frac{1}{m^2 - m_0^2 + im_0\Gamma(m)} ,$$

where $\Gamma(m)$ is a mass dependent width of the form

$$\Gamma(m) = \Gamma_0 \frac{m_0}{m} \left(\frac{p^*}{p_0^*}\right)^{2J+1} \frac{{}^J F^2(p^*)}{{}^J F^2(p_0^*)} .$$

In both equations m is the invariant mass of the final state particles forming the spin-J resonance. The functions ${}^J F$ are the Blatt-Weisskopf barrier factors [21]: ${}^0F = 1$ for spin 0, ${}^1F = 1/\sqrt{1 + (rp^*)^2}$ for spin 1 and ${}^2F = 1/\sqrt{9 + 3(rp^*)^2 + (rp^*)^4}$ for spin 2 particles. The parameter r is the radius of the resonance[3] and $p^* = p^*(m)$ the momentum of the decay particles at mass m, measured in the resonance rest frame, and $p_0^* = p^*(m_0)$, where m_0 it the resonance mass.

[2] $f^0(600)$ meson is also known as σ meson

[3] r is set to 3.1 GeV^{-1} for parameterization and fitting routines, this is similar to the number used in `EvtGen` simulation (see section 3.9).

The broad width of the a_1 meson implies that other meson states with decays to 3π can lie within its invariant mass distribution. In fact the $a_2(1320)$ meson with an invariant mass of $m_{a_2} = (1318.3 \pm 0.6)$ MeV and a width of $\Gamma = (107 \pm 5)$ MeV [4] does. Compared to the a_1 meson the a_2 meson has a small width. The $a_2(1320)$ meson is characterized by the quantum numbers $J^{PC} = 2^{++}$. With roughly 70% probability the a_2 meson decays into a ρ meson and a π meson, like the a_1 meson. This all confirms that the decay $B^+ \rightarrow a_2 K^{*0}$ is a possible background to the signal decay $B^+ \rightarrow a_1^+ K^{*0}$ that should be considered during the analysis.

3 The BaBar Experiment

The *BaBar* experiment at SLAC is a modern, multi-purpose particle detector. The experiment is situated at the interaction region of the PEP-II storage rings. The PEP-II storage rings provide electrons and positrons with an energy of 9.0 GeV and 3.1 GeV, respectively. The resulting center-of-mass energy with these beam energies is 10.58 GeV and lies within the $\Upsilon(4S)$ resonance. The *BaBar* detector and the PEP-II storage rings have been operated from October 1999 to April 2008. This time was divided into seven run periods for data taking: Run1 to Run6 where PEP-II storage rings operated with a center-of-mass energy within the $\Upsilon(4S)$ resonance and Run7 where the energies of the beams has been changed to result in a center-of-mass energy within the $\Upsilon(2S)$ or $\Upsilon(3S)$. In addition Run7 was also used to perform center-of-mass energy scans. The PEP-II storage rings are designed to provide a peak luminosity of $3 \times 10^{33}\mathrm{cm}^{-2}\mathrm{s}^{-1}$. In October 2005 a record peak luminosity just over $1 \times 10^{34}\mathrm{cm}^{-2}\mathrm{s}^{-1}$ was delivered to the *BaBar* experiment. The integrated luminosity $\mathcal{L}$ for *BaBar* and PEP-II for all data taking periods is show in figure 3.1. Following is a short description of the *BaBar* detector and its major subsystems. A more detailed description of various components can be found in [23]. An overview of the *BaBar* detector is shown in figure 3.2. The e^+e^- interaction products transverse the detector subsystems layer by layer. The Silicon Vertex Tracker (SVT) is closest to the beam pipe, next is the Drift Chamber (DCH), then the Cherenkov Detector (DIRC), and the Electromagnetic Calorimeter (EMC). The instrumented Flux Return (IFR) is the outermost subdetector component and outside the magnet. The super-conducting coil provides a solenoidal magnetic field of 1.5 T. The detector has only been slightly modified over the time, where the major modification was the replacements of active detector hardware within the IFR. The BaBar coordinate system is defined as a right handed system such that:

- The $+z$ axis is parallel to the magnetic field of the solenoid and in the direction of the high energy electron beam.
- The $+y$ axis points vertically upward.
- The $+x$ axis points horizontally, away from the center of the PEP-II ring.
- The origin, $(0, 0, 0)$, is defined as the nominal interaction point of the

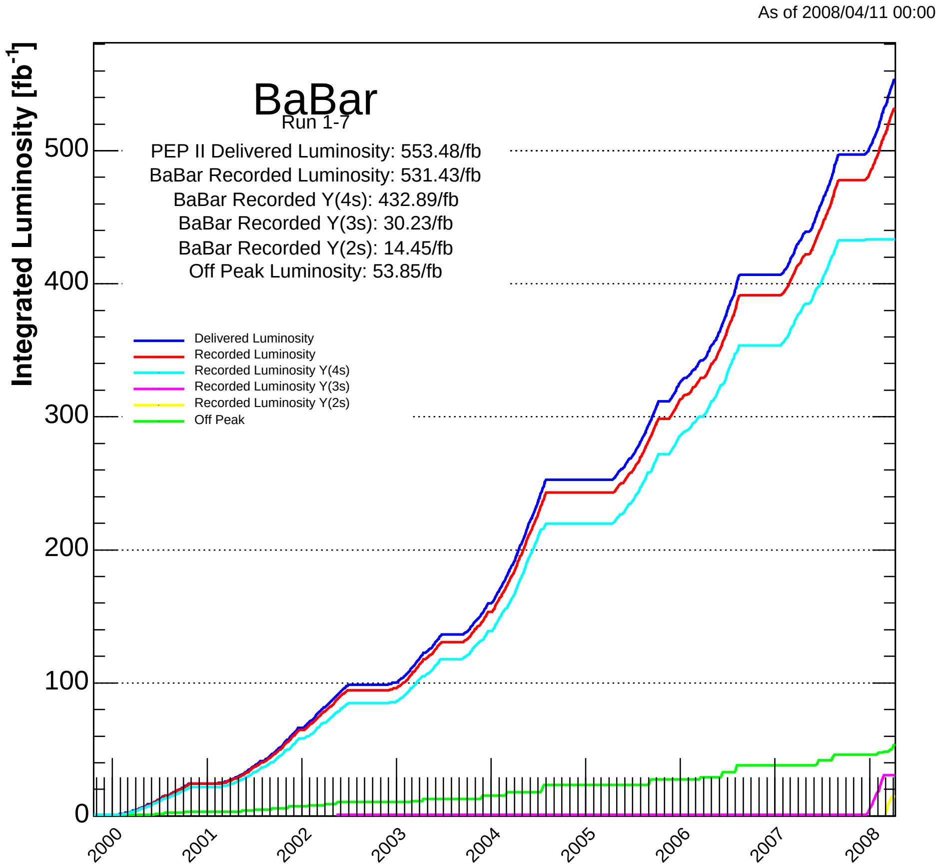

Figure 3.1: *BABAR and PEP-II integrated luminosity $\mathcal{L}$ in units of* fb^{-1}*for all data taking periods. Beside data taking at a center-of-mass energy of the $\Upsilon(4S)$ (On-Peak) also run periods at the $\Upsilon(3S)$, $\Upsilon(2S)$ and just below the $\Upsilon(4S)$ resonance center-of-mass energy (Off-Peak) data is shown [22].*

positron and electron beam and due to the asymmetric beam energies not in the geometrical center of the detector.

3.1 Silicon Vertex Tracker (SVT)

The Silicon Vertex Tracker (SVT) is one of the two *BABAR* tracking devices and is designed to reconstruct decay vertices. It is made out of 5 cylindrical layers of double-sided silicon micro strip detectors. Each layer is divided azimuthally into modules, these are arranged in a way that neighbored modules overlap each other, ensuring a full azimuthal coverage. The silicon strips of the inner side of

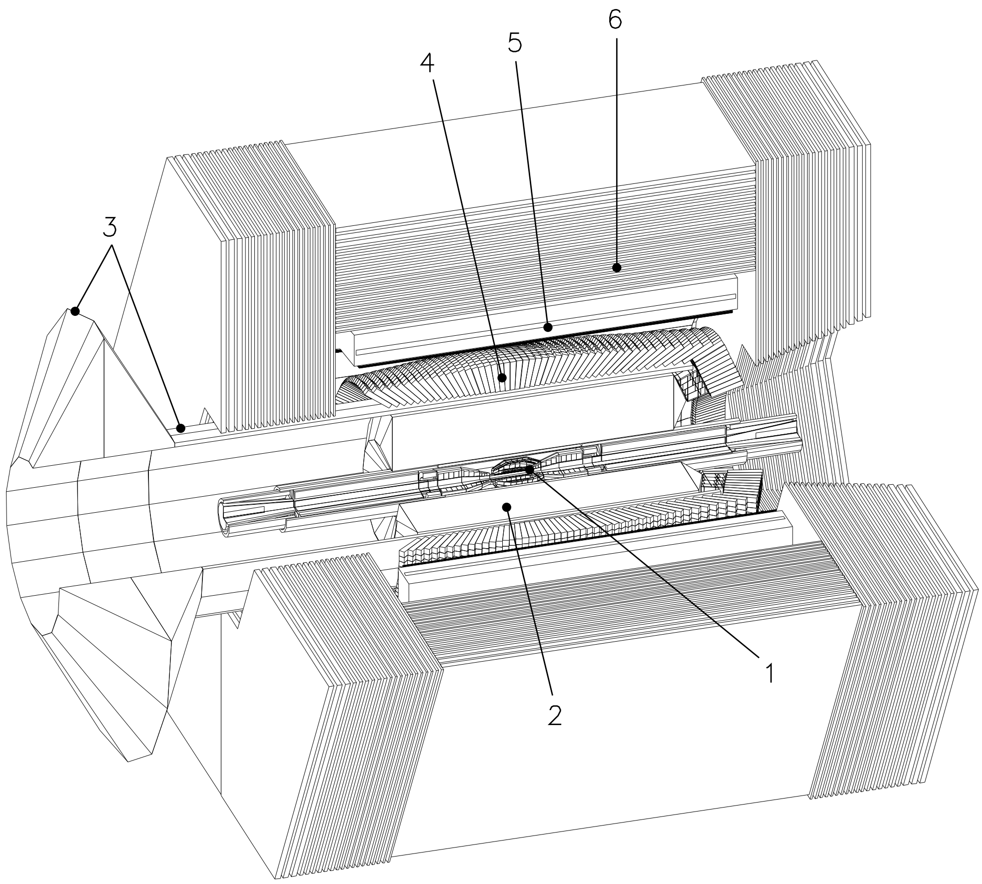

Figure 3.2: *Layout of the BABAR detector: (1) Silicon Vertex Tracker (SVT); (2) Drift Chamber (DCH); (3) Cherenkov Detector (DIRC); (4) Electromagnetic Calorimeter (EMC) (5) Magnet Coil; (6) Instrumented Flux Return (IFR). The high energy electrons enter from the left side and the low energy electrons from the right side of the figure [3].*

each module are perpendicular to the beam axis to measure the z coordinate. The strips on the outer side are arranged parallel to the z axis to measure the azimuthal angle. The SVT vertex resolution, depending on the B meson decay, is $60 - 100\ \mu$m and the polar angle coverage is about 90%.

3.2 Drift Chamber (DCH)

The other tracking device of *BABAR* is the Drift Chamber (DCH), a 280 cm long cylinder with a radius of 80.0 cm. The chamber contains 7104 hexagonal drift cells, that are arranged in 40 cylindrical layers, with four of these layers are grouped into a superlayer. Each drift cell is a sense wire surrounded by six field wires, making up the hexagonal structure. In order to reconstruct a 3 dimensional trajectory of a particle, the wires within a superlayer show different stereo angles: apart from axial (A), there are superlayers with positive (U) and negative (V) stereo angles, with their absolute values increasing with the radius of each layer. The arrangement of the 10 superlayers follows the pattern AUVAUVAUVA.

3.3 Cerenkov Detector (DIRC)

The Detector of Internally Reflected Cerenkov light (DIRC) is a ring imaging Cerenkov detector based on total internal reflection of Cerenkov light and is used for particle identification in combination with the momentum measurement; the Cerenkov light is produced by charged particles moving faster than the speed of light c within a radiator of refractive index n. The light is then emitted under the Cerenkov angle Θ_C:

$$\cos\Theta_C = \frac{1}{n\beta}$$

where $\beta = \frac{v}{c}$ and v is the speed of the particle. The radiator, that consist of 144 straight fused silica bars ($n = 1.473$) with rectangular cross section, is located between the Drift Chamber and the Electromagnetic Calorimeter. It is subdivided into 12 azimuthal regions, each being formed by a bar box containing 12 bars. Each bar has a rectangular profile of $1.7\,\mathrm{cm} \times 3.5\,\mathrm{cm}$ and a length of $4.9\,\mathrm{m}$. The modules cover 94% of the full azimuth and 83% of the full polar angle. The light emitted by the charged particles travels through the radiator, due to total reflection and a mirror at the front end of each bar. The light reaches the rear end after multiple reflections. The photons exit into an expansion region, called the standoff box, filled with 6000 liters of purified water and are detected by a close packed array of 10572 photomultiplier tubes, mounted on the toroidal surface on the back. Except for a number of discrete ambiguities, the magnitude of the Cerenkov angle is preserved during this process. To resolve these ambiguities, measurements of the photon arrival times and pattern recognition algorithms are used.

3.4 Electromagnetic Calorimeter (EMC)

The Electromagnetic Calorimeter (EMC) is the main device for electron-pion separation and neutral pion and photon reconstruction. It consists of 5760 Thallium-doped Caesium iodide CsI(Tl) crystals in the barrel and 820 crystals in the endcap. CsI(Tl) features a Moliere radius of $R_m = 3.8\,\mathrm{cm}$ and a radiation length of

$X_0 = 1.85\,\text{cm}$. The EMC barrel, located within the magnet cryostat, is made of 48 polar angle rows, each having 120 crystals in azimuthal angle. The end-cap is divided into 8 rings with a segmentation in azimuth angle varying between 80 and 120 crystals. Every crystal is a truncated trapezoidal pyramid with a length between $16.1X_0$ and $17.6X_0$ with a front face of typically $5\,\text{cm} \times 5\,\text{cm}$. Read out is realized with two independent $2\,\text{cm}^2$ large area pin[1] photodiodes epoxied to the rear face.

3.5 Instrumented Flux Return (IFR)

The Instrumented Flux Return (IFR) is designed to identify muons and to detect neutral hadrons. It consists of a barrel and two end-caps made of iron. The iron is segmented into 18 plates, with Resistive Plate Chambers (RPC) or Limited Streamer Tubes (LST) mounted in the 17 gaps. The Barrel has 4 more active layers: a double layer surrounding the EMC, a layer between the solenoidal coil and iron and a last layer outside the iron. A plate has a length between 194 cm and 320 cm and a width of 125 cm. An RPC layer consist of two 2 mm-thick bakelite[2] sheets separated by a gap of 2 mm. These two surfaces are connected to high voltage and ground. The signals are read out capacitively, on both sides of the gap, by external electrodes made of aluminum strips. An LST cell consists of a silver plated sense wire $100\,\mu$m in diameter, located at the center of a cell of 9 mm square section. A plastic extruded structure, called profile, contains 8 such cells. The profile is coated with a resistive layer of graphite. The RPCs have been replaced in 2004 and 2006 with LST interleaved with brass. The brass is utilized to add mass for the interaction length since the LST modules are less massive than the RPCs. The replacement was necessary due to improper assembling of the RPCs, leading to large inefficiency for muon reconstruction.

3.6 Trigger

The *BABAR* trigger is designed to select a large variety of physics processes (efficiency greater than 99% for $B\overline{B}$ events) while keeping the output rate below 400 Hz to satisfy computing limitations of the offline processing farms. The trigger accepts also 95 % of continuum hadronic events and more than 90 % of $\tau^+\tau^-$ events. It is implemented as a two level hierarchy, the hardware Level 1 (L1) followed by the software Level 3 (L3). The L1 trigger has an output rate of the order of 1 kHz to 3 kHz, depending on the luminosity and background conditions. It is

[1]positive intrinsic negative
[2]phenolic polymer

based on charged tracks in the DCH, showers in the EMC, and tracks detected in the IFR. The L3 trigger operates by refining and augmenting the selection methods used in L1. The L3 software algorithm selects events of interest and then allowing them to be transferred to mass storage data for further analysis.

3.7 Particle Reconstruction and Identification

The detector components described above provide raw information about all recorded events. From this particles candidates are reconstructed. Such objects contain all kinds of physical information for data analysis like mass, energy and momentum. These particle candidates are sorted into corresponding lists depending on certain criteria. All available candidate lists are summarized in [24], where the different requirements are listed. The basic list is a charged track candidate lists build up by fitting a trajectory with track hits from SVT and DCH.

In order to divide charged tracks candidates into pion, kaon, electron or myon candidates additional particle identification (PID) information from sub-detectors are used to fill the corresponding lists [25]. Mainly the energy loss dE/dx along the track compared to calculations from Bethe-Bloch formula [4] and the Cerenkov angle and detected number of photons from DIRC are used. For electron candidates in addition the energy deposition in the EMC is important, for myon candidates the IFR information is mainly utilized [26].

3.8 Data Sub-Sets

The large amount of data, shown in figure 3.1, forces the *BABAR* community to distribute the data to different computing sites[3] in order to provide enough computing capacity for the data processing. Therefore the data is divided into sub-sets of events selected with a specific physic signature or decay topologies for use in *BABAR* analyses [27]. In the terminology of the *BABAR* community these sub-sets of events are called skims. Related analyses take advantage of using the same skim, since the pre-selection of events is done only once. Running an analysis on a skimmed dataset is in general faster and the total amount of computing resources needed is reduced.

[3]Beside SLAC computing site, the *BABAR* experiment is using officially the computing sites: IN2P3, RAL and GridKa.

3.9 Event Simulation

For developing analysis techniques and selection criteria as well as understanding the detector behavior and calculating selection efficiencies a detailed event simulation is required.
The *BABAR* Monte-Carlo-Simulation (MC) is done in three steps: first, the basic physical process with best theoretical knowledge available is simulated, where e.g. `EvtGen` [28] is used for exclusive B decays. Second, the particle is traced through the detector and the interactions with the detector is simulated [29]. Third, the detector response for the read-out electronic is simulated. Finally noise and beam background, picked up during data taking, is overlaid with the simulation. After these steps the simulated events are available in the same event format as the data and the same reconstruction procedure as for the data is applied.

For practical reasons there are two different kinds of MC events: One are the so-called generic $B\overline{B}$ MC events, where both B mesons from the $\Upsilon(4S)$ decay decay generically, depending on the world average or with best available knowledge estimates B meson branching fractions. The underlying B meson branching fractions reflect the current best knowledge from theory and experiments. The others are the so-called signal MC decays, that means one B meson from the $\Upsilon(4S)$ decay decays generically as described above and the other one decays in a pre-defined way for every single event.

All these decay scenarios are steered by a decay file, that defines how a decay is simulated by `EvtGen`. For a simple management of the different decays every decay scenario is assigned a mode number. E.g generic B^+B^- in *BABAR* is assigned the mode number 1235 and generic $B^0\overline{B}^0$ the mode number 1237.

A feature of the simulation is to compare the properties of the generated particles and the reconstructed particle candidates. With these information one can judge if a reconstructed particle candidate represents one of the generated particles. To get these information a so-called truth-match algorithm is used.

4 Analysis

The analysis of the decay $B^+ \to a_1^+ \ K^{*0}$ is based on a maximum likelihood fit to extract the branching fraction and polarization. The fit uses seven variables to distinguish between five components where one is the signal component and the other four components describe different backgrounds. Around this core method the steps involved in the analysis are presented in this chapter. The involved steps are split into different sections: the chapter starts with the definition of the used data samples and the pre-selection to obtain data sub-sets for the analysis (see section 3.8). This is followed by the explanation of the reconstruction of the decay, where the reconstruction involves a kinematic fitting procedure, and the final event selection. The last step for the selection includes choosing between more than one possible reconstructed B candidate. The following step is the discussion of the different possible background contributions for the analysis. Four background contributions are grouped: the biggest fraction of background is arising from continuum background others are charm background, charmless background and a $B \to a_2 K^*$ decay background component. The description of the charm, charmless and $B \to a_2 K^*$ decay background component are taken from MC samples, while the continuum background is taken from data. Therefore, sidebands in two the variables m_{ES} and ΔE – both defined later in this chapter – are defined and selected together with the data sample. Subsequent to this the probably most important step is the analysis technique including the maximum likelihood fit procedure. The fit procedure is then validated with MC toy experiments and the results of the fit are shown. The final steps are then cross checks the results and determine all possible systematics uncertainties.

4.1 Data Samples

The analysis is based on the Run1 to Run6 *BABAR* dataset collected in the years 1999 to 2007. The dataset consists of an integrated luminosity of $423.5\,\mathrm{fb}^{-1}$ collected at the $\Upsilon(4S)$ resonance corresponding to a production of (465.0 ± 5.1) million $B\overline{B}$ pairs.

For data (On-Peak) and generic MC the `BToA1Kst` sub-set (skim) [30, 31] is used. A large fraction of skims (including the skim `BToA1Kst`) are set-up and centralized produced in advanced for upcoming interesting analysis topics. These skims use loose criteria for selection. The `BToA1Kst` skim is using a kinematic fit algorithm [32] to build B meson candidates from $a_1$and K^* meson candidates and applies the following pre-selection criteria:

$$\begin{aligned} 0.6 \leq & \quad m_{a_1} & \leq 1.8 \text{ GeV}/c^2 \\ 0.45 \leq & \quad m_{K^{*0}} & \leq 1.1 \text{ GeV}/c^2 \\ 5.225 \leq & \quad m_{\text{ES}} & \leq 5.3 \text{ GeV}/c^2 \\ -0.2 \leq & \quad \Delta E & \leq 0.2 \text{ GeV} . \end{aligned}$$

The variables m_{a_1}, $m_{K^{*0}}$, m_{ES} and ΔE are used for the final event selection; therefore they are defined and discussed subsequent in section 4.2. Also the B, a_1 and K^* meson candidates composition is in detail explained there.

Most of the MC studies are done with MC data produced within the official *BABAR* MC production cycle. In case of the signal decay two MC samples are produced: longitudinal polarized signal MC, where the longitudinal polarization fraction is set to be 1 and transversal polarized signal MC, where the longitudinal polarization fraction is set to be 0. For later steps in the analysis, like validation studies for the maximum likelihood fit, any value of the longitudinal polarization fraction for a signal decays is mixed by using proper portions from these two base MC samples. The numbers of produced events for the signal decay and the generic $B\overline{B}$ MC are given in table 4.1. The signal and background MC samples,

Table 4.1: *Number of events for longitudinal and transversal polarized signal and generic $B\overline{B}$ MC datasets used in this analysis. For the generic MC samples the numbers are obtained using the* `BToA1Kst` *skim and in brackets the full numbers before skimming are shown.*

	longitudinal signal	transversal signal	generic B^+B^-	generic $B^0\overline{B}^0$
run6	20k	20k	558k (101M)	478k (102M)
run5	67k	67k	1300k (244M)	1057k (234M)
run4	50k	50k	913k (168M)	749k (162M)
run3	17k	17k	273k (50M)	220k (47M)
run2	31k	31k	556k (103M)	469k (102M)
run1	10k	10k	196k (37M)	169k (37M)
Total	195k	195k	3796k (703M)	3142k (684M)

which in detail are shown and discussed in section 4.3, were generated with detector conditions covering the full data period. The charmless background component that is composed out of different charmless MC decays which are in details given in section 4.3. The continuum sample is taken from m_{ES} and ΔE sideband data.

In addition, a possible $B \to a_2 K^*$ component is explored with a privately produced MC sample; Nevertheless to do so the official release and configuration has been used along with a background trigger mix covering the full data period. The `EvtGen` models used for the $B \to a_2 K^*$ signal MC decay is given in appendix B. The helicity angle distributions obtained from the $B \to a_2 K^*$ production (shown later in section 4.4.1 in figure 4.3) have been compared to the theoretical calculated distributions [6] and are in agreement. The $B \to a_2 K^*$ sample consists of 19k events for longitudinal and 19k events for transverse polarization.

A comparison of the numbers of B mesons from generic $B\overline{B}$ MC in table 4.1 to the Run1 to Run6 dataset results in the fact that the generic Monte Carlo events exceed the real data events by a factor of 2.985. This is a reasonable size for the generic $B\overline{B}$ MC sample.

All results and studies are obtained from a processing of data based on official *BABAR* software[1]. In addition to the standard packages from base software release a couple of extra packages in a different version has been used for reconstruction. These packages with version tag are given in section A in table A.1.

4.2 Event Selection and Candidate Reconstruction

This section explains how the events of interest are selected and in which way the B meson candidates for future use are reconstructed. In particular the section starts with the details of the B meson candidate composition, this includes some loose pre-selection cuts. Then the main selection criteria are presented, followed by the studies for the best B meson candidate selection, since an event can offer more than one candidate which could be a signal B meson. Finally the total selection efficiency is calculated.

4.2.1 B Meson Composition

The B meson production at the *BABAR* experiment is achieved in B meson pairs by the reaction $e^+e^- \to \Upsilon(4S) \to B\overline{B}$ at a center-of-mass-energy of

[1] *BABAR* analysis release: Analysis-42.

$\sqrt{s} = 10.58$ GeV. In the $\Upsilon(4S)$ rest frame, the B mesons have low momenta, so that the decay of each B meson is nearly isotropic. A B meson candidate is characterized kinematically by the energy substituted mass,

$$m_{\mathrm{ES}} = \sqrt{(s/2 + \mathbf{p}_0 \cdot \mathbf{p}_B)^2/E_0^2 - \mathbf{p}_B^2}$$

and the energy difference

$$\Delta E = E_B^* - \sqrt{s}/2$$

where $(E_B, \mathbf{p}_B)$ is the four-momentum of the B meson candidate, $(E_0, \mathbf{p}_0)$ is the four-momentum of the initial state, and E_B^* is the energy of the B meson candidate in the center-of-mass frame. The ΔE distribution for signal events peaks at zero with a typical width of 20 MeV, while the m_{ES} distribution peaks at the B meson mass with a width of about $3\,\mathrm{MeV}/c^2$. These two variables are very helpful to distinguish between signal decays and background, as well as they are used to define the continuum background by selecting events from data in m_{ES} or ΔE sidebands.

The B meson candidates are formed by combining an a_1^+ meson candidate with a K^{*0} meson candidate. The a_1^+ meson candidate is reconstructed in the dominant decay mode $\rho^0\pi^+$ with $\rho^0 \to \pi^+\pi^-$. The K^{*0} meson is reconstructed in the decay mode $K^+\pi^-$. All these candidate compositions are done within the BABAR software framework for particle candidate composition [33]. The pion candidates are taken from a charged track list with minimum transverse momentum of 0.1 GeV, minimum number of 12 hits in drift chamber (DCH), a maximum momentum of 10 GeV, a maximum for the distance of closest approach (DOCA) in xy-plane of 1.5 cm, a maximum for the DOCA in z of 10 cm and acceptance requirements on the polar angle $(0.410 < \theta < 2.54)$ [24]. For K candidates a track list with additional PID information is used, where the idea is to calculate a likelihood for each particle hypothesis (e.g. pion, kaons or electrons) [34]:

$$\mathcal{L}_i = \mathcal{L}_i^{\mathrm{DIRC}} \times \mathcal{L}_i^{\mathrm{DCH}} \times \mathcal{L}_i^{\mathrm{SVT}}$$

The DCH and SVT likelihoods are calculated by comparing in both cases the measured $\mathrm{d}E/\mathrm{d}x$ against the expected $\mathrm{d}E/\mathrm{d}x$ from the Bethe-Bloch parameterization. In the case of the DIRC the likelihood is constructed from the Cherenkov angle, number of photons, and track quality. For the reconstruction only K candidates are used were $\mathcal{L}_K/(\mathcal{L}_K + \mathcal{L}_\pi) > 0.8176$. From these candidate lists the decay tree is composed with a least squares fit of the decay chain involving multiple decay vertices. The routine deals with the entire decay tree at once; the algorithm does a global decay chain fit and does not a leaf-by-leaf fitting. The decay chain fit uses a parameterization in terms of vertex positions, momenta and decay times. The technique allows for the simultaneous extraction of this parameters and their uncertainties and correlations for all particles in the decay chain [32]. In addition, composite particle candidates are fitted with a constrain to the nominal interaction point. This constrain takes the uncertainty in that point into account, where the uncertainty is increased such that a transverse flight length for a B meson is included.

During the reconstruction steps a couple of very loose cuts on invariant masses of the different meson candidates and on the fit probabilities are done to limit the size of the data files[2], but all of them are tightened in the following step of the analysis and presented in a later subsection and are therefore not explicitly showed here.

4.2.2 Event Shape Variables

Event shape variables are used to separate $B\overline{B}$ events from $q\overline{q}$ events, because of the differences in their characteristic topologies. In a $B\overline{B}$ event, the primary e^+e^- pair from the collider produces the $B\overline{B}$ pair via the $\Upsilon(4S)$ resonance. In the $\Upsilon(4S)$ rest frame, the B mesons have low momenta, such that the decay of each B meson is nearly isotropic. The event shape for a continuum event ($u\overline{u}$, $d\overline{d}$, $s\overline{s}$ and $c\overline{c}$) has a pronounced two-jet structure, therewith is a strongly preferred direction characterizing the whole event.

Two variables, used to describe the event shape, are for example the thrust axis $\hat{T}$ and the thrust T, where the bases for each variable can be all particles in the whole event or sub sets of particles like all particles belonging to a B meson candidate. The thrust axis is defined to be the direction which maximizes the sum of the longitudinal momenta of the particles. Thrust is related to this direction by

$$T = \frac{\sum\limits_i |\hat{T} \cdot \mathbf{p}_i|}{\sum\limits_i |\mathbf{p}_i|}$$

where $\mathbf{p}_i$ is the 3-momentum-vector for a particle i used to determine $\hat{T}$. The allowed range of T is from 0.5 to 1, where $T \sim 1$ corresponds to a highly directional event, and $T \sim 0.5$ corresponds to an isotropic event. More on event shape variables and typical distributions can be found in [3].

The variables used in this analysis to describe the event shape are

[2] The B meson candidates and daughter particles are stored with their linking to each other as objects in ROOT files.

1. $|\cos\theta_B| = |\cos(\vec{p}_B, \vec{z})|$, the unsigned cosine of the angle between the B meson candidate momentum and the beam axis (z).

2. $|\cos\theta_C|$, the unsigned cosine of the angle between the B meson candidate thrust axis and the beam axis(z).

3. $L_0 = \sum_{i\in\mathrm{ROE}} p_i$, the zeroth Legendre polynomial weighted by the particle momenta. Where p_i is the magnitude of the momentum of i-th neutral or charged particle in the Rest-of-the-event (ROE) not associated with the reconstructed signal B candidate.

4. $L_2 = \sum_{i\in\mathrm{ROE}} \frac{1}{2}(3\cos^2(\theta_i)-1)p_i$, the 2nd Legendre polynomial weighted by the particle momenta. The angle θ is the angle of the i-th track with respect to the B candidate thrust axis.

5. $|\cos\theta_{\mathrm{T}}|$, the unsigned cosine of the angle between the B meson candidate thrust axis and the thrust axis formed from the ROE.

All the above quantities are computed in the center of mass system of the $\Upsilon(4S)$ resonance. It is to note that the distribution of $|\cos\theta_B|$ shows a $\sin^2\theta$ shape for $B\overline{B}$ events, whereas it is flat for $q\overline{q}$ events.

Four event shape variables enter the multivariate maximum likelihood fit analysis, described later in section 4.4, as a combined discriminating input variable. The event shape variables x_i, where x_i is $|\cos\theta_B|$, $|\cos\theta_C|$, L_0 or L_2 are combined into a linear Fisher discriminate:

$$\mathcal{F} = \sum_{i=1}^{4} \lambda_i\, x_i\,,$$

where the goal of the Fisher technique is to determine the coefficients λ_i so as to maximize the separation between a signal and background sample [35]. The values for λ_i are the numbers used in almost all charmless quasi-two-body analyses at *BABAR* and have been trained on a set of different decay channels [36]. For this analysis separately coefficients have been trained on MC to some extent and found to be consistent in terms of separation ability for signal and background test samples. Remaining differences can be lead back to the different training samples and software packages[3], leading mostly to different scaling and offset values.

[3]TMVA vs Cornelius++.

Table 4.2: *Summary of the selection requirements for the decay* $B^+ \rightarrow a_1^+ K^{*0}$. *For details on the selection requirements see text.*

Criterion	Requirement
$\lvert\cos\theta_{\mathrm{T}}\rvert$	≤ 0.8
Fisher	$-2 \leq \mathcal{F} \leq 2$
B fit probability	≥ 0.01
K_0^* helicity angle	$-0.98 \leq \mathcal{H}_{K^*} \leq 0.8$
m_{ρ^0}	$0.55 \leq m_{\rho^0} \leq 1$ GeV/c^2
$m_{K_0^*}$	$0.8 \leq m_{K_0^*} \leq 1$ GeV/c^2
$m_{a_1^+}$	$0.9 \leq m_{a_1^+} \leq 1.8$ GeV/c^2
m_{ES}	$5.25 \leq m_{\mathrm{ES}} \leq 5.29$ GeV/c^2
ΔE	$-0.1 \leq \Delta E \leq 0.1$ GeV

The question of using other or more than these four variables in the Fisher discriminate has been addressed before and it was shown that adding some other variables, e.g. variables providing information about the quark content of the other B meson in the $\Upsilon(4S)$ decay, can provide a 5% improvement in separation for some of them, but would result in a more complicated analysis structure, so using only the four variables is preferred for its simplicity [36].

4.2.3 Event Selection

This section summarizes the requirements for the selection criterions. The cuts have not been formally optimized. The reasons for this are the parameterization for a variable in one of the different components for the fit can be simplified by cutting away a critical region. The final sample of background and signal events in the final fit must have a reasonable size, a large sample can increase the time for fitting procedures to a intolerable amount, while a small sample can lead to less significant signal. Therefore, one aims for a balanced sample to enter the maximum likelihood fit. The compatibility with the used skim and with other analyses in the same field for comparison is also considered. But in principle all cuts reduce the various background while keeping the signal reduction small.

All selection criteria and the requirements for the decay $B^+ \rightarrow a_1^+ K^{*0}$ are summarized in table 4.2 and are discussed here. The definition for the event shape variable $|\cos\theta_{\mathrm{T}}|$ is given in the previous section 4.2.2. $B\overline{B}$ events show a flat distribution in $\cos\theta_{\mathrm{T}}$, while continuum background events peak at ± 1. The $\cos\theta_{\mathrm{T}}$ thrust cut reduces mainly continuum background and thus is used to control the overall size of the fitted sample, since continuum background represent by far the largest background fraction. The distribution of the Fisher discriminant for signal and background can be described with a Gaussian function and lies for both in the range from -2 to $+2$. The cuts only defines the region for future procedures and removes events with artefacts from some calculation.

The B fit probability is the χ^2 fit probability from the least squares fit of the decay chain fit for composing the B meson candidates. The allowed range is from 0 to 1 and for correct reconstructed B meson candidates the distribution is flat, while it is sharply peaking at zero for improper fit results. Therefor the fit probability is required to be greater than 0.01.

The K_0^* helicity $\mathcal{H}_{K^*}$ is defined and its theoretical distribution is shown in section 2.4. The $\mathcal{H}_{K^*}$ distributions for longitudinal and transversal polarized signal MC, longitudinal and transversal polarized $B^+ \to a_2^+ K^{*0}$ MC, continuum background, charmless $B\overline{B}$ background MC and charm $B\overline{B}$ background MC before applying the helicity cut are shown in figure 4.1. The requirement $\mathcal{H}_{K^*} \leq 0.8$ for the helicity angle is designed to reduce charmless background, because the charmless background is prominently peaking in this region (cp. figure 4.1 distribution (f)). This requirement nearly pushes down the charmless background to half of its original size. The requirement $-0.98 \leq \mathcal{H}_{K^*}$ for the helicity angle removes artificial peaking effects during the parameterization of K_0^* helicity variable for the fitting procedure. The generated input helicity distributions $\mathcal{H}_{K^*}$ and $\mathcal{H}_{a_1}$ are show in figure 4.2 for signal MC and in figure 4.3 for $B \to a_2 K^*$, respectively. The variable m_{ρ^0} is the mass of the intermediate $\pi^+\pi^-$ state. The lower m_{ρ^0} cut excludes K_S^0-mesons and lowers the charm and continuum background, as well as reducing the combinatoric background. $m_{K^*_{0\,K^+\pi^-}}$ is the mass of the K^* meson candidate reconstructed with K^+ and π^- meson candidates. The cuts on the mass reduces various backgrounds and simplifies the parameterization for the background components. The variable $m_{a_1^+}$ is the mass of the reconstructed a_1 meson candidate. The requirement $m_{a_1^+} \leq 1.8\,\mathrm{GeV}/c^2$ reduces the charm background, because the charm background is strongly rising in this region. This is taken from figure 4.4, where the a_1 mass distribution for charm background MC and $B^+ \to a_1^+ K^{*0}$ signal MC is shown. The requirements for the selection of the the $m_{a_1^+}$ region lead to a simpler parameterization for almost all background components.

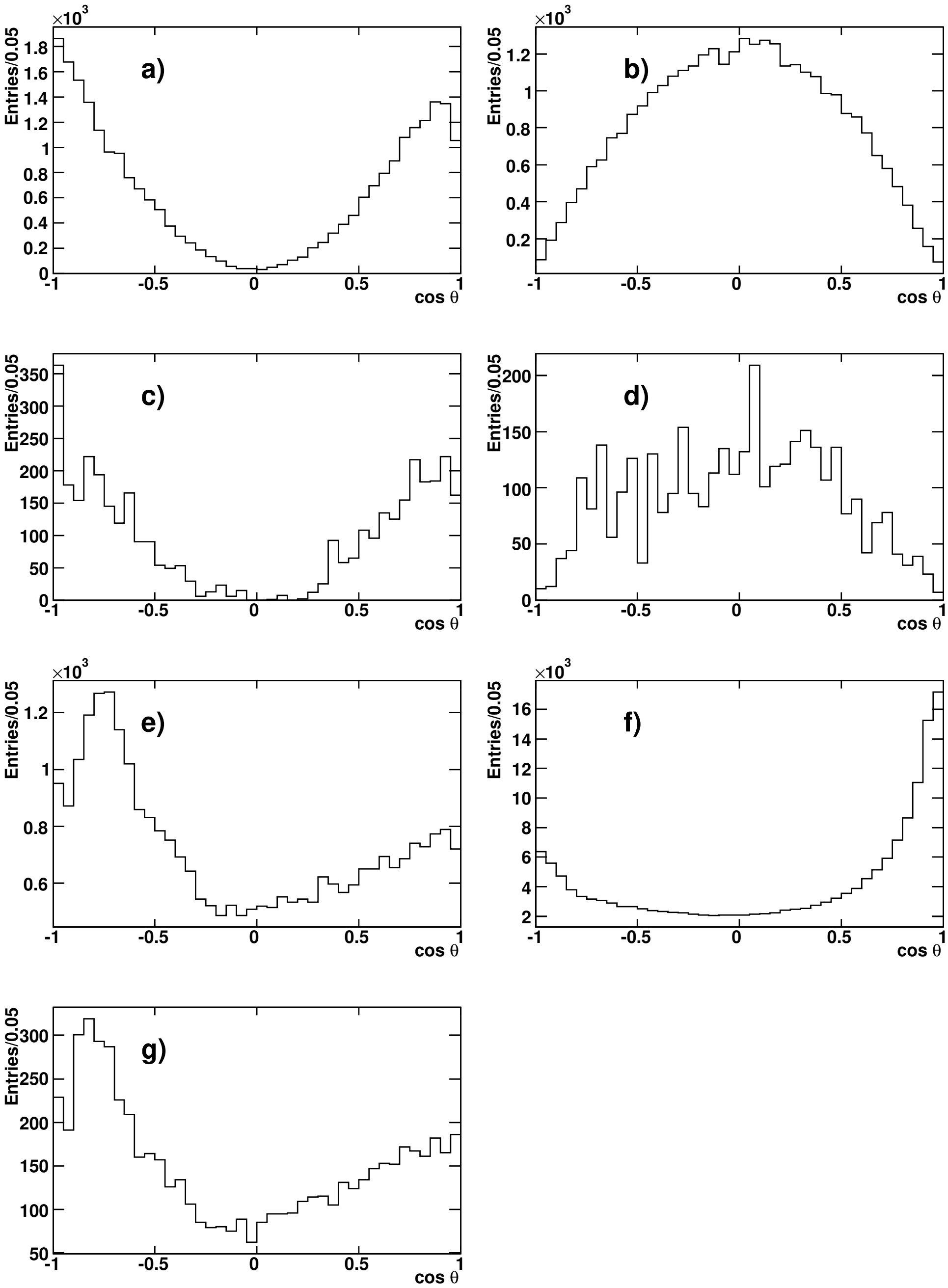

Figure 4.1: *Cosine of the K_0^* helicity angle $\mathcal{H}_{K^*}$ before applying the selection requirement $-0.98 \leq \mathcal{H}_{K^*} \leq 0.8$ for longitudinal (a) and transversal polarized signal MC (b), longitudinal (c) and transversal polarized $B^+ \rightarrow a_2^+ K^{*0}$ MC (d), continuum background (e) taken from ΔE data sideband, charmless $B\overline{B}$ background MC (f) and charm $B\overline{B}$ background MC (g). The K_0^* helicity angle is defined in section 2.4. Details for background are given in section 4.3.*

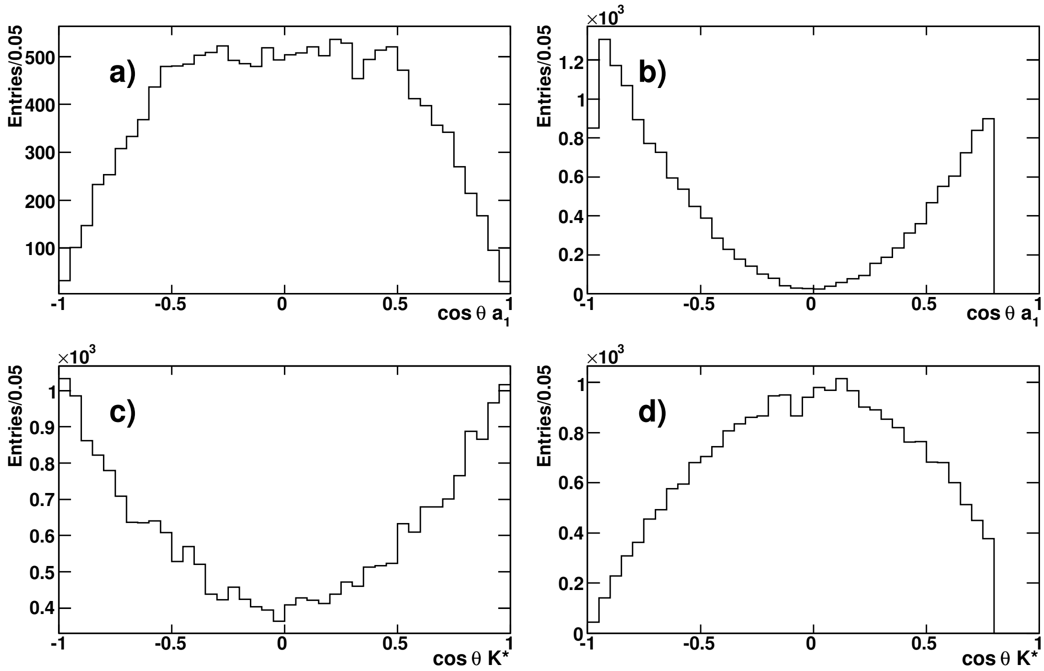

Figure 4.2: *The $\mathcal{H}_{a_1}$ distribution for longitudinal (a) and transversal (c) polarized signal MC. And the $\mathcal{H}_{K^*}$ distribution for for longitudinal (b) and transversal (d) polarized signal MC. The $\mathcal{H}_{K^*}$ distribution is affected by the $\mathcal{H}_{K^*} < 0.8$ selection requirement (see section 4.2).*

The kinematic variables m_{ES} and ΔE are defined in the beginning of this section. Both variables are most sensitive to separate between signal and background. All cuts on the variables provide simplification for the parameterization and remove backgrounds. The cuts could be chosen much tighter and would decrease the amount of background, but the two variables are also used to select the continuum background from the m_{ES} and ΔE sideband data sample and are chosen this way to provide a reasonable size to be able to model the continuum background component for the maximum likelihood fit. It was pointed out in various other BABAR analyses that it is necessary to correct the m_{ES} value [37, 38, 39]. The proper correction values are applied for the data sample and the endpoint for the m_{ES} continuum background is fixed for the parameterization[4]. Further investigations lead to the conclusion that applying corrections for the

[4]Fitting the m_{ES} for continuum background while floating the ARGUS function endpoint leads to the endpoint value $5.28966\,\mathrm{GeV}/c^2$. For ARGUS function and parameterization see section 4.4.1.

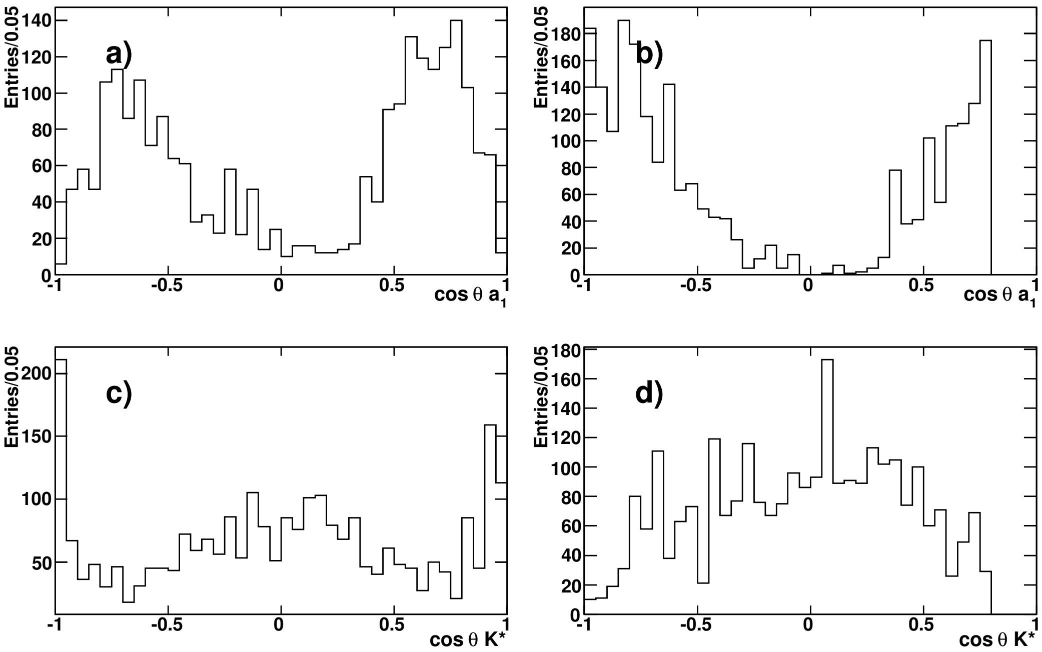

Figure 4.3: *The $\mathcal{H}_{a_1}$ distribution for longitudinal (a) and transversal (c) polarized $B^+ \to a_2^+ K^{*0}$ MC. And the $\mathcal{H}_{K^*}$ distribution for for longitudinal (b) and transversal (d) polarized $B^+ \to a_2^+ K^{*0}$ MC. The $\mathcal{H}_{K^*}$ distribution is affected by the $\mathcal{H}_{K^*} < 0.8$ selection requirement (see section 4.2).*

m_{ES} value on the MC sample is not necessary [40].

Decays of D mesons are a possible source of background to the signal channel. Therefore a so-called D-Veto is constructed. The details are described later with the charm background component itself in section 4.3.2.

4.2.4 Best Candidate Selection

After selecting signal like events passing the selection criteria given above in table 4.2, there is in almost every event more than one B candidate reconstructed. On average these are 2.4 candidates per event for longitudinal polarized signal MC, 2.0 candidates per event for transverse polarized signal MC and 1.5 candidates per event for On-Peak data.

Three different methods of selecting the best B meson candidate are presented

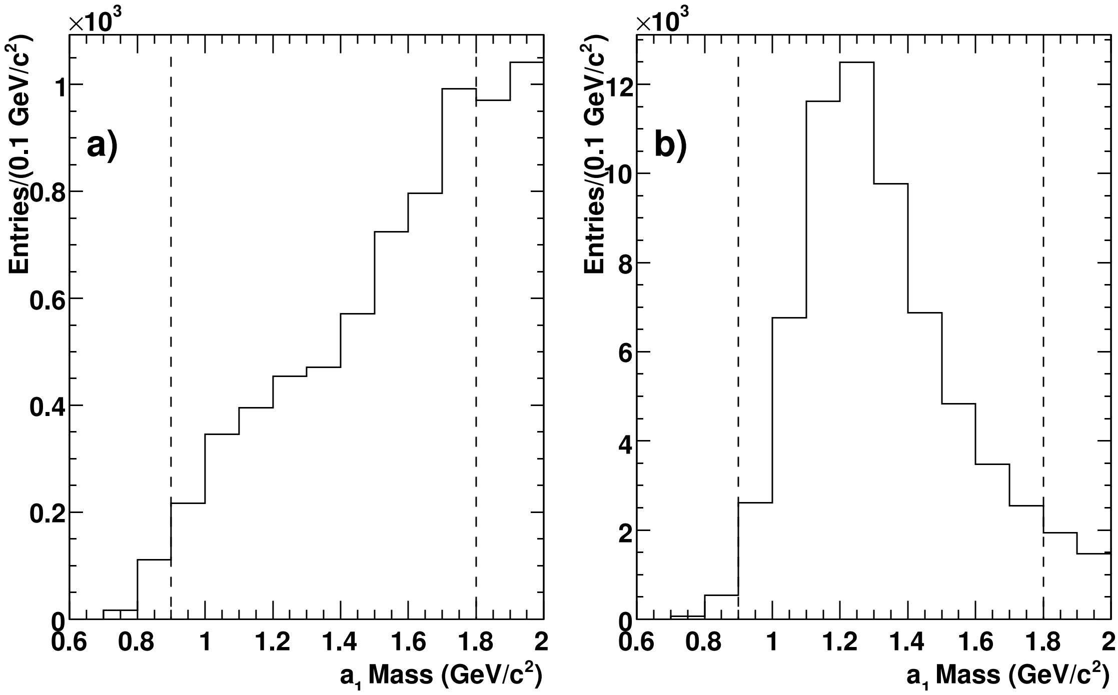

Figure 4.4: *The a_1 mass distribution for charm background MC (a) and for $B^+ \to a_1^+ K^{*0}$ signal MC (b). The dashed lines indicate the selection requirements used in the analysis on the a_1 meson candidate mass.*

here and compared to each other. The three methods are based on the same input variables. The variables used are the intermediate ρ candidate mass and the χ^2-fit probabilities from the B-, a_1- and K_0^*-vertex fit, taken from the decay chain fit for B meson candidate composition. To be sure not to introduce a bias and systematic error to the measurement, these variables are not used further more in the maximum likelihood fit. The first approach calculates a χ^2 deviation, where the χ^2 is defined as $\chi^2 = \sum_i (e_i - x_i)^2$, whereas e_i represent the expected value for one of the variables x_i. For this approach the difference from the reconstructed ρ meson candidate mass with respect to the nominal ρ meson mass [4] is used for calculating the χ^2 value and in case of the three fit probabilities the difference to 1 is used. The two other approaches are based on multivariate classification techniques. One of the methods is based on a non-linear discriminant technique and is an artificial neural network [41, 42], which belongs to the class of multi-layer perceptions (MLP). The third approach is a Boosted Decision Tree (BDT), that is a decision tree with the feature to give boosted weights to a misclassified event in order to build up a new tree with new weights; so the decision tree learns from mistakes in a previous version [43]. The MLP and BDT methods are implemented using the TMVA framework [44] and have been trained on truth matched signal events, non-truth matched signal events, and background samples.

The truth match is provided by a algorithm that finds the best match between the properties for a particle from generated level and the reconstructed ones in MC. In particular, the pion permutation inside the a_1 meson is problematic, for the analysis all possible permutations of the pions used for the a_1 meson candidate reconstruction are considered as truth-matched if they truly belong to the a_1 meson. For signal MC where candidate particles are exchanged with a ROE particle the resulting B meson candidate is considered as not-truth matched. Such kind of a B meson candidate is so-called self-cross-feed. The self-cross-feed fraction (SCF) for the analysis is defined as number of not-truth matched signal events over the number of all selected signal events.

The different methods are compared in Table 4.3 for longitudinal and transversal polarized signal MC. And the self-cross-feed fraction is used as criterion for

Table 4.3: *Self-cross-feed fraction (SCF) in % for longitudinal and transversal polarized signal MC events. Compared are three different methods used to select a best B meson candidate. The methods shown are Multi-layer Perceptions Artificial Neural Network (MLP), Boosted Decision Tree (BDT) and χ^2 approach (χ^2). For more details on methods and SCF see text.*

Method	SCF for longitudinal signal in %	SCF for transversal signal in %
MLP	21.7	12.9
BDT	21.9	13.1
χ^2	22.8	13.5

the comparison in the table.

For the analysis the method with the lowest SCF is used to select the best B meson candidate. This is the method based on MLP. In order to prove that the B candidate selection based on a MLP works properly the performance is shown in figure 4.5. In this figure m_{ES} with and without best B meson candidate selection for signal event MC and the intermediate ρ meson candidate mass for On-Peak

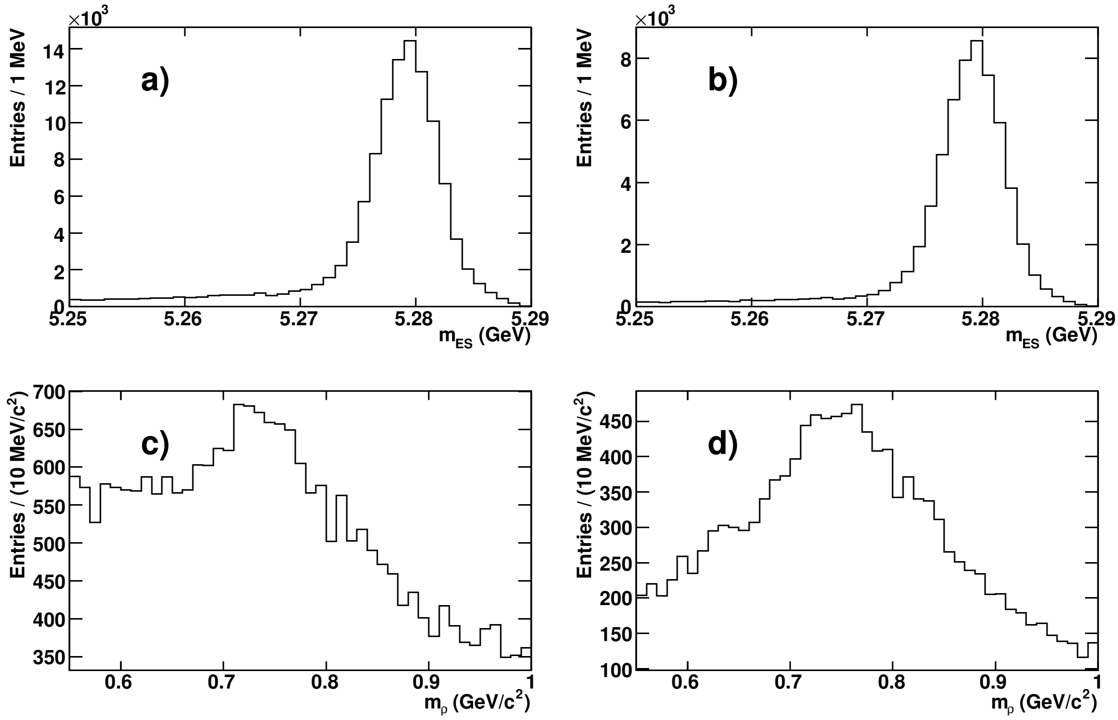

Figure 4.5: *Performence of best B meson candidate selection based on a MLP approach. The upper row shows the m_{ES} distribution for signal MC events, on the left hand side without (a) and on the right hand side with best B meson candidate selection (b). The lower row shows the intermediate ρ candidate mass distribution for On-Peak data, on the left hand side without (c) and on the right hand side with best B meson candidate selection (d). The distribution (c) and (d) for On-Peak data has been obtained and added after the results of the final likelihood fit was validated to work properly.*

data is presented. The comparison between the two plots (a and b) in the upper row gives a lower level for the background, which can be seen on the side left to the peak. The intermediate ρ candidate mass distribution takes shape after the best B candidate selection, shown in the lower row in figure 4.5.

4.2.5 Selection Efficiencies

The raw selection efficiency ϵ is determined by the ratio of the signal MC events passing all selection criteria to the total number of generated signal MC events.

The numbers for longitudinal and transversal polarized signal MC are different in general and the strong requirement on the $\mathcal{H}_{K^*}$ variable affects the longitudinal polarized signal by far stronger (cp. table 4.2 and 4.1), thus one expects a lower efficiency for longitudinal polarize signal MC. The raw selection efficiencies are $\epsilon_L = 12.9\%$ for longitudinal polarized signal MC and $\epsilon_T = 18.6\%$ for transversal polarized signal MC. To obtain the final efficiency, the MC efficiency has to be corrected for the known resonance branching fraction since the channel of interest is forced to decay into the signal channel. The correction is obtained from isospin formalism with the Clebsch-Gordan coefficients table [4]. A factor $\frac{2}{3}$ arise from the K^{*0} and a factor of $\frac{1}{2}$ from the a_1 sub-decay:

$$\prod \mathcal{B}_i = \frac{2}{3} \cdot \frac{1}{2} = \frac{1}{3}\,.$$

This leads to the final efficiency of 4.3% for the longitudinal polarized signal MC and 6.2% for the transversal signal MC.

The average raw efficiency is 15.9% and is obtained by running the selection code for a combined simulated data set; from this follows the average efficiency 5.3%. The average efficiency is later used to estimate the number of signal events for validation studies. There is no separate treatment to obtain a trigger efficiency, since the trigger efficiency is greater than 99% for $B\overline{B}$ events (cp. section 3.6). Table 4.4 summarizes the absolute number of selected events for longitudinal polarized signal MC, transversal polarized signal MC, continuum events, and $B\overline{B}$ generated MC events for different steps during the selection.

4.3 Backgrounds

The background arising for the $B^+ \to a_1^+\ K^{*0}$ analysis is classified into different background components as fit categories. These background components are discussed in this section. Charmless background is background from B meson decays without a $b \to c$ quark transition. Charm background is background from B meson decays with a $b \to c$ quark transition. Continuum background is background from the initial e^+e^- annihilation decaying non-resonant into $q\overline{q}$ pairs. $B^+ \to a_2^+ K^{*0}$ background is special decay mode separated from the charmless background. The components are treated separately since they are different in terms of the shapes for the discriminating variables in the likelihood fit, the creation of the samples, and the specific action involved to reduce the size of the component.

Table 4.4: *Summary of absolute numbers of selected events for longitudinal polarized signal MC, transversal polarized signal MC, continuum background events from ΔE sideband data and generic $B\overline{B}$ MC events after applying a certain levels of the selection requirements, where the selection for a row includes the selection requirements from the rows above. The D-Veto shown in the last row is explained with the charm background in section 4.3.2.*

Selection	longitudinal signal MC	transversal signal MC	continuum background	generic $B\overline{B}$ MC
Generated	195k	195k	-	1387M
Trigger & Reconstruction	84903	87902	2150563	233140
$\cos\theta_{\mathrm{T}}$, $\mathcal{F}$	65116	67784	333920	145382
PID	51104	54507	104334	59049
Fit Probabilities	47275	50503	86188	47375
m_{ρ^0}	45267	48891	64117	36780
$m_{K^{*0}}$	42222	45980	44063	24940
m_{a_1}	39787	43588	35636	18815
K_0^* helicity	30319	42212	31533	16239
m_{ES} and ΔE	27367	39111	10717	7675
D-Veto	25279	36249	9538	6652

4.3.1 Charmless $B\overline{B}$ Background

Prominent decays of a B meson involve a $b \to c$ quark transition. B meson decays without such a $b \to c$ transition are called charmless and can be very similar to the signal decay. Since most of the charmless $B\overline{B}$ background decays are rare B meson decays they are probably not statistically sufficiently represented in the generic $B\overline{B}$ MC sample. This is also driven by the fact that the selection efficiency for a background mode is not as large as for the signal. A background sample with a reasonable size is also needed for fit validation to have a number of independent samples.

The following procedure is done to obtain a representative charmless $B\overline{B}$ background sample. The full analysis selection is applied to the generic $B\overline{B}$ data sample (see section 4.1), where $b \to c$ background and signal events are removed in order to focus on charmless background modes. This provides a long list with many charmless B decays. In addition, similar charmless B decays missing in the list are added to the list by hand. For every decay channel in the list, a MC sample is generated where one of the B meson from the $\Upsilon(4S)$ decay is forced to decay accordingly to the charmless decay channel; the reconstruction and selection is then applied to this MC sample. The number of generated events for each of the background modes are of the same order as the signal decay sample, but varies for the different decay channels. The selected events from the samples are mixed together in appropriate proportions depending on the estimated branching fraction for the decay channel. Therefore, the expected number of events in $B\overline{B}$ background is estimated by taking into account the number of B mesons pairs in data, the branching fraction for the mode, the product branching fraction for the mode, as the decay mode is forced for the generation, and the calculated efficiency for the mode. The expected number of charmless events entering the maximum likelihood fit is 360. Due to the limited total size for some modes, the size of the charmless cocktail is 1716 events in total. This is about five times the number of charmless events expected as background. The composition of the charmless cocktail sorted by the total number of events for each mode in the cocktail is given in table 4.5.

Table 4.5: *Charmless $B\overline{B}$ backgrounds to the decay $B^+ \to a_1^+ K^{*0}$. For each background channel considered, listed are the raw selection efficiency (MC ϵ) in %, the estimated branching fraction Est.$\mathcal{B}$ in units of 10^{-6}, the product branching fraction $\prod \mathcal{B}_i$, the expected number of events in $B\overline{B}$ background (Exp. in $B\overline{B}$ Bkg.) and the number of events in the charmless cocktail (# in file). A star instead of a error for estimated branching fraction indicates that indeed the branching fraction for this mode is estimated. In case of errors the latest known values to* BaBar *are used. The abbreviation (nr) stands for non-resonant. The numbers of events in the table are rounded for the presentation in the table.*

Background channel	MC ϵ (%)	$Est.\mathcal{B}$ (10^{-6})	$\prod \mathcal{B}_i$	Exp. in $B\overline{B}$ Bkg.	# in file
$B^0 \to K^{*0}_{K^+\pi^-}\pi^+\pi^-$ (nr)	0.32	$48.0^{+5.2}_{-5.2}$	0.667	47	234
$B^0 \to a_1^0 K^{*0}$	1.88	7.0^*	0.667	41	204
$B^+ \to K^{*0}_{K^+\pi^-}\pi^+\pi^0$ (nr)	0.14	40.0^*	0.667	17	85
$B^+ \to a_1^+(\rho^0\pi^+)\rho^0$	0.37	16.0^*	0.5	14	69
$B^0 \to a_1^0 K^{*0}$	1.30	3.0^*	0.667	12	60
$B^0 \to \rho^0 K^{*0}_{K^+\pi^-}$	1.17	$2.8^{+0.8}_{-0.8}$	0.667	10	50
$B^0 \to \eta'_{\rho\gamma} K^{*0}_{K^+\pi^-}$	2.81	$3.8^{+1.2}_{-1.2}$	0.197	10	48
$B^+ \to \rho\ K_0^*(1430)$	0.05	40.0^*	1.0	10	48
$B^0 \to \rho^0 K^{*0}_{K^+\pi^-}$	1.05	$2.8^{+0.8}_{-0.8}$	0.667	9	45
$B^+ \to a_1^+(\rho^+\pi^0)K^{*0}$	0.25	14.0^*	0.444	7	36
$B^0 \to a_1^+(\rho^0\pi^+)a_1^-(\rho^0\pi^-)$	0.10	64.0^*	0.25	7	35
$B^0 \to K^{*0}_{K^+\pi^-}K^+K^-$ (nr)	0.11	20.0^*	0.667	7	34
$B^+ \to \rho^+\ K^{*0}_{K^+\pi^-}$	0.47	$4.6^{+0.75}_{-0.75}$	0.666	7	33
$B^+ \to \rho^+\ K^{*0}_{K^+\pi^-}$	0.46	$4.6^{+0.75}_{-0.75}$	0.666	7	32
$B^0 \to \rho\ K_0^*(1430)$	0.07	20.0^*	1.0	6	30
$B^0 \to \eta_{3\pi} K^{*0}_{K^+\pi^-}$	0.54	$15.9^{+1.0}_{-1.0}$	0.151	6	30
$B^0 \to \omega\pi^- K^+$ (nr)	0.14	$10.0^{+4.0}_{-4.0}$	0.891	6	29
$B^0 \to \phi\rho^0$	0.39	$6.5^{+6.5}_{-6.5}$	0.491	6	29

(Table 4.5 continued.)

Background channel	MC ϵ (%)	$Est.\mathcal{B}$ (10^{-6})	$\prod \mathcal{B}_i$	Exp. in $B\overline{B}$ Bkg.	# in file
$B^0 \to \rho^0\pi^- K^+$	0.11	10.0^*	1.0	5	26
$B^0 \to \phi_{3\pi} K^{*0}_{K^+\pi^-}$	2.25	$4.75^{+0.4}_{-0.4}$	0.103	5	25
$B^0 \to K^{*0}_{K^+\pi^-}\rho^-\pi^+$	0.33	5.0^*	0.667	5	25
$B^0 \to \rho^0\pi^0 K^{*0}_{K^+\pi^-}\rho^0\pi^0$	0.31	5.0^*	0.667	5	23
$B^0 \to \omega\ K^{*0}_{K^+\pi^-}$	0.70	$2.4^{+1.3}_{-1.3}$	0.594	5	23
$B^0 \to K^{*0}_{K^+\pi^-}\rho^+\pi^-$	0.30	5.0^*	0.667	5	23
$B^0 \to f_0 K^{*0}_{K^+\pi^-}$	0.95	$2.15^{+2.15}_{-2.15}$	0.444	4	20
$B^+ \to K^{*+}_{K^+\pi^0}\pi^+\pi^-$ (nr)	0.04	$70.3^{+10.1}_{-10.1}$	0.333	4	20
$B^+ \to K^+\pi^-\pi^+$	0.02	$54.8^{+2.9}_{-2.9}$	1.0	4	19
$B^0 \to \phi_{3\pi} K^{*0}_{K^+\pi^-}$	1.73	$4.75^{+0.4}_{-0.4}$	0.103	4	19
$B^+ \to a_1^0 K^+$	0.04	20.0^*	1.0	4	18
$B^0 \to K(1680)\rho$	0.08	10.0^*	1.0	4	17
$B^+ \to \eta'_{\rho\gamma} K^+$	0.04	$70.2^{+2.5}_{-2.5}$	0.295	3	17
$B^0 \to \phi\ K^{*0}_{K^+\pi^-}$	0.47	$4.75^{+0.4}_{-0.4}$	0.327	3	16
$B^0 \to \phi\ K^{*0}_{K^+\pi^-}$	0.47	$4.75^{+0.4}_{-0.4}$	0.327	3	16
$B^0 \to a_1^-(\rho^0\pi^-)K^+$	0.08	$16.3^{+3.7}_{-3.7}$	0.5	3	15
$B^+ \to \phi\rho^+$	0.08	$8.0^{+8.0}_{-8.0}$	1.0	3	15
$B^0 \to a_1^-(\rho^0\pi^-)K^{*+}_{K^+\pi^0}$	0.18	20.0^*	0.167	3	13
$B^0 \to \eta\ K^+\pi^-$ (nr)	0.03	20.0^*	1.0	3	12
$B^+ \to a_1^+(\rho^0\pi^+)a_1^0$	0.04	49.0^*	0.25	2	11
$B^0 \to a_1^+(\rho^0\pi^+)\rho^-$	0.03	$31.4^{+26.6}_{-31.0}$	0.5	2	11
$B^+ \to K^+K^-K^+$	0.01	$32.5^{+1.5}_{-1.5}$	1.0	2	10
$B^\pm \to K_0^*(1430)\pi$	< 0.01	$47.1^{+4.5}_{-4.6}$	1.5	2	10
$B^\pm \to K^*(1680)\pi$	0.03	$6.0^{+6.0}_{-6.0}$	2.0	2	9
$B^\pm \to K(1680)\rho$	0.04	10.0^*	1.0	2	9
$B^+ \to \rho^+\pi^- K^+$	0.04	10.0^*	1.0	2	8
$B^0 \to \phi\ K^{*0}_{K\pi}$ *odd*	0.47	$2.4^{+0.23}_{-0.23}$	0.327	2	8
$B^0 \to a_1^+\pi^-$	0.01	$31.7^{+3.7}_{-3.7}$	1.0	2	8
$B^0 \to a_1^-(\rho^0\pi^-)\pi^+$	0.02	$31.7^{+3.7}_{-3.7}$	0.5	1	7

(Table 4.5 continued.)

Background channel	MC ϵ (%)	$Est.\mathcal{B}$ (10^{-6})	$\prod \mathcal{B}_i$	Exp. in $B\overline{B}$ Bkg.	# in file
$B^0 \rightarrow\ a_1^+(\rho^0\pi^+)\pi^-$	0.02	$31.7^{+3.7}_{-3.7}$	0.5	1	7
$B^0 \rightarrow\ K^*(1680)\pi$	0.04	$5.0^{+5.0}_{-5.0}$	1.5	1	7
$B^+ \rightarrow\ a_1^+\pi^-\pi^+$	0.03	10.0^*	1.0	1	7
$B^+ \rightarrow \rho^+\rho^0$	0.02	$18.3^{+3.4}_{-3.4}$	0.96	1	6
$B^+ \rightarrow\ a_1^+(\rho^+\pi^0)K^{*0}$	0.11	6.0^*	0.444	1	6
$B^0 \rightarrow \overline{K}^{*0}_{K\pi}K^{*0}_{K\pi}$	1.28	$0.49^{+0.17}_{-0.14}$	0.444	1	6
$B^0 \rightarrow \rho^0\rho^+\pi^-\ (nr)$	0.03	10.0^*	1.0	1	6
$B^+ \rightarrow\ a_1^0K^{*+}_{K^+\pi^0}$	0.07	10.0^*	0.333	1	5
$B^0 \rightarrow\ K^+\pi^-\pi^0$	< 0.01	$36.6^{+5.2}_{-5.2}$	1.0	1	5
$B^+ \rightarrow\ a_1^+(\rho^0\pi^+)\omega$	0.03	20.0^*	0.445	1	5
$B^0 \rightarrow \rho^0\rho^+\pi^-$	0.02	10.0^*	1.0	1	4
$B^0 \rightarrow\ K_2^{*+}(1430)pi-$	0.06	$3.15^{+3.15}_{-3.15}$	1.0	1	4
$B^+ \rightarrow\ K^{*0}_{K^+\pi^-}\pi^+$	0.02	$10.7^{+0.8}_{-0.8}$	0.667	1	3
$B^0 \rightarrow\ b_1^+(\omega\pi^+)K^-$	0.02	$7.4^{+1.4}_{-1.4}$	0.891	1	3
$B^0 \rightarrow\ b_1^+(\omega\pi^+)K^-$	0.02	$7.4^{+1.4}_{-1.4}$	0.891	1	3
$B^+ \rightarrow \rho^0\pi^0\ K^+$	0.03	5.0^*	1.0	1	3
$B^+ \rightarrow\ a_1^0\pi^+$	< 0.01	$20.4^{+5.8}_{-5.8}$	1.0	1	3
$B^0 \rightarrow \phi\ K^{*0}_{K\pi}(1430)$	0.11	$4.6^{+0.9}_{-0.9}$	0.304	1	3
$B^0 \rightarrow \pi^-K_0^{*+}(1430)_{K^+\pi^0}$	< 0.01	$49.7^{+7.8}_{-9.0}$	0.31	1	3
$B^0 \rightarrow\ a_1^0\rho^0$	0.13	1.0^*	1.0	1	3
$B^+ \rightarrow \omega\ K^+$	0.02	$6.9^{+0.5}_{-0.5}$	0.891	1	2
$B^+ \rightarrow \rho^0K^{*+}_{K^+\pi^0}$	0.09	$3.6^{+1.9}_{-1.8}$	0.333	1	2
$B^0 \rightarrow \rho^+\ell^-\nu$	< 0.01	$220.0^{+40.0}_{-40.0}$	2.0	1	2
$B^+ \rightarrow\ K^{*+}_{K^0_S\pi}\pi^+\pi^-\ (nr)$	< 0.01	$70.3^{+10.1}_{-10.1}$	0.231	1	2
$B^+ \rightarrow\ f_0K^{*+}_{K^+\pi^0}$	0.08	$5.2^{+1.3}_{-1.3}$	0.222	1	2
$B^+ \rightarrow\ a_1^+(\rho^+\pi^0)\rho^0$	0.01	16.0^*	0.5	0	2
$B^+ \rightarrow\ a_1^0\rho^+$	0.01	16.0^*	0.5	0	2
$B^+ \rightarrow \omega\ell^-\nu$	< 0.01	$130.0^{+60.0}_{-60.0}$	1.0	0	2
$B^0 \rightarrow\ b_1^+(\omega\pi^+)\pi^-$	< 0.01	$10.9^{+1.5}_{-1.5}$	0.891	0	1

(Table 4.5 continued.)

Background channel	MC ϵ (%)	$Est.\mathcal{B}$ (10^{-6})	$\prod \mathcal{B}_i$	Exp. in $B\overline{B}$ Bkg.	# in file
$B^0 \to \rho^0\pi^+\pi^-$	0.02	5.0^*	1.0	0	1
$B^+ \to \omega\pi^+$	0.01	$6.7^{+0.6}_{-0.6}$	0.891	0	1
$B^+ \to K^{*+}_{K^+\pi^0}\rho^-\pi^+$	0.02	10.0^*	0.333	0	1
$B^+ \to \omega\ K^+\pi^0\ (nr)$	0.01	$6.0^{+3.0}_{-3.0}$	1.0	0	1
$B \to \eta'\ell\nu$	< 0.01	80.0^*	1.0	0	1
$B^0 \to a_1^-(\rho^-\pi^0)K^+$	< 0.01	$16.3^{+3.7}_{-3.7}$	0.5	0	1
$B^+ \to \pi^+\ell^-\nu$	< 0.01	$136.0^{+9.0}_{-9.0}$	2.0	0	1
$B^+ \to K^{*+}\overline{K}^{*0}$	0.12	2.0^*	0.222	0	1
$B^0 \to \rho^0\rho^0$	0.06	$0.86^{+0.28}_{-0.28}$	1.0	0	1
$B^0 \to K^{*0}_{K^+\pi^-}\gamma$	< 0.01	$40.1^{+2.0}_{-2.0}$	0.667	0	1
$B^0 \to a_1^-(\rho^-\pi^0)K^{*+}_{K^+\pi^0}$	0.02	20.0^*	0.167	0	1
$B^0 \to K_SK^-\pi^+$	0.01	$4.5^{+4.5}_{-4.5}$	1.0	0	1
$B^+ \to K^{*+}\overline{K}^{*0}$	0.16	2.0^*	0.154	0	1
$B^+ \to \eta'_{\rho\gamma}K^{*+}_{K^+\pi^0}$	0.10	$4.9^{+2.1}_{-1.9}$	0.098	0	1
$B^+ \to \phi_{3\pi}K^{*+}_{K^+\pi^0}$	0.03	$5.0^{+0.55}_{-0.55}$	0.333	0	1
$B^+ \to \eta'_{\rho\gamma}\rho^+$	0.02	$9.1^{+3.7}_{-2.8}$	0.295	0	1
$B^+ \to \omega\rho^+$	< 0.01	$8.7^{+2.1}_{-1.9}$	0.891	0	1
$B^+ \to K^{*+}_{K^+\pi^0}\rho^+\pi^-$	0.01	10.0^*	0.333	0	1
$B^0 \to \rho^+\rho^-$	< 0.01	$24.2^{+3.1}_{-3.2}$	0.96	0	1
$B^+ \to \rho^0\pi^+\pi^0$	< 0.01	10.0^*	1.0	0	1
$B^0 \to K^+K^-K^0$	< 0.01	$24.7^{+2.3}_{-2.3}$	0.346	0	1
$B^0 \to a_1^+\pi^-\pi^0$	< 0.01	10.0^*	1.0	0	1
$B^+ \to \rho^-\pi^0K^+$	< 0.01	10.0^*	1.0	0	1
Total				360	1716

This method to create a charmless cocktail is not perfect, since the generic MC does not include all possible charmless decay modes and as well as not all decay modes are available. Especially non-resonant B decays to $K^*\pi\pi\pi$ or $a_1K\pi$ are not represented in the charmless cocktail, but the contributions are expected to be small compared to the modes already represented in the charmless cocktail. E.g. the contribution from $B \to \rho\pi K^*$ is included in charmless cocktail and is small, due to the ρ reconstruction and selection requirements on the ρ mass; the contribution from $K^*\pi\pi\pi$ should be even smaller for an estimated branching fraction of the same size. It is known that the charmless cocktail is not perfect and this will be treated as a systematic error later in the analysis.

4.3.2 Charm $B\overline{B}$ Background and D-Veto

Most of the B meson decays involve a $b \to c$ quark transition. This can lead to B meson decays with D or D^* mesons, where the D^* decays to D with an additional π or a γ, in the final state. Other B meson decays that involve a $b \to c$ quark transition can produce e.g. D_s mesons or Λ_c baryons, which are not considered here. The D meson itself decays mainly to a K and a number of π mesons. Due to the 5 tracks in the signal final state and the width of the a_1 meson mass, decay products of the D and D^* mesons can be picked up and used for reconstruction. Therefore, charm B meson decays are treated as a additional background component. The charm background is not expected to significantly peaking in ΔE and m_{ES} variables, due to the different kinematic properties.

In order to specifically reduce the charm background, a so called D-veto is applied, that removes decays with a reconstructed D meson candidate. A dedicated D^* meson veto is not applied, but charm background with a D^* meson is removed with the D-veto due to the subsequent D^* meson decay to a D meson. For the D-veto neutral and charged D mesons candidates are reconstructed in parallel with the $B^+ \to a_1^+ K^{*0}$ signal decay chain and build up from the same kaon and pion lists, which are used for the $B^+ \to a_1^+ K^{*0}$ signal decay reconstruction. Due to performance in terms of purity and runtime, not all possible D meson decays are reconstructed; only the decays $D^0 \to K^-\pi^+$ and $D^+ \to K^-\pi^+\pi^+$ are considered. The D meson are composed from the K and pi candidate lists with a least squares decay chain fit [32]. It is required that the χ^2 fit probability is greater than 0.01 to remove improper fit result. For more details on the decay chain fit in general see section 4.2. Furthermore the D meson candidate mass is required to be $\pm 0.01\,\mathrm{GeV}/c^2$ around the nominal D mesons mass [4]. Figure 4.6 shows the D^+ meson mass distribution with requirements for the D-veto around the nominal D^+ meson mass. A B meson signal candidate is rejected if a pion track candidate used for the signal reconstruction is also used as a pion track for a charged or neutral D meson reconstruction.

The remaining charm background is treated as a separate component in the likelihood fit. For that component and for D-veto studies itself a charm $B\overline{B}$ background sample is necessary. To select the charm $B\overline{B}$ background sample from generic MC, the generated MC information is used. Every event in the generic sample is considered as a charm event if both generated B mesons decay into a final state containing a meson build up from a charm quark. This sample consists of 5184 events and it is later used for modeling the charm $B\overline{B}$ background component. From the sample size the number of expected charm $B\overline{B}$ background events for the fit is estimated. The expected number of charm

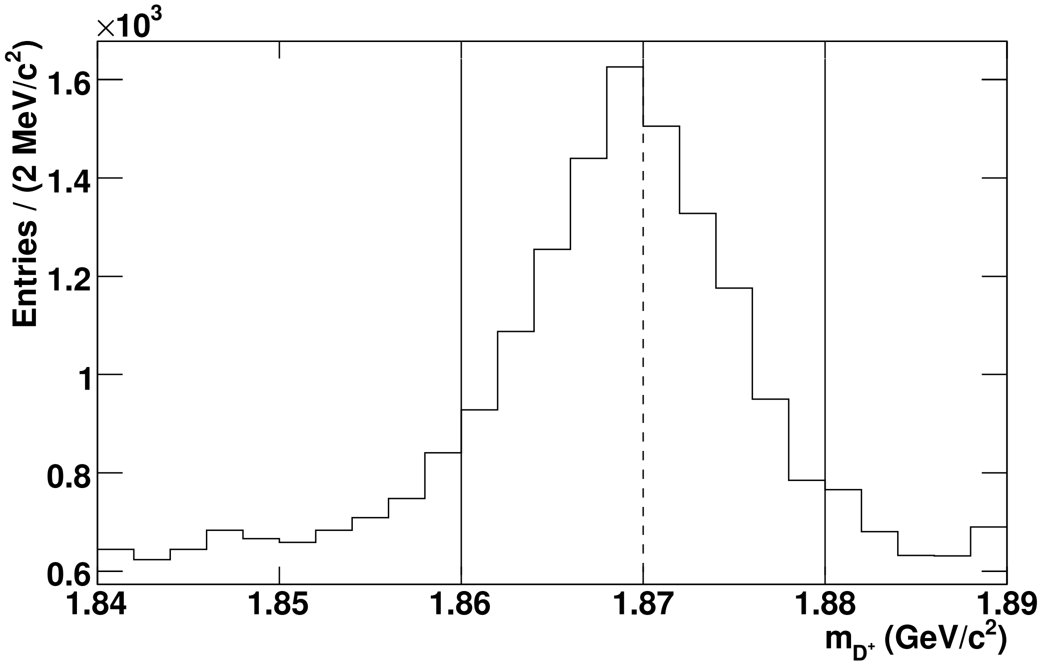

Figure 4.6: *The D^+ candidate mass distribution for generic $B\overline{B}$ MC. Indicated with lines are the mass requirements $\pm 0.01\,\mathrm{GeV}/c^2$ around the nominal D^+ meson mass and with dashed line the nominal D^+ meson mass.*

$B\overline{B}$ events is 1737 for the data sample.

4.3.3 Continuum Background

The largest background contribution to the $B \to a_1^+ K^{*0}$ decay is continuum background. This background arises from the initial e^+e^- annihilation not forming an $\Upsilon(4S)$ resonance but directly producing $q\overline{q}$ pairs. It is mostly the result of random combinations of tracks. Since no $B\overline{B}$ pairs are produced in this so-called continuum events, it is not peaking in m_{ES} and ΔE. Also the event shape variables are very good to control the continuum background. Within the likelihood fit this is guaranteed via the Fisher discriminate. The magnitude of the continuum background contribution is mainly reduced by cutting on the event shape variable $\cos\theta_{\mathrm{T}}$ (see section 4.2.2).

Contrary to the other backgrounds, the continuum background is determined from data. The continuum background sample is taken from the ΔE sideband.

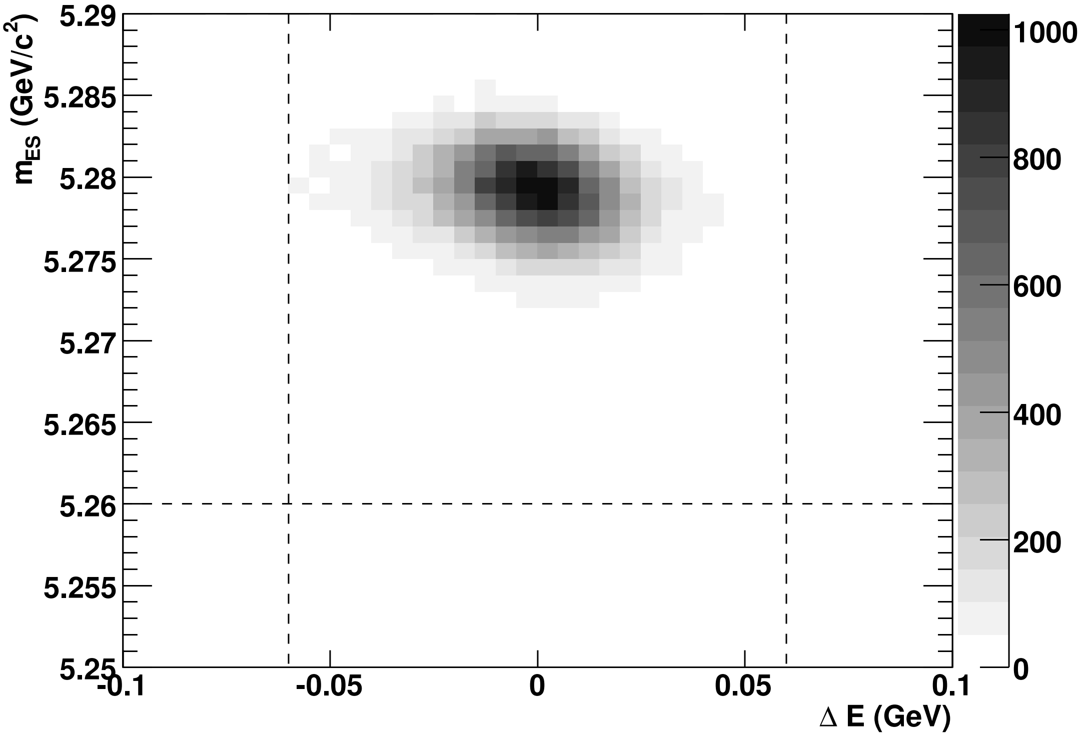

Figure 4.7: *The ΔE vs m_{ES} distribution for $B^+ \to a_1^+ K^{*0}$ signal MC. Indicated with lines are the sideband definitions for the continuum background sample.*

The ΔE sideband is defined as $|\Delta E| > 0.06$ GeV. In the case where the ΔE variable itself is examined or modeled for the likelihood fit the m_{ES} sideband is used. The m_{ES} sideband is defined as $m_{\text{ES}} < 5.26$ GeV/c^2. The definition for the sidebands is shown in figure 4.7 with $B^+ \to a_1^+ K^{*0}$ signal MC overlaid. With this definition almost no $B^+ \to a_1^+ K^{*0}$ signal events are expected to be found with in the continuum background sample. It is not fully excluded that in general as small number of $B\overline{B}$ events are not part of the continuum background sample.

4.3.4 $B^+ \to a_2^+ K^{*0}$ Background

The $a_2(1320)$ meson is very similar to the $a_1(1260)$ meson (cp. 2.6). The width of the a_2 meson is much smaller than for the a_1 meson and the central mass lies in the range of the a_1 mass. Therefore, a $B^+ \to a_2^+ K^{*0}$ decay is a possible source of background. The `EvtGen` decay model used for the decay is given in appendix

B. There are no branching fraction as well as polarization measurements for this decay available. Furthermore, no theoretical prediction is available. Other analyses of charmless B meson decays involving a_1 mesons did not observe a sizable a_2 meson contribution. The ad hoc conservative estimation for the branching fraction is $0.75 \cdot 10^{-6}$, that is as large as the measured $B^+ \to a_1^+ K^{*0}$ branching fraction. The average over longitudinal and transversal efficiency for the decay including the resonance branching fraction for an a_2 and a K^{*0} meson is 5.5%. The expected number of $B^+ \to a_2^+ K^{*0}$ decays is 19 events for the size of the given dataset. In principle, this component can be treated as separated signal component to measure the yield and branching fraction and probably a longitudinal polarization fraction if the contribution would be sizeable. For most of the studies done later, 19 events for the $B^+ \to a_2^+ K^{*0}$ background component are used. For the final fits to data the component is fixed to 0 events and a systematic uncertainty for a possible $B^+ \to a_2^+ K^{*0}$ contribution on the final results is estimated by varying the number of $B^+ \to a_2^+ K^{*0}$ events.

4.4 Analysis Technique

The following section explains the fit technique and the particular set up for the $B^+ \to a_1^+ \ K^{*0}$ decay. Prior to performing the fit, the preliminary event selection discussed above in section 4.2 is applied. The selection criteria are in general quite loose to allow a high signal efficiency and to provide sufficient events in the ΔE and m_{ES} sidebands to allow for a good characterization of the continuum background.

The analysis technique consists of an unbinned multivariate extended maximum likelihood (ML) fit [35], with the extended likelihood function defined as

$$\mathcal{L} = \frac{e^{-\left(\sum_j Y_j\right)}}{N!} \prod_{i=1}^{N} \mathcal{L}_i \ . \tag{4.1}$$

where the first term takes into account a Poisson fluctuation in the total number of events N in the selected sample; Y_j are the numbers of events for each hypothesis component j. The five hypothesis components are signal, a $B \to a_2 K^*$ component, $q\overline{q}$ background, charm $B\overline{B}$ background and charmless $B\overline{B}$ background. Within the likelihood function the likelihood $\mathcal{L}_i$ for each event candidate i is the sum of $Y_j \mathcal{P}_j(\vec{x}_i, \vec{\alpha}_j)$ over all hypotheses j:

$$\mathcal{L}_i = \sum_{j=1} Y_j \mathcal{P}_j(\vec{x}_i, \vec{\alpha}_j) \,. \tag{4.2}$$

Where $\mathcal{P}_j(\vec{x}_i, \vec{\alpha}_j)$ is the product of the probability density functions (PDFs) for hypothesis component j. $\vec{x}_i$ are the measured discriminating variables. The quantities $\vec{\alpha}_j$ represent parameters in the expected distributions of the measured variables for each hypothesis. Each discriminating variable $\vec{x}_i$ in the likelihood function is modeled with a probability density function (PDF), where the parameters $\vec{\alpha}_j$ are extracted from various MC simulation or m_{ES} and ΔE On-Peak sideband data. The observable discriminating variables $\vec{x}_i$ used for all hypothesis components in the fit are: m_{ES}, ΔE, the Fisher discriminant $\mathcal{F}$, the invariant masses of the meson resonance candidates m_{a_1} and $m_{K^{*0}}$ and the helicity angles $\mathcal{H}_{K^*}$ and $\mathcal{H}_{a_1}$. The correlations among the fitted input variables are found to be small on average (cp. correlations matrices for MC and data in appendix C), therefor each $\mathcal{P}_j$ is taken to be the product of the PDFs for the separated variables. Hence this is done for $q\overline{q}$ and $B\overline{B}$ backgrounds regarding the helicity angles, while for the signal and the $B \to a_2 K^*$ component an appropriate joint 2-dimensional partial helicity distribution $\mathcal{P}^{ang}(\mathcal{H}_{K^*}, \mathcal{H}_{a_1})$ is used.

In order to find the most likely solution for the given likelihood function within a dataset, the negative logarithm of the extended likelihood function (NLL) is minimized. At the point in the parameter space for which the fitting routine converges, these parameters are taken as the most likely solution. A single NLL value at the minimum of a fit does not have a meaning on its own, but it is expected for different fits with the same setup to produce a NLL value approximately in the same region. For example with a given setup the result of the NLL value should not be very different if one uses similar datasets of the same size. Also a NLL scan around the minimum will be used later to determine a upper limit.

The implementation of the fitting routine, the following validation, cross check and systematic studies are bases on RooRarFit [45]. For the core fitting RooRarFit uses `Minuit` [46] with the fit sub-routines (`MIGRAD` and `HESSE`) for minimization and error calculation. The package RooRarFit is part of official *BABAR* software releases and the used version is taken from a standard base release. In addition to the standard packages from that base release a couple of packages in a different version are used. For completeness these packages with version tag are given in appendix A in table A.2.

4.4.1 PDF Parameterization

This section gives an overview of the PDF parameterization used for the observable discriminating variables $\vec{x}_i$ in the ML fit.

For the parameterization a combination of the following functions are used: the normal distribution or the Gaussian distribution (G); the Crystal-Ball function (CB), that describes a line shape composed of a central Gaussian with a power law tail to the low end tail and is given by [47]

$$CB(x; a, n, \bar{x}, \sigma) = N \cdot \begin{cases} \exp(-\frac{(x-\bar{x})^2}{2\sigma^2}), & \text{for } \frac{x-\bar{x}}{\sigma} > -a \\ A \cdot (B - \frac{x-\bar{x}}{\sigma})^{-n}, & \text{for } \frac{x-\bar{x}}{\sigma} \leq -a \end{cases}$$

where

$$A = \left(\frac{n}{|a|}\right)^n \cdot \exp\left(-\frac{|a|^2}{2}\right) \text{ and } B = \frac{n}{|a|} - |a| \ .$$

In this formula N is a normalization factor and a, n, $\bar{x}$ and σ are free parameters. The CB function and its first derivative are both continuous; the Breit-Wigners (BW) distribution is given by [48]

$$BW(E; E_0, \Gamma) = \frac{1}{2\pi} \frac{\Gamma}{(E - E_0)^2 + (\Gamma/2)^2}$$

here E_0 is the mass of the resonance and Γ the width of the resonance. The relativistic Breit Wigner (RBW) distribution is given in section 2.6, simple polynomials of different degree n (Pn) and the $ARGUS$ threshold function [49] given by

$$ARGUS(x; \xi) = A\, x\, \sqrt{1 - x^2} \exp\left[-\xi(1 - x^2)\right] \ ,$$

with the argument $x \equiv 2m_{\rm ES}/\sqrt{s}$, a shape parameter ξ and a normalization factor A. The $\sqrt{1 - x^2}$ portion in the ARGUS function describes the available phase space for $m_{\rm ES}$ given a B meson momentum which is flat in the momentum vector 3-dimensional space.

The PDF parameterization for the observable discriminating variables is summarized in table 4.6. The choice of the combined functions for the parameterization of the signal component reflects that the signal includes a small fraction of self-cross-feed (see section 4.2.4). Therefore, no separate component for self-cross-feed in the fit. An additional function has not been used unless it was necessary. The 2-dimensional angular distribution used for the signal and $B \to a_2 K^*$ background component are:

$$\mathcal{P}^{ang*}_{VA}(\mathcal{H}_{K^*}, \mathcal{H}_{a_1}) = \mathcal{P}^{ang}_{VA}(\mathcal{H}_{K^*}, \mathcal{H}_{a_1}) \times \mathcal{G}(\mathcal{H}_{K^*}, \mathcal{H}_{a_1})$$
$$\mathcal{P}^{ang*}_{VT}(\mathcal{H}_{K^*}, \mathcal{H}_{a_1}) = \mathcal{P}^{ang}_{VT}(\mathcal{H}_{K^*}, \mathcal{H}_{a_1}) \times \mathcal{G}(\mathcal{H}_{K^*}, \mathcal{H}_{a_1})$$

where $\mathcal{G}(\mathcal{H}_{K^*}, \mathcal{H}_{a_1})$ is the parameterization of the detector acceptance effects as a function of $\mathcal{H}_{K^*}$ and $\mathcal{H}_{a_1}$. The angular acceptance parameterization is obtained with MC simulation. The acceptance effects are due to kinematic

Table 4.6: *PDF shape summary table for the distribution of the observable discriminating variables ΔE, $m_{\rm ES}$, $\mathcal{F}$, a_1 candidate mass, K^* candidate mass, partial helicity distribution, the helicity $\mathcal{H}_{K^*}$ and helicity $\mathcal{H}_{a_1}$. The shapes are composed of following functional shapes: Gaussian (G), Crystal-Ball (CB), Breit-Wigners (BW), relativistic Breit-Wigners (RBW), nth degree polynomials (Pn) and ARGUS functions. For more details on the function see text.*

Variable	Signal	$B \to a_2 K^*$	Continuum	Charm $B\overline{B}$	Charmless $B\overline{B}$
$m_{\rm ES}$	$CB + G$	CB	$ARGUS$	$ARGUS$	$ARGUS$
ΔE	$CB + G$	$CB + G$	$P2$	$P2$	$P2$
$\mathcal{F}$	$G + G$	G	G	G	G
m_{a_1}	$RBW + RBW$	RBW	$P1$	$P4$	$P3$
m_{K^*}	RBW	RBW	$BW + P1$	$BW + P3$	$BW + P1$
$\mathcal{H}_{K^*}$	$\mathcal{P}^{ang*}_{VA}$	$\mathcal{P}^{ang*}_{VT}$	$G + P2$	$G + P3$	$G + P3$
$\mathcal{H}_{a_1}$			$P6$	$P6$	$P6$

correlations, whereas the detector geometry correlations are negligible. The angles between the final state particles and their parent resonances are related with their momenta; the momenta in the lab frame and the detection efficiency are correlated. Thus acceptance effects in the angular observable $\mathcal{H}_{K^*}$ and $\mathcal{H}_{a_1}$ are expected [6]. The acceptance effects is most evident for $\mathcal{H}_{K^*}$ (cp. figure 4.1) due to the slow pion from the K^* meson decay, but this acceptance effect is compensated by the selection requirement on $\mathcal{H}_{K^*}$ (cp. table 4.2). The ideal angular distribution $\mathcal{P}^{ang}_{VA}(\mathcal{H}_{K^*}, \mathcal{H}_{a_1})$ for the signal component and the distribution for the $B^+ \to a_2^+ K^{*0}$ background component $\mathcal{P}^{ang}_{VT}(\mathcal{H}_{Kstar}, \mathcal{H}_{a_1})$ are given in section 2.4.

The parameters for the PDF distributions, given in table 4.6, for the components are extracted from fits to the longitudinal and transversal polarized signal MC in case for the signal component and to the different background samples, explained in section 4.3, in case for the backgrounds. The input MC sample and the PDFs for the signal component is shown in figure 4.8, for the $B^+ \to a_2^+ K^{*0}$ background component in figure 4.9, for the continuum background component taken from the m_{ES} and ΔE sideband data in figure 4.10, the charmless background component in figure 4.11, and charm background component in figure 4.12.

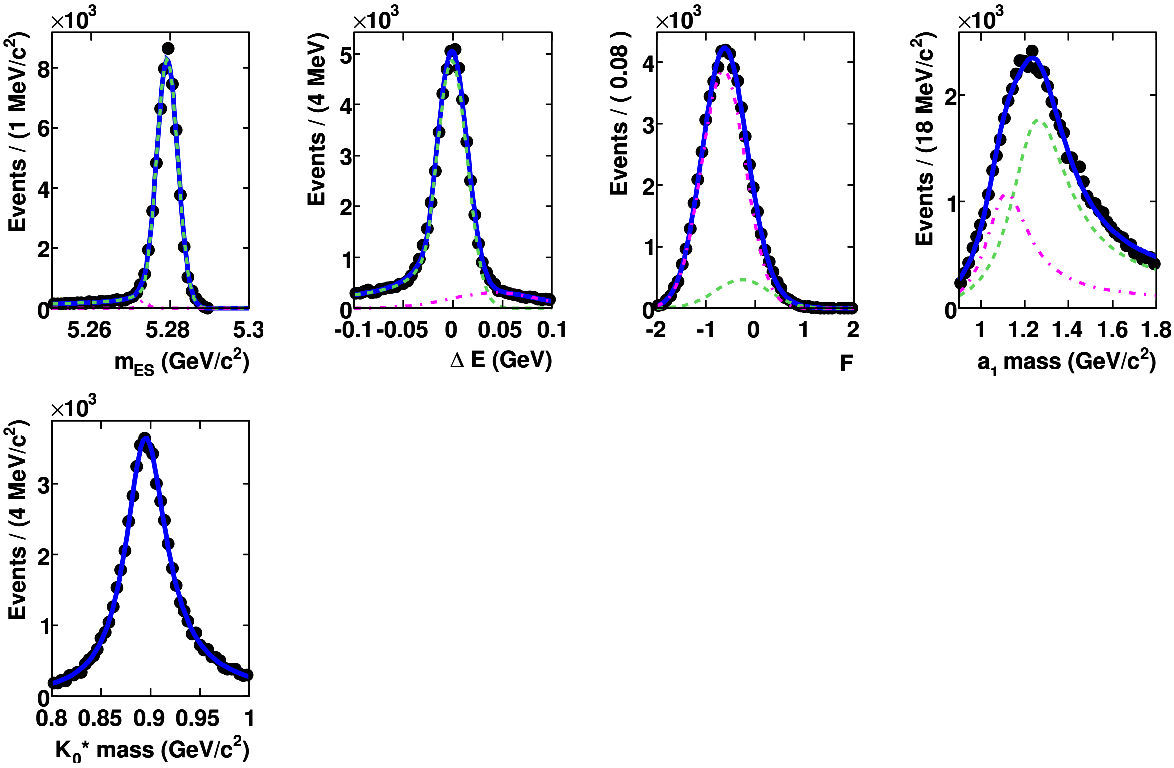

Figure 4.8: *The distributions for the signal MC sample overlaid with the probability density functions for the signal component; shown are the distributions of the observable discriminating variables ΔE, m_{ES}, $\mathcal{F}$, a_1 candidate mass and K^* candidate mass. The points with error bars show the input from the MC sample. The solid blue line is the corresponding PDF. The dashed and dashed-dotted lines are parts of the PDF parameterization, depending on each variable as listed in table 4.6 in section 4.4.1.*

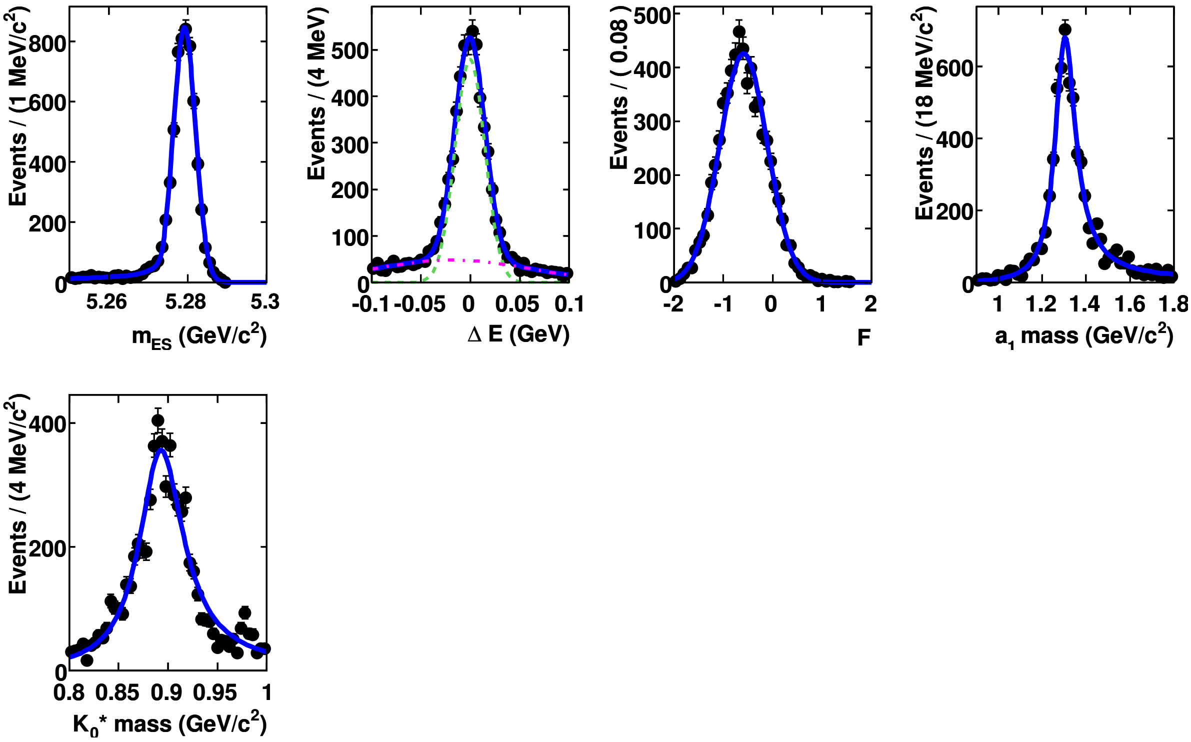

Figure 4.9: *The distributions for the $B \to a_2 K^*$ background MC sample overlaid with the probability density functions for the $B \to a_2 K^*$ component; shown are the distributions of the observable discriminating variables ΔE, m_{ES}, $\mathcal{F}$, a_1 candidate mass and K^* candidate mass. The points with error bars show the input from the MC sample. The solid blue line is the corresponding PDF. The dashed and dashed-dotted lines are parts of the PDF parameterization, depending on each variable as listed in table 4.6 in section 4.4.1.*

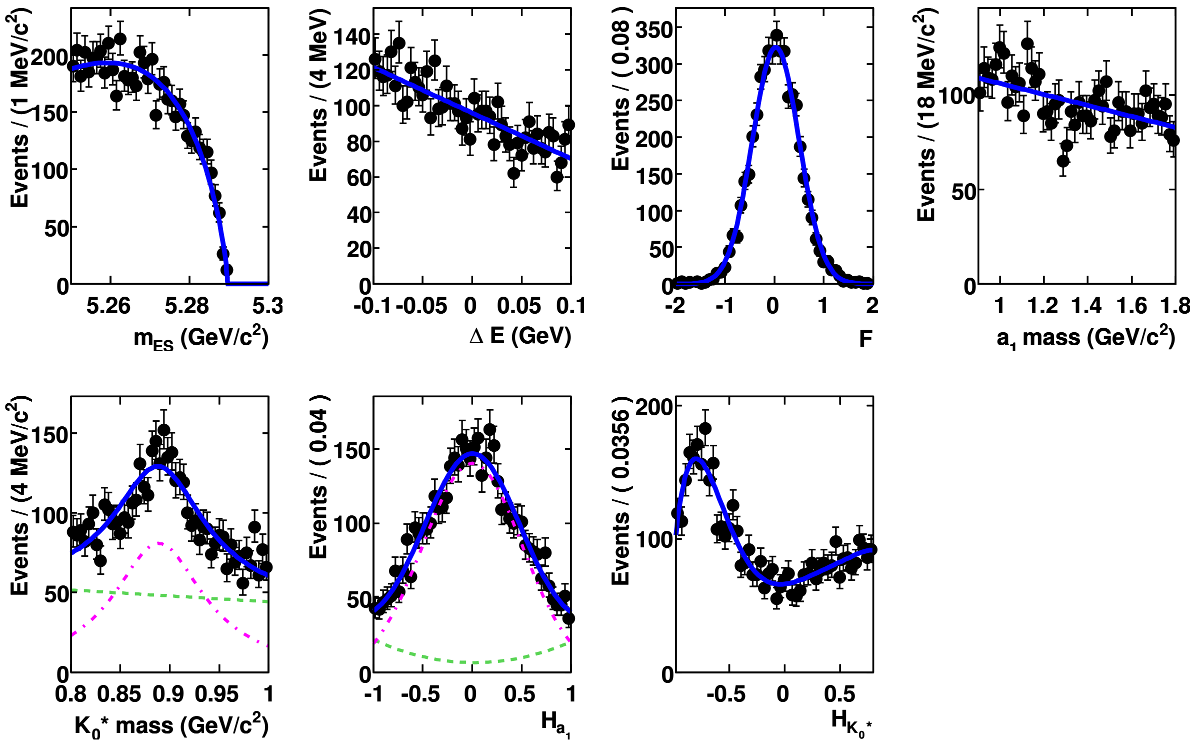

Figure 4.10: *The distributions for the continuum background sample overlaid with the probability density functions for the continuum background component; shown are the distributions of the observable discriminating variables ΔE, m_{ES}, $\mathcal{F}$, a_1 candidate mass, K^* candidate mass, the helicity $\mathcal{H}_{K^*}$ and the helicity $\mathcal{H}_{a_1}$ The points with error bars show the input from the ΔE and m_{ES} sideband data sample. The solid blue line is the corresponding PDF. The dashed and dashed-dotted lines are parts of the PDF parameterization, depending on each variable as listed in table 4.6 in section 4.4.1.*

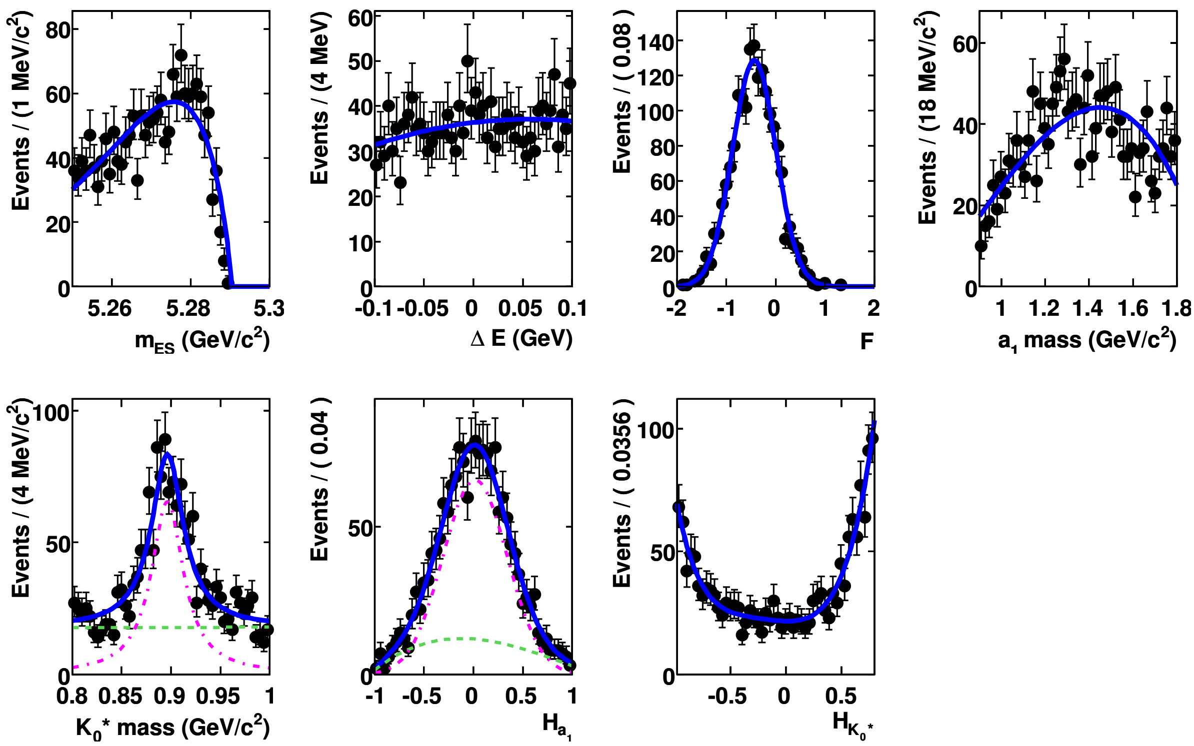

Figure 4.11: *The distributions for the charmless $B\overline{B}$ background sample overlaid with the probability density functions for the charmless $B\overline{B}$ background component; shown are the distributions of the observable discriminating variables ΔE, $m_{\rm ES}$, $\mathcal{F}$, a_1 candidate mass, K^* candidate mass, the helicity $\mathcal{H}_{K^*}$ and the helicity $\mathcal{H}_{a_1}$ The points with error bars show the input from the charmless MC cocktail sample. The solid blue line is the corresponding PDF. The dashed and dashed-dotted lines are parts of the PDF parameterization, depending on each variable as listed in table 4.6 in section 4.4.1.*

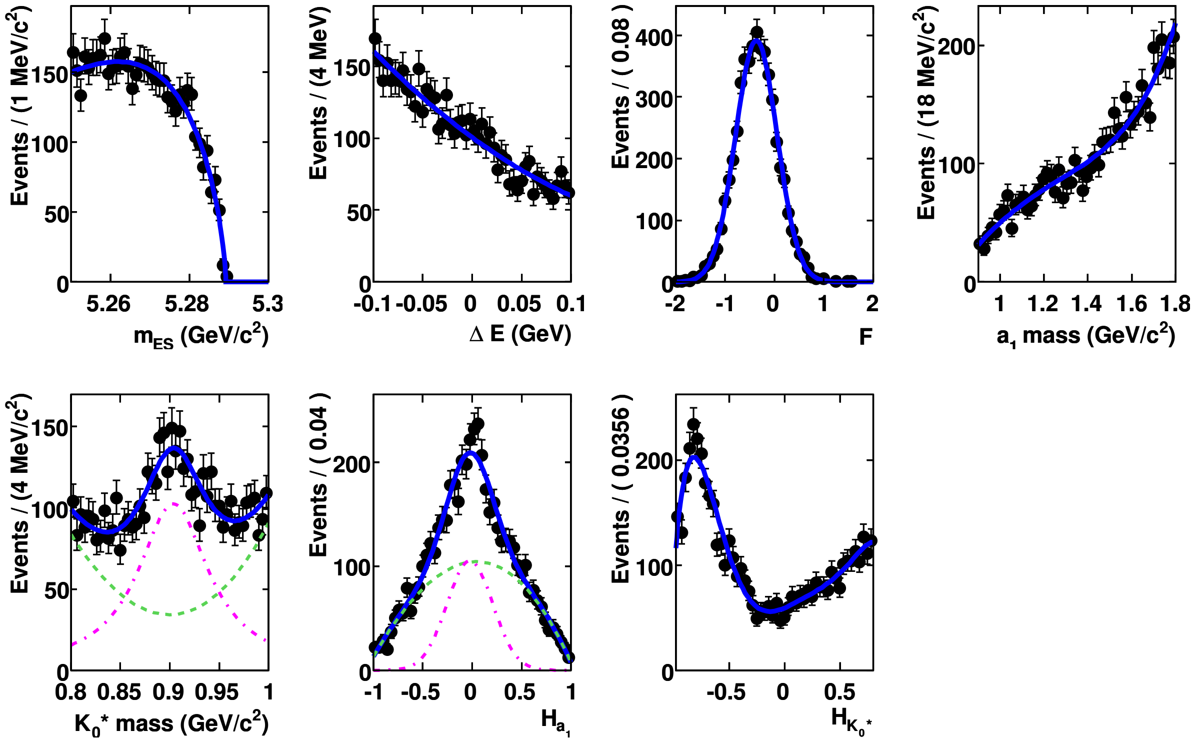

Figure 4.12: *The distributions for the charm $B\overline{B}$ background sample overlaid with the probability density functions for the charm $B\overline{B}$ background component; shown are the distributions of the observable discriminating variables ΔE, m_{ES}, $\mathcal{F}$, a_1 candidate mass, K^* candidate mass, the helicity $\mathcal{H}_{K^*}$ and the helicity $\mathcal{H}_{a_1}$ The points with error bars show the input from the MC sample. The solid blue line is the corresponding PDF. The dashed and dashed-dotted lines are parts of the PDF parameterization, depending on each variable as listed in table 4.6 in section 4.4.1.*

4.4.2 Fixed and Floating Parameters

In summary, the PDF parameterization discussed in the previous section leads to 136 parameter for the maximum likelihood fit, this includes the signal and background yields and the longitudinal polarization fractions. In detail 31 parameter belong to the signal component, 25 to the continuum background component, 19 to the $B^+ \to a_2^+ K^{*0}$ background component, 29 to the charmless background component and 32 to the charm background component. In general is not possible floating all parameters in the maximum likelihood fit, one has to find a set of parameters where the fitting routine converges. Beside this the fit routine has to find a result with in a time that is reasonable in terms of computing resource consumption. This last point is important in the context of repeating the fit routine many times, which is necessary for fit validation, projection plots, cross checks and systematic studies.

For the maximum likelihood fit, the following setup is used: the signal and continuum background yields are floated. The yields for the charm, charmless and $B^+ \to a_2^+ K^{*0}$ background component are fixed. Almost all PDF parameters used in ML fit are fixed, except the longitudinal polarization fraction f_L in the partial helicity distribution for the signal component and four parameters from the continuum background component. These four parameters from the continuum background component are the slope from the ΔE parameterization, one of the parameters from the a_1 meson mass parameterization and two parameters from the K^* candidate mass parameterization. The fixed parameters are kept constant to the values extracted with a fit for the component parameterization to the particular component samples. This setup keeps the ML fit stable and deals with the fit in terms of fitting time. The signal parameters for the a_1 meson mass parameterization would be interesting to measure, but due to the expected limited statistic the a_1 meson parameters are not floated in the fit and thus are not measured in this analysis. All fixed signal parameters in the fit and the fixed background yields will be varied within an appropriate range later and the effect of the variation will be used as a systematic uncertainty. More about this topic will be discussed in section 4.8.

The efforts floating various other parameters for the maximum likelihood fit, especially the yields for charm, charmless and $B^+ \to a_2^+ K^{*0}$ background component are discussed later after the validation techniques, which are necessary for that studies, are introduced.

4.5 Fit Validation

To assess the reliability of the maximum likelihood fitter, the fit is applied to generated toy samples matching the data in size, containing small numbers of signal events, and the expected number of backgrounds events. Applying the maximum likelihood fit to a toy sample is called a toy experiment. The combined results from a number of toy experiments will uncover a potential bias of the fit routine. Two types of toy experiments can be used: one is called pure toy experiments where the toy event samples are generated from PDF shapes, here an arbitrary number of independed samples can be generated. The other type is called embedded toy experiment where the events for at least one component are directly taken from the MC sample, while the events for rest of the components are generated from PDF shape. With embedded toy experiment, one measure how many events for each floated component hypothesis are found and obtain the sizes of potential bias on the fit results.

The following sections give the results for the toy experiments, where it will be shown that the fitting routine works properly. This includes the section 4.5.3 dedicated to studies about floated and fixed PDF parameters and component yields. In addition, a section about the verification of the a_1 meson mass shape from a control sample follows. This studies are necessary since the properties of the a_1 meson are not very well known, as already discussed in section 2.6, but used as a discriminating variable in the ML fit.

4.5.1 Pure Toy Experiments

In order to check the internal consistency of the fit routine toy MC samples are generated directly from the PDFs. The nominal fit routine is then tested with these samples, where the parameters and yields are fixed or floating as mentioned in section 4.4.2. As already mentioned these kind of studies are referred to as pure toy MC experiments. Running the fit routine with these toys data samples will check if the fit converges successfully for all the nominal parameters floating.

The number of expected signal and background events is an important input to these studies, although the number of expected signal events for $B \to a_1 K^*$ is not known. The branching fraction for $B \to a_1 K^*$ is assumed to be $\mathcal{B} = 15 \cdot 10^{-6}$, this value is consistent with the theoretical prediction[5]. With this branching fraction

[5] The value was a educated guess when fit validation was carried out, but none QCD factorization estimation for the branching fraction was available. Since then the value was kept. because it is consistent with the theoretical estimations.

Table 4.7: *Summary of the main results for the three pure toy MC studies for* f_L *0.25, 0.5 and 0.75. For each of the studies 500 toy experiments have been performed. The total number of events in the fits is* 15802. *The numbers of generated events is* 370 *signal events,* 19 $B \to a_2 K^*$ *events,* 1737 *charm events,* 360 *charmless events and 13316 continuum background events. The means and widths given in the table for the number of continuum events, signal events, and* f_L *value are taken from a Gaussian fit to the results of 500 toy experiments each. The full summary tables for the three pure toy studies are given in appendix D.*

f_L	Continuum Fit		Signal Fit		f_L Fit	
	Mean	σ	Mean	σ	Mean	σ
0.25	13307 ± 6	127 ± 4	370 ± 1	32 ± 1	0.247 ± 0.004	0.079 ± 0.003
0.50	13306 ± 6	128 ± 4	370 ± 1	34 ± 1	0.498 ± 0.003	0.069 ± 0.002
0.75	13305 ± 6	125 ± 4	372 ± 1	32 ± 1	0.747 ± 0.003	0.057 ± 0.002

the number of expected signal events is

$$Y_{\text{expected}} = N_B \cdot \mathcal{B} \cdot \prod \mathcal{B}_i \cdot \epsilon = 370$$

where N_B is the number of produced B^+ or B^0 mesons[6], $\mathcal{B}_i$ is the branching fraction for the ith unstable B daughter and ϵ is the mean raw efficiency computed in section 4.2.5. For the $B \to a_2 K^*$, charm, and charmless background components 19, 1737, and 360 events are generated. These event numbers has been determined for the backgrounds in section 4.3. The number of events for the continuum background component is the number of selected events in the data set minus the number of events already generated for the four other components, this gives 13316 events left for the continuum background component.

Pure toy studies are done for three different values for f_L: 0.25, 0.5, and 0.75. Each of these study is done with 500 experiments. The input numbers and results are given in table 4.7. The results in table 4.7 are the mean and width of a Gaussian fitted to the results of the 500 toy experiments for the yield of the continuum background components, the yield of signal component, and

[6]Throughout the analysis its assumed that the branching fractions of the $\Upsilon(4S)$ to B^+B^- and $B^0\overline{B}^0$ are equal, consistent with measurement $f_{+-}/f_{00} = 1.065 \pm 0.026$ with a significance of 2.5 sigma [50].

longitudinal polarization fraction f_L from the signal component.

The minimization results for the 500 toy experiments for the toy studies with $f_L = 0.5$ are given as an example in figure 4.13, where the distribution of the

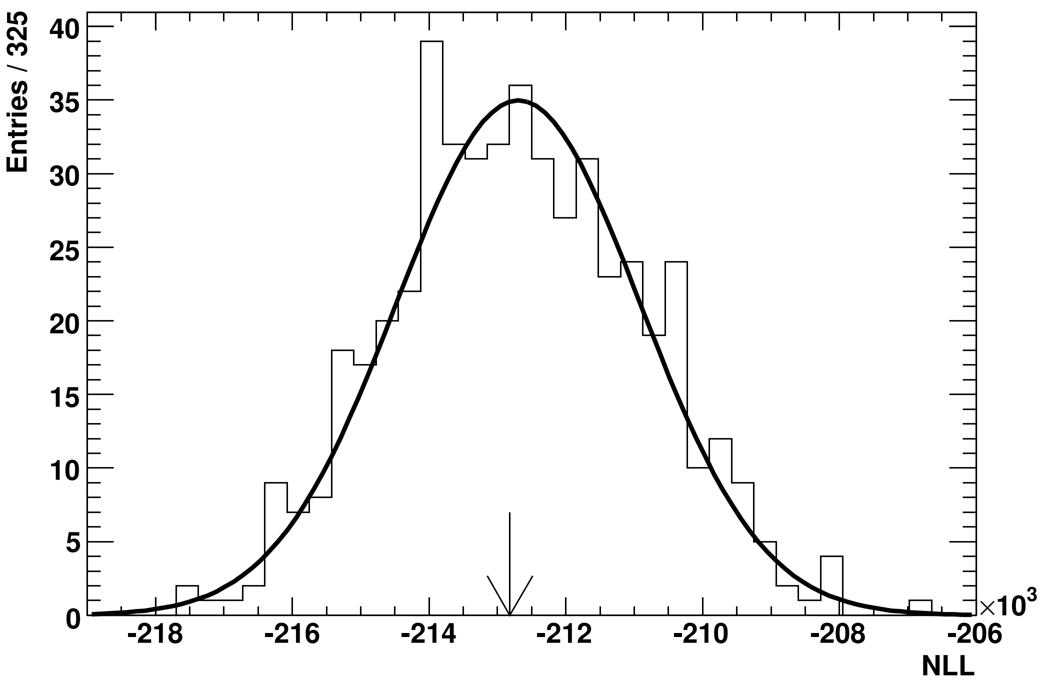

Figure 4.13: *Distribution of the negative-log-likelihood (NLL) from the ML fit for 500 pure toy studies with $f_L = 0.5$. The arrow indicates the NLL value from a ML fit to data, where the results for the yields and parameters were blinded. The solid line is a fit with a Gaussian function to the NLL from the pure toy studies.*

negative-log-likelihood (NLL) from the ML fit is shown. The NLL values from the pure toy experiments are compared to the NLL value from a ML fit to the data (arrow in figure 4.13), where the results for the yields and the parameters were blinded. The mean value for the toy experiment agree well with the NLL value from the nominal ML fit.

The yield distribution for the signal and continuum background as well as the corresponding pull distributions for pure toy studies with generated f_L value of

0.5 are given as an example in figure 4.14. In case of toy experiments the pull p for a parameter or a yield is calculated for each toy experiment as the difference between the observed value p_{obs} and the generated value p_{in} of a parameter or yield divided by the uncertainty of the observed value:

$$p = (p_{\mathrm{obs}} - p_{\mathrm{in}})/\sigma_{p_{\mathrm{obs}}} \; .$$

The signal and continuum yield distribution as well as the corresponding pull distribution are follow the expected Gaussian distribution with a mean around zero and $\sigma \approx 1$.

The fitted longitudinal polarization fraction for the three different toy studies with generated values $f_L = 0.25$, $f_L = 0.50$ and $f_L = 0.75$ are shown in figure 4.15. Here the longitudinal polarization fraction and the corresponding pull distributions show the expected shape of a normal distribution. For all three pure toy studies the mean fitted f_L value is in good agreement with the corresponding generated f_L value.

The summary tables for the three pure toy studies are given in appendix D. There as well the pulls for all floating parameters as the fitted values are summarized.

Finally, it is probably worth to mention that none of the fits in the pure toy experiments was observed to fail and with these studies it is shown that the set up of the fit routine is internally consistent.

4.5.2 Embedded Toys Experiments

In addition to the pure toy experiments so-called embedded toy experiments are discussed for the analysis. Embedded toy experiments are toy experiments where the signal, $B \to a_2 K^*$ background, charm background, and charmless background component events are directly taken from the full MC simulation and are embedded into continuum background events generated from their PDFs. These studies are done mainly to determine the level of fit bias in order to correct the signal yield measured in the data, as well as to determine the systematic uncertainty for the fit. The fit bias is expected, due to the small, but not negligible, residual correlations among the discriminating variables used in the maximum likelihood fit. These correlations are not present in the pure toy experiments, because there the values for the different discriminating variables are generated from the single PDFs independently.

Table 4.8: *Summary of the results for embedded toy MC studies. 500 toy experiments have been done for five different embedded f_L values: 0.0, 0.25, 0.5, 0.75 and 1.0. The total number of events in the experiments are* 15802, *where* 370 *signal events,* 19 $B \to a_2K^*$ *events,* 1737 *charm background events and* 360 *charmless background events are embedded into 13316 continuum background events generated from PDFs. In the table the mean and width of a Gaussian fitted to the results of 500 toy experiments is given for the number of continuum events, signal events and f_L value. In addition the signal bias is shown.*

f_L	Continuum Fit Mean	σ	Signal Fit Mean	σ	Signal Bias	f_L Fit Mean	σ
0.0	13254 ± 6	125 ± 4	429 ± 1	33 ± 1	59 ± 1	0.081 ± 0.003	0.073 ± 0.002
0.25	13262 ± 6	124 ± 4	425 ± 2	33 ± 1	55 ± 2	0.281 ± 0.003	0.067 ± 0.002
0.5	13265 ± 6	124 ± 4	420 ± 2	34 ± 1	50 ± 2	0.489 ± 0.003	0.057 ± 0.002
0.75	13274 ± 5	122 ± 4	411 ± 2	33 ± 1	41 ± 2	0.715 ± 0.002	0.046 ± 0.002
1.0	13284 ± 6	124 ± 4	398 ± 1	31 ± 1	22 ± 1	0.967 ± 0.001	0.033 ± 0.001

For the embedded toy experiments the same number of input events are used as for pure toy experiments in the section above. To be able to input the correct number of longitudinal and transversal polarized signal events, one has to take into account the different efficiencies for longitudinal signal MC ϵ_L and transversal signal MC ϵ_T. Starting from the total number of embedded signal events

$$N_S = N_L + N_T$$

and a given polarization f_L, the number of longitudinal signal events N_L is

$$N_L = N_S \cdot (1 - \frac{1}{1 + \frac{f_L}{1-f_L} \cdot \frac{\epsilon_L}{\epsilon_T}})$$

and the number of transversal signal events N_T is

$$N_T = N_S \cdot (1 - \frac{1}{1 + \frac{1-f_L}{f_L} \cdot \frac{\epsilon_T}{\epsilon_L}})\,.$$

Embedded toy studies have been done for five different values of f_L with 500 toy experiments each. The results are summarized in table 4.8. The signal bias is clearly different from zero for all five studies, but seems to be smaller for lager longitudinal polarization fraction values. Also the mean value for the fitted f_L

Table 4.9: *Summary of the results for two different embedded toy MC studies for* $f_L = 1.0$. *The total number of events in the experiments are* 15802 *where 30 signal events,* 1737 *charm background events and* 360 *charmless background events are embedded into continuum background events generated from PDFs. The number of embedded* $B \to a_2 K^*$ *events is* 19 *events for the one and 0 event for the other toy study. In the table the mean and width of a Gaussian fitted to the results of 500 toy experiments are given for the number of continuum events, signal events and* f_L *value. In addition the signal bias is shown.*

#	Continuum Fit		Signal Fit		Signal	f_L Fit	
$B \to a_2 K^*$	Mean	σ	Mean	σ	Bias	Mean	σ
19	13624 ± 1	22 ± 1	58 ± 1	19 ± 1	28 ± 1	0.92 ± 0.01	0.23 ± 0.01
0	13643 ± 1	23 ± 1	57 ± 1	18 ± 1	27 ± 1	1.11 ± 0.02	0.23 ± 0.01

for each study does not perfectly reproduce the embedded value. In order to have an overview of these results the fitted signal yield and f_L values for the five embedded toy studies are shown in figure 4.16.

The studies show that the signal bias has to be taken into account for final results. Therefore, the procedure of embedded toy experiments are redone after the order of magnitude for the number of signal events and the f_L value in un-blinded data was observed (see section 4.6). This re-evaluation is necessary to determine the exact fit bias and systematic errors. The number of signal events used for this is 30 events, that is the yield extracted from the un-blind ML fit minus a educated guess for a expected bias based on the the yield extracted from the un-blind ML fit. The embedded longitudinal polarization fraction used is $f_L = 1$, inspired by the value found for the un-blind ML fit. The results for two different toy studies are given in table 4.9. Since the number of $B \to a_2 K^*$ background events $n_{B \to a_2 K^*}$ in data is not known two toy studies are done: one where the branching fraction as large as for signal decay and the other where zero events for this component are embedded. For both studies the bias on the signal yield is almost the same. The signal bias from the study with zero $B \to a_2 K^*$ embedded will be used to calculate the signal branching fraction subsequently.

4.5.3 Studies with Floating Charm, Charmless, and $B \to a_2 K^*$ Component Yields

There has been an effort to try to float the charm, charmless and $B \to a_2 K^*$ background component yields for the ML fit. These toy studies are briefly summarized in this subsection.

The similarities in the PDF shapes for charm and charmless background component to the continuum background component, show that the two components are likely to be correlated to continuum background. This is mainly due to the fact that the charm and charmless component are not peaking in the variables m_{ES} and ΔE and show a similar shape in other variables. Most powerful to distinguish between continuum background and charm or charmless background seem to be the Fisher discriminant . In embedded toy experiments where the charm or charmless yield is allowed to float in the fit the result is that some of the continuum events are picked up into the charm or charmless background component yield by the fit. In the studies with floating charm background, done with 500 embedded toy experiments, where 1737 charm background events are embedded, a mean number of 1768 ± 6 charm background events are found with a $\sigma = 132 \pm 4$. In the same setup, where the charmless background component instead of the charm is allowed to float and 360 charmless background events are embedded, a mean number of mean number of 375 ± 4 charmless background events are found with a $\sigma = 89 \pm 3$. This behavior is cross checked with another set of embedded toy experiments where charm (charmless) events haven been embedded but no continuum background events have been generated at all. For these studies all PDF parameters and all yields are fixed, except the continuum and the charm (charmless) yields are allowed to float. These cross checks show the behavior that the continuum events are picked up into the charm (charmless) background component. This studies lead to the result that the charm and charmless background component yield are fixed to the values found in MC samples for the ML fit.

Not surprisingly, the $B \to a_2 K^*$ background component is correlated to the signal component; this is expected since only the a_2 meson mass distribution reconstructed as a a_1 mass and the angular distributions are different compared to the signal component. With a set of toy studies it was confirmed that the fit is not able to fully separate the $B \to a_2 K^*$ background component from signal component. Furthermore the fit could not reliable extract the longitudinal polarization for $B \to a_2 K^*$ component and for most of the toy experiments the PDF parameter ran into an unphysically limit. Therefore, this result supports the idea to fix the yield of the $B \to a_2 K^*$ background component in the final ML fit and float the yield in certain limits to extract a systematic uncertainty.

4.5.4 Embedded Toy Studies with Increased Background Components

A number of embedded toy studies with increased numbers of background events are performed to find out if the fit routine can extract the signal yield with different numbers of background yields. The same setup as before is used and different f_L values are embedded. For studies with the charmless background component, the number of charmless events is increased from 360 to 500. For studies with the charm background component, the number of charm events is increased from 1737 to 2600. And for studies with the $B \to a_2 K^*$ component, the number of $B \to a_2 K^*$ events is increased from 19 to 40. For all studies the charmless, charm, and $B \to a_2 K^*$ background component yields are kept fix. The results can be summarized shortly that the fit is able to extract the signal yield and f_L value in the same way as for the normal embedded toy studies in the case the background is not perfectly estimated. The results for five studies with increased numbers of background events are shown in table 4.10. The extracted signal yields for the different studies are higher than for the normal studies. Therefore it is necessary to take into account a systematic error for the fixed background yields in the fit.

4.5.5 a_1 Meson Shape Studies

The a_1 meson mass shape is not very well known, due to the limited knowledge about the a_1 meson itself. Therefore, this subsection describes a way to verify the a_1 meson mass shape for the ML fit procedure by extracting the a_1 meson mass shape from the decay $B^0 \to D^{*-} a_1^+$, where the D^{*-} is reconstructed in the decay to a D^0 and a π^- meson. This hadronic B decay is chosen because of the relatively large branching fraction of $\mathcal{B}(B^0 \to D^{*-} a_1^+) = 0.0130 \pm 0.0027$ [4] and the possibility of a clean signal selection due to the small mass difference between the D^{*-} meson and the D^0 meson. This procedure is in principle a independent analysis. The way chosen here is a first look into the topic, where favored way would be a full Dalitz-plot analysis.

For the a_1^+ candidates, the selection and the kinematic reconstruction and fitting is done in the same way as described in section 4.2 for the $B \to a_1 K^*$. The D^{*-} candidates are build up from D^0 candidates and a π^- candidate. For the π^- the same list of track is used as in the $B^+ \to a_1^+ K^{*0}$ case. The D^0 candidates

Table 4.10: *Summary of the results for five sets of embedded toy MC studies with increased numbers of background events. 500 toy experiments have been done for each set. The total number of events in each set is* 15802. *The other input values for the each set is: (A)* 370 *signal events,* 19 $B \to a_2K^*$ *events,* 2600 *charm background events,* 360 *charmless background events and* $f_L = 0.5$. *(B)* 370 *signal events,* 19 $B \to a_2K^*$ *events,* 1737 *charm background events,* 500 *charmless background events and* $f_L = 0.5$ *(C)* 370 *signal events,* 19 $B \to a_2K^*$ *events,* 2600 *charm background events,* 360 *charmless background events and* $f_L = 0.75$. *(D)* 370 *signal events, 40* $B \to a_2K^*$ *events,* 1737 *charm background events,* 360 *charmless background events and* $f_L = 0.5$. *(E)* 370 *signal events,* 19 $B \to a_2K^*$ *events,* 2400 *charm background events,* 360 *charmless background events and* $f_L = 0.75$.

#	Continuum Fit		Signal Fit		f_L Fit	
	Mean	σ	Mean	σ	Mean	σ
A	13127 ± 6	125 ± 4	455 ± 2	34 ± 1	0.542 ± 0.002	0.054 ± 0.002
B	13233 ± 6	126 ± 4	431 ± 2	35 ± 1	0.509 ± 0.003	0.057 ± 0.002
C	13134 ± 6	123 ± 4	458 ± 2	34 ± 1	0.746 ± 0.002	0.047 ± 0.002
D	13244 ± 6	124 ± 4	438 ± 2	34 ± 1	0.488 ± 0.003	0.058 ± 0.002
E	13156 ± 6	128 ± 4	445 ± 2	32 ± 1	0.528 ± 0.003	0.057 ± 0.002

are reconstructed in four different decay channels: $D^0 \to K\pi$, $D^0 \to K\pi\pi^0$, $D^0 \to K3\pi$ and $D^0 \to K_s\pi\pi$. The composing of the B^0 meson candidate for the $B^0 \to D^{*-}a_1^+$ decay channel is done with the same decay chain fitting routine as in case of the $B^+ \to a_1^+K^{*0}$ decay chain. Strict requirements on the B^0 candidates in order to have a clean signal selection are used:

$$-0.02 \leq \Delta E \ \leq 0.02\,\mathrm{GeV}$$

and

$$5.27723 \leq m_{\mathrm{ES}} \ \leq 5.28123\,\mathrm{GeV}/c^2 \ .$$

The D meson invariant mass m_D is expected to be

$$1.855 \leq m_D \leq 1.875\,\mathrm{GeV}/c^2 \ .$$

The invariant mass difference between the D meson and the D^* meson, Δm, is very small, thus the emitted π meson has a low momentum. This mass difference is required to be within [51]

$$0.140 \leq \Delta m \leq 0.145\,\mathrm{GeV}/c^2 \ .$$

Beside signal events, possible background events are selected into a different sample for a background subtraction. Therefore, the ΔE and m_{ES} cuts are changed to select ΔE or m_{ES} sideband events. For ΔE events have to be inside one of the two regions $-0.2\,\mathrm{GeV}$ to $-0.11\,\mathrm{GeV}$ or $0.11\,\mathrm{GeV}$ to $0.2\,\mathrm{GeV}$. For the variable m_{ES} the region $5.25\,\mathrm{GeV}/c^2$ to $5.27\,\mathrm{GeV}/c^2$ is selected.

In order to extract an a_1 meson mass shape, a relativistic Breit-Wigner function and a 2nd order polynomial is fitted simultaneously to the a_1 meson mass distribution selected from data, as described above. The parameters for the polynomial are fixed to the values, which haven been obtained by a separate fit to the selected sideband sample beforehand. All other parameters are floated. This fitting procedure including the cuts are tested on large MC samples. Beside the generic $B\overline{B}$ MC dataset, $B^0 \to D^{*-}a_1^+$ signal MC events are used. For these signal MC events the `EvtGen` generator model source code is given in appendix B.

The results from the fit are an a_1 mass of (1.17 ± 0.02) GeV/c^2 and a width of (0.48 ± 0.01) GeV/c^2. The given uncertainties are statistical uncertainties only. The data and fit results for the a_1 invariant mass distribution are shown in figure 4.17. The results for the mean and width of the a_1 meson mass from the $B^0 \to D^{*-}a_1^+$ decay are in reasonable good agreement with values used in the analysis. In order to remove possible uncertainties in the a_1 mass shape, due to other meson contribution, such as the a_2 meson, a full Dalitz-plot analysis is necessary. Throughout the analysis the mean $m_{a_1} = 1230$ MeV/c^2 and the width is $\Gamma = 400$ MeV, given in section 2.6 are used to have consistent values among all BABAR analysis involving an a_1 meson.

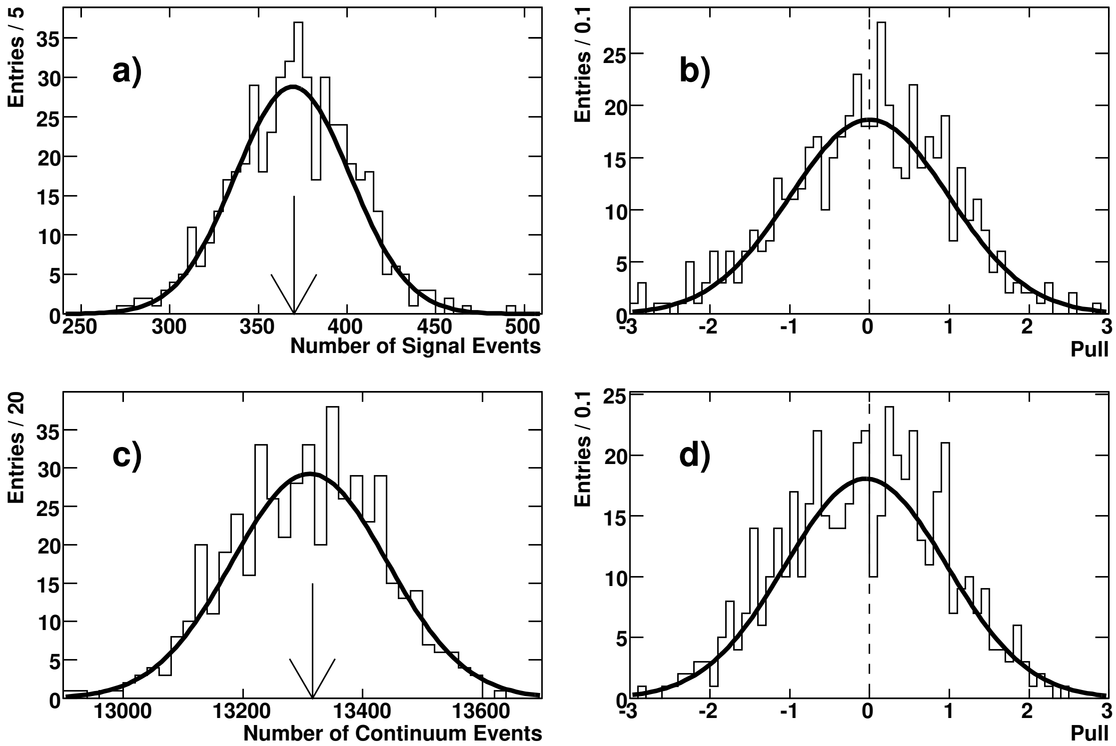

Figure 4.14: *Yield and pull yield distributions for pure toy studies with a generated longitudinal polarization fraction* $f_L = 0.5$*. 500 toy experiments are the bases for the shown distributions. In detail are shown the yield for signal events (a) and the corresponding pull (b) distribution. The arrow indicates that* 370 *signal events have been generated for each toy experiment. The yield (c) for the continuum background component and the corresponding pull distribution (d) are also shown. In sub-figure (c) the arrow indicates that 13316 continuum background events have been generated for each toy experiment. In each sub-figure the solid line is a fit with a Gaussian function to the actual distribution. The summary tables for the three pure toy studies are given in appendix D, where all pulls with corresponding* σ *are summarized.*

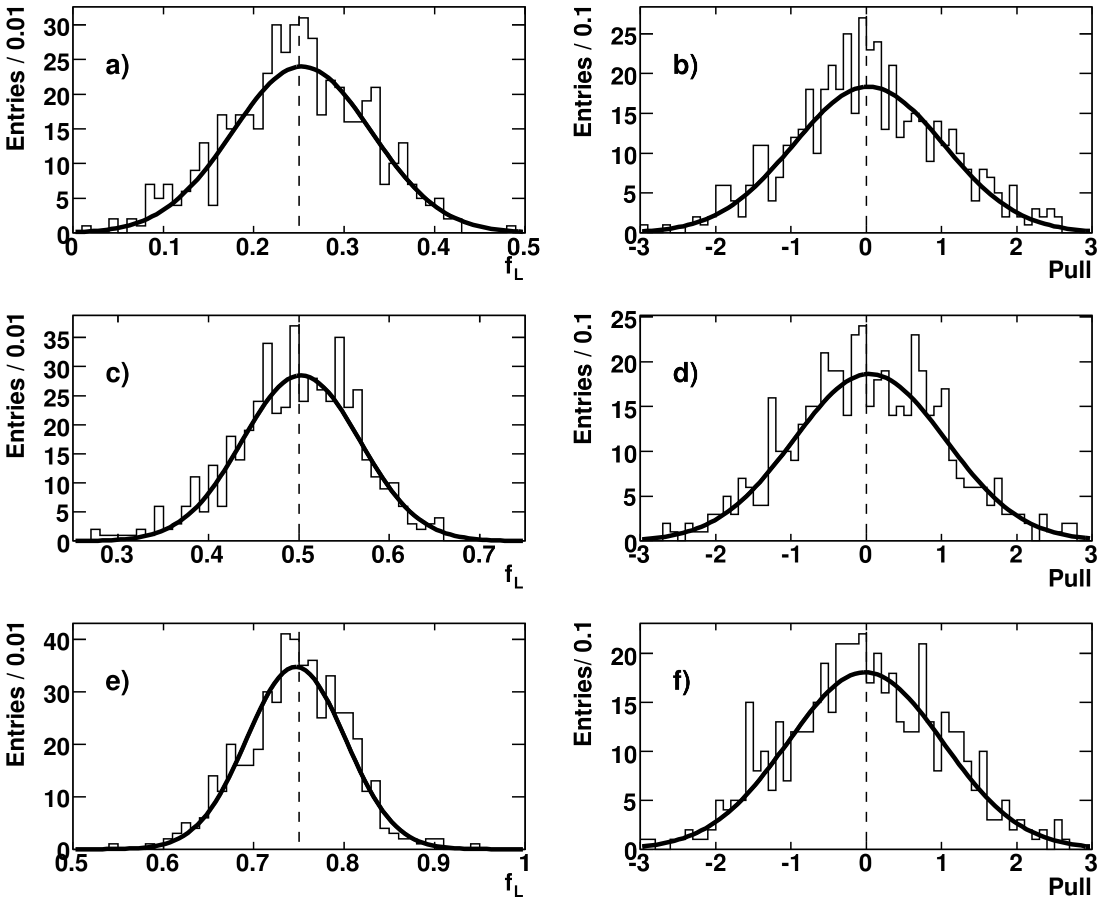

Figure 4.15: *Fitted longitudinal polarization fraction f_L and the corresponding pull distribution for the three pure toy studies. Results shown are based for each of the three toy studies on 500 toy experiments. In detail the shown distributions are fitted f_L value for a generated $f_L = 0.25$ (a) and the corresponding pull distribution (b). Same for a toy experiments with a generated $f_L = 0.5$ in (c) and (d) and for a generated $f_L = 0.75$ shown in sub-figure (e) and (f).*

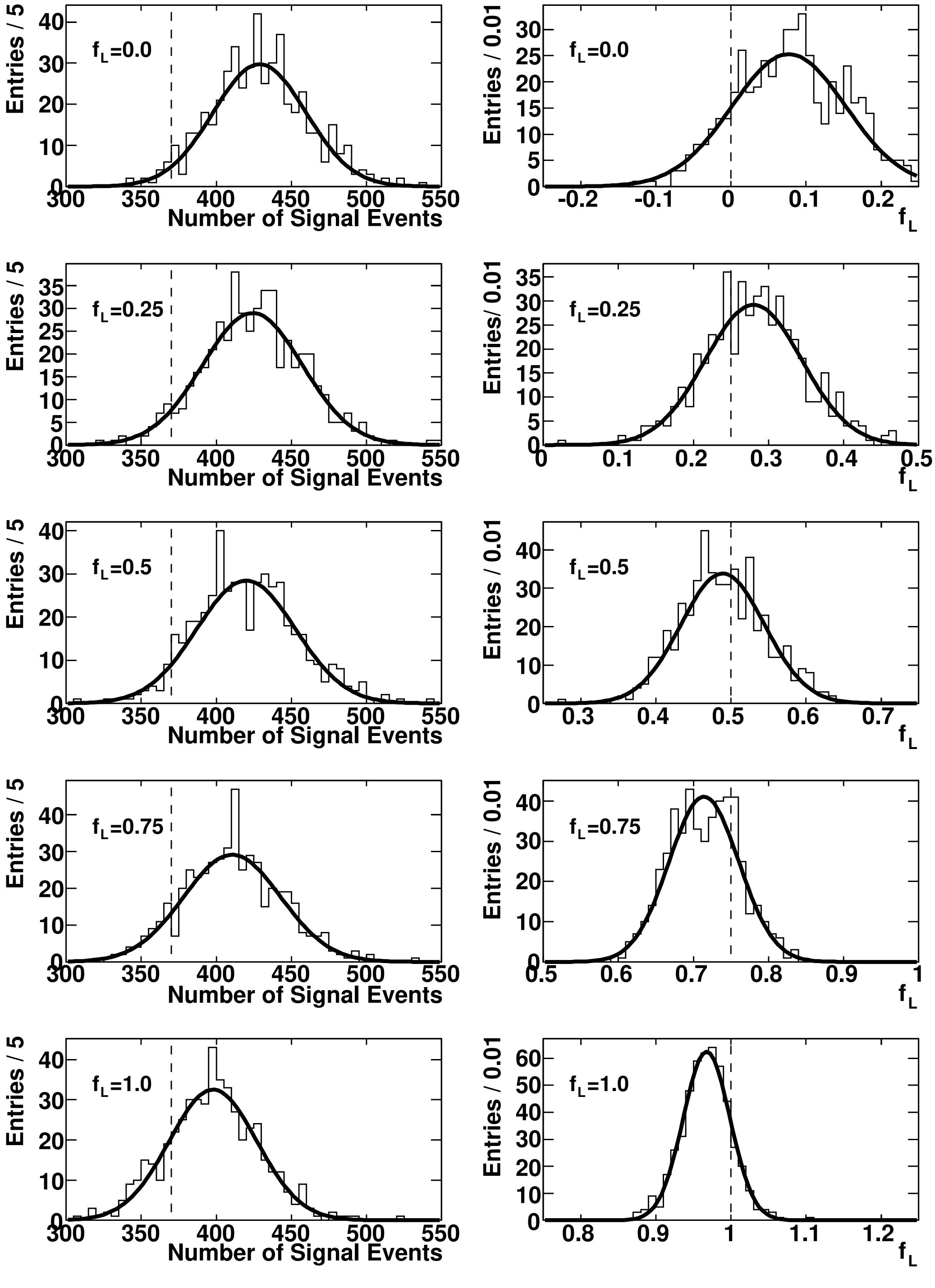

Figure 4.16: *Fitted signal yield and the longitudinal polarization fraction f_L for five embedded toy studies with embedded f_L values (from top to bottom):* 0.0, 0.25, 0.5, 0.75, 1. *The dashed lines indicate the embedded values. Each study is done with 500 toy experiments. For more detail see text.*

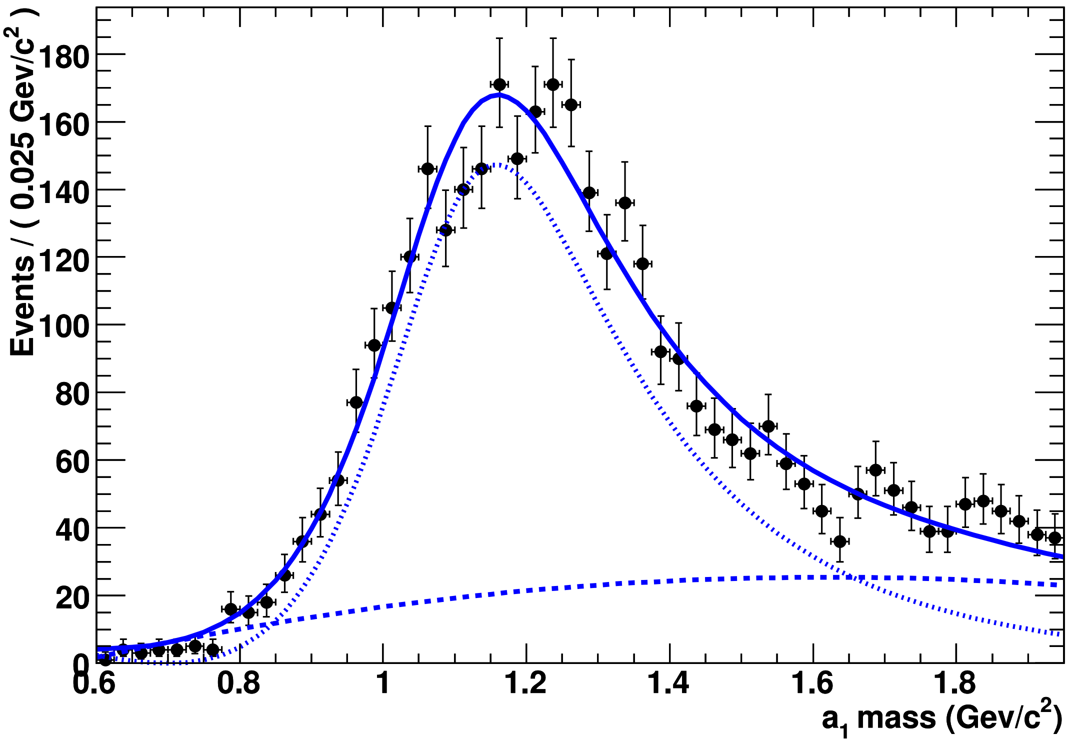

Figure 4.17: a_1 *meson mass distribution in the hadronic decay* $B^0 \rightarrow D^{*-}a_1^+$ *in units of* GeV/c^2. *The points with error bars show the data; the solid line shows signal-plus-background fit; the dotted line is signal and the dashed line is sideband background fit component.*

4.6 Results

Within this section the results for the branching fraction $\mathcal{B}$ for the decay $B^+ \to a_1^+ K^{*0}$ are presented. The branching fraction for the decay is obtained from

$$\mathcal{B} = \frac{Y - Y_b}{\epsilon\, N_B \prod \mathcal{B}_i}\,, \tag{4.3}$$

here $\mathcal{B}$ is the product $\mathcal{B}(B^+ \to a_1^+ K^{*0}) \times \mathcal{B}(a_1^+ \to \pi^+\pi^-\pi^+)$, Y is the yield of signal events from the fit, Y_b is the fit bias taken from table 4.9 in section 4.5.2, ϵ is the raw efficiency as computed from signal Monte Carlo, $\mathcal{B}_i$ is the branching fraction for the $K^{*0} \to K^+\pi^-$ decay $\mathcal{B}(K^{*0} \to K^+\pi^-)$ and is assumed to be 2/3, obtained from isospin formalism with the Clebsch-Gordan coefficients table [4]. The efficiency depends on the measured f_L value

$$\epsilon = f_L \epsilon_L + (1 - f_L)\epsilon_T$$

where ϵ_L and ϵ_T are the raw efficiencies and are given in section 4.2.5. N_B is the number of produced B^+ mesons and is computed with the assumption of equal production rates of charged and neutral B pairs. This assumption is used for all charmless B decay analysis in BABAR and will be done until there is a precise measurement indicating this assumption is not valid [50].

In table 4.11 the results for two fits to data are shown, the first fit is with f_L as floated parameter and the second fit with f_L fixed to 1. The longitudinal polarization fraction is fixed to 1, to keep the fit for the final results out of a unphysical region, where one can not trust the result and the corresponding uncertainty from the fit. For the final results f_L is fixed to 1 to have a most conservative upper limit and f_L is varied later to obtain a systematic uncertainty. The table shows signal yield Y with statistical uncertainties and the fit bias Y_b with a uncertainty including statistical and systematic uncertainties. Systematic uncertainties in detail are discussed in section 4.8.

The statistical significance S and the significance S' which takes into account statistical and systematic uncertainties are estimated by calculating

$$S^{(\prime)} = \sqrt{-2\ln(\mathcal{L}(0)/\mathcal{L}_0)}$$

where $\mathcal{L}(0)$ is the result of the likelihood function for a branching fraction $\mathcal{B} = 0$ and $\mathcal{L}_0$ is the result of the likelihood function at the minimum. This is visualized with the log-likelihood scan (NLL) curve in figure 4.18, where the value $-2\ln(\mathcal{L}/\mathcal{L}_0)$ is scanned within interested parameter space of the branching fraction. The curves are tested to the hypothesis of being a parabolic distribution

Table 4.11: *Summary of results for decay $B^+ \to a_1^+ K^{*0}$. The table include signal yield Y, fit bias Y_b (see section 4.5.2), statistical significance S, significance S' (statistical and systematic uncertainties), branching fraction $\mathcal{B} = \mathcal{B}(B^+ \to a_1^+ K^{*0}) \times \mathcal{B}(a_1^+ \to \pi^+\pi^-\pi^+)$, upper limit UL at 90% confidence level and longitudinal polarization f_L. The given uncertainties on fit yields are statistical only, the uncertainties on the fit bias include the corresponding systematic uncertainties. The branching fraction of $K^{*0} \to K^+\pi^-$ used to obtain the results given in the tables is $\mathcal{B}(K^{*0} \to K^+\pi^-) = \frac{2}{3}$. The first fit to the data is with f_L as floated parameter and the second fit with f_L fixed to 1. (*) The systematic error on the $\mathcal{B}$ for the fit with floated f_L is not estimated and thus the significance S' including statistical and systematic uncertainties for this fit is not calculated. This leads to the limitation that no UL calculation can be done. (**) No errors on f_L are given since the f_L is fixed in this fit.*

Y	Y_b	S	S'	$\mathcal{B}(10^{-6})$	UL (10^{-6})	f_L
55^{+19}_{-17}	27 ± 14	1.8	$-^*$	$0.7^{+0.5}_{-0.4}{}^*$	$-^*$	$1.1 \pm 0.2 \pm 0.1$
57^{+20}_{-17}	27 ± 14	1.8	0.9	$0.7^{+0.5+0.7}_{-0.4-0.7}$	1.6	1.0^{**}

and found that this is in relatively good agreement, but with the restrictions of being slightly asymmetric for the lower part, from this one can conclude that the underlying likelihood distribution follows a normal distribution. The statistical significance is found to be 1.8 for this measurement. When the statistical and the systematic uncertainties are combined the significance is 0.9, due to this an upper limit on the branching fraction is set.

A likelihood scan for the branching fraction, which is in principle the basis for the NLL scan curve, shown in figure 4.18, is used to calculate the upper limit (UL) by integrating over the likelihood curve up to the branching fraction corresponding to a 90% confidence level. For a likelihood scan, the likelihood is calculated with a ML fit with the nominal setup, where the observable, e.g. the branching fraction, is fixed to some value; this is repeated for a number of values chosen to be within the interested parameter space for the scan. For calculating the upper limit, the systematic uncertainty from the $B \to a_2 K^*$ component variation is excluded. This is necessary to estimate a conservative UL, since

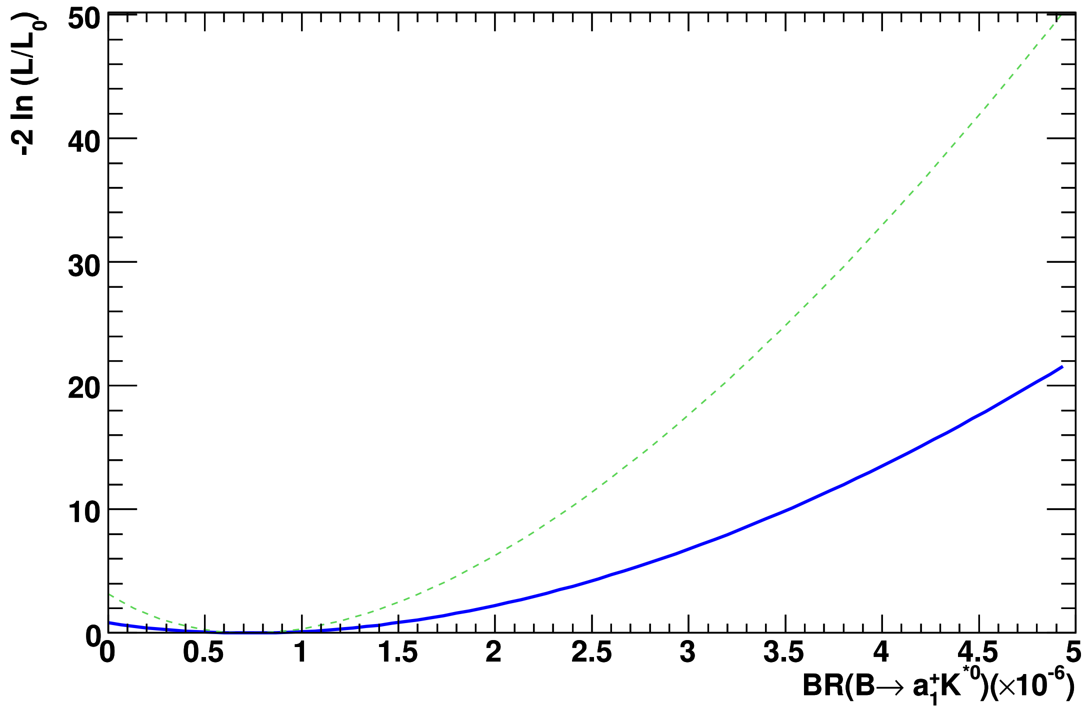

Figure 4.18: *Shown is the log-likelihood scan curves for the decay* $B^+ \to a_1^+ K^{*0}$. *The* blue solid *line represent the curve including statistical and systematic uncertainties and the* green dashed *curve is with statistical error only. Systematic uncertainties in detail are discussed in section 4.8.*

the $B \to a_2 K^*$ is fixed to 0 in the nominal ML fit; a yield for the $B \to a_2 K^*$ component could just brings the central value signal branching fraction down, because it could absorb some signal events.

In table 4.11 the systematic error on the branching fraction for the nominal ML fit with floated f_L is not estimated and thus the significance S' and UL calculation is not done for this case.

To visualize the fit results projection plots for the discriminating variables are created. These are distributions for signal-enhanced subsets of the data projected onto the fit observables for the decay. The signal is enriched by require the ratio

$$R = \mathcal{L}_{\text{sig}} / (\mathcal{L}_{\text{sig}} + \sum \mathcal{L}_{\text{bkg}})$$

Table 4.12: *Summary of the floated parameters. Shown are initial values, final values with upper and lower errors for the nominal ML fit on data. For the ML fit the f_L parameter was floated.*

Floating Parameter	Initial Value	Final Value	Error	
			high	low
ΔE slope continuum	-2.7	-2.5	+0.2	-0.2
m_{a_1} slope continuum	-0.21	-0.32	+0.01	-0.01
m_{K^*} $\sigma_{\rm BW}$ continuum	0.112	0.118	+0.006	-0.005
m_{K^*} slope continuum	-0.45	-0.51	+0.09	-0.07
$Y_{\rm Continuum}$	14101	13778	+126	125
$Y_{\rm Signal}$	370	55	+19	-17
f_L	0.5	1.1	+0.2	-0.2

to be larger between 0.95 and 0.99, depending on the plotted plotted observable and computed without the plotted variable. The requirement on the ratio is optimized for every observable independently. In figure 4.19 the projection plots onto $m_{\rm ES}$, ΔE, $\mathcal{F}$, $a_1$mass, K^* mass, $\mathcal{H}_{a_1}$, and $\mathcal{H}_{K^*}$ of signal-enhanced data samples are shown. For the distributions the different background components are combined into one background contribution. The remaining fraction of signal events after the cut with respect to the nominal fit is 26% for $m_{\rm ES}$, 22% for ΔE, 46% for $\mathcal{F}$, 34% for $m(\rho\pi)$, 21% for $m(K\pi)$, 19% for $\mathcal{H}_{K^*}$ and 35% for $\mathcal{H}_{a_1}$. The variation in the remaining fraction of signal events in the different observable arise from the facts that each plot is computed without the plotted variable and the requirement on the ratio is optimized independently. For the given low number of signal events the fit results agree reasonable well with the data points. Problematic, due to the low number of remaining signal events, seems to be the $m(\rho\pi)$ mass and $\mathcal{H}_{K^*}$ distribution.

For completeness all floated parameters and corresponding initial and final values are given in table 4.12 for the ML with floated f_L and in table 4.13 for the final fit with fixed f_L.

The obtained product of branching fractions is:

$$\mathcal{B}(B^+ \to a_1^+ K^{*0}) \times \mathcal{B}(a_1^+ \to \pi^+\pi^-\pi^+) = (0.7^{+0.5+0.7}_{-0.4-0.7}) \times 10^{-6},$$

corresponding to an upper limit of 1.6×10^{-6}. With the assumption of $\mathcal{B}(a_1^\pm(1260) \to \pi^+\pi^-\pi^\pm)$ is equal to $\mathcal{B}(a_1^\pm(1260) \to \pi^\pm\pi^0\pi^0)$, and that

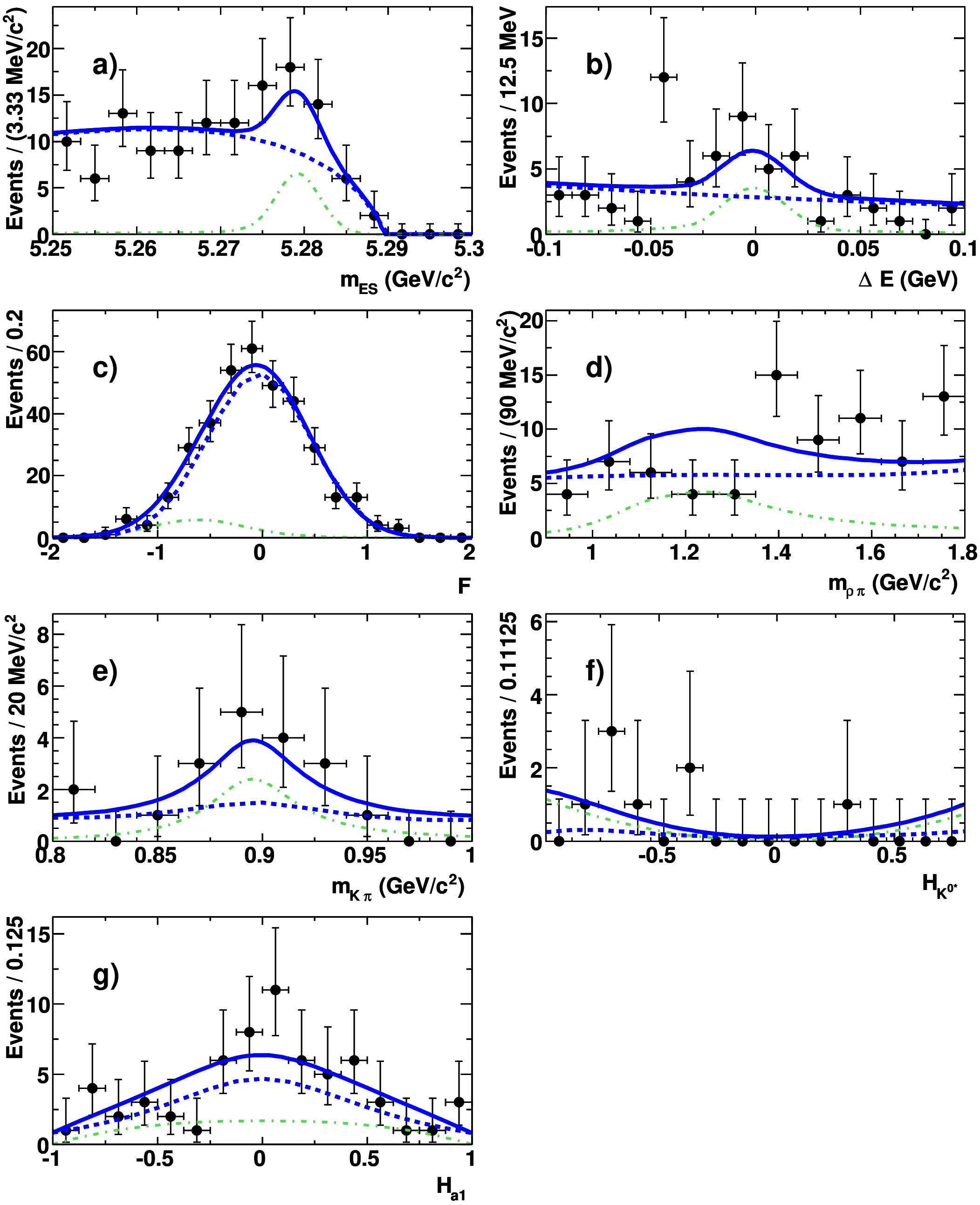

Figure 4.19: *Distributions for signal-enhanced subsets (see text) of the data projected onto the fit observables for the decay $B^+ \to a_1^+ K^{*0}$; (a) $m_{\rm ES}$, (b) ΔE, (c) $\mathcal{F}$, (d) $m(\rho\pi)$ for the a_1 candidate, (e) $m(K\pi)$ for the K^* candidate, (f) $\mathcal{H}_{K^*}$ and (g) $\mathcal{H}_{a_1}$. The solid lines represent the results of the fit, and the dot-dashed and dashed lines the signal and background contributions, respectively. These plots are made with cuts on the ratio of signal to total likelihood. With respect to the nominal fit* 19% *to* 46% *(depending on the variable) of signal events remain.*

Table 4.13: *Summary of the floated parameters. Shown are initial values, final values with upper and lower errors for the nominal ML fit on data. For the ML fit the f_L parameter was fixed to 1.*

Floating Parameter	Initial Value	Final Value	Error	
			high	low
ΔE slope continuum	-2.7	-2.5	+0.2	-0.2
m_{a_1} slope continuum	-0.21	-0.32	+0.01	-0.01
m_{K^*} σ_{BW} continuum	0.112	0.118	+0.006	-0.005
m_{K^*} slope continuum	-0.45	-0.51	+0.10	-0.07
$Y_{\text{Continuum}}$	14101	13776	+126	125
Y_{Signal}	370	57	+20	-17

$\mathcal{B}(a_1^{\pm}(1260) \to 3\pi)$ is equal to 100%, one obtains:

$$\mathcal{B}(B^+ \to a_1^+ K^{*0}) = (1.5^{+1.0+1.4}_{-0.9-1.4}) \times 10^{-6},$$

corresponding to an upper limit of 3.3×10^{-6}. The first error quoted is statistical and the second systematical. Since the signal significance is 0.9 standard deviations, a 90% confidence level upper limit is quoted.

4.7 Cross Checks

Complementary cross checks are performed to be sure to have a reliable fit with the necessary high quality. Three cross checks have been done after extracting the branching fraction and the polarization: firstly, f_L is fixed to different values for the ML fit to the data. Secondly, an alternative method to visualize the discriminating variables is used. And thirdly, a portion of signal MC is embedded into the data set and the ML fit is repeated. The cross checks and the results are discussed in this section.

4.7.1 Fixing and Floating f_L

To understand the influence of f_L on the branching fraction, f_L was fixed to different values for the ML fit on data. As it is intended to derive a conservative upper limit on the branching fraction, the correlation between the branching fraction and f_L values needs to be understood. The expected behavior obtained from the ML fit result on data is that the branching fraction gets larger with f_L near 1. To demonstrate this the results for four fits with the f_L floated and fixed to 1.0, 0.9 and 0.8 are presented in table 4.14. The results shown in table 4.14 confirm the expected behavior of the ML fit on data.

Table 4.14: *The branching fraction dependency on the longitudinal polarization f_L. Results from four ML fits to data with f_L floated and fixed to 1.0, 0.9 and 0.8. The error given for branching fraction is the statistical uncertainty only.*

f_L value	branching fraction
floated	$0.730^{+0.472}_{-0.431}$
1.0	$0.725^{+0.477}_{-0.428}$
0.9	$0.688^{+0.472}_{-0.421}$
0.8	$0.622^{+0.459}_{-0.408}$

4.7.2 *sPlots*

The alternative method to visualize the discriminating variables compared to the projection plots, shown in figure 4.19 in section 4.6 before, is the method of so-called *sPlots* [52]. The idea of the *sPlots* formalism is to provide a convenient way to unfold the overall distribution of a mixed sample of events for a control variable into the sub-distributions of the various species which compose the sample, thereby being essentially a method of background subtraction for presenting a signal distribution. The basic idea is to have a set of variables which can be split into two components. The first component is a set of variables for which the distributions of all the sources of events are known: these variables are the discriminating variable. The second component is a set of variables for which the distributions of some sources of events are either truly unknown or considered as such: these variables are the control variables. Here one wants to assess the validity of the fit, and examining the distributions of control variables. So the control variables are obtained by removing one of the discriminating variables before performing again the maximum Likelihood fit. This removed variable is in terms for *sPlot* a control variable. The expected distribution of the control variable is to be compared to the one extracted from the data sample. How to unfold the signal distribution from the whole data sample and the details of the method of *sPlot* is described in [52, 53]. Compared to projection plots, this method should be statistically more powerful, since all events in the sample contribute to the plot.

The *sPlots* for the $B \to a_1^+ K^{*0}$ decay for all discriminating variables in the ML fit for signal and continuum background are shown in figure 4.20. The *sPlot* method rely on the assumption that the discriminating variables are uncorrelated. To assure that the *sPlot* method works, certain variables, which are likely correlated in the first place, are treated in a special way. If one of the following variables is plotted the other variables from the list are ignored in the ML fit: $m_{\rho\pi}$, $m_{K\pi}$, $\mathcal{H}_{a_1}$ and $\mathcal{H}_{K^*}$. For comparison the data from the *sPlot* are overlaid with a PDF. The PDF used is the PDF built directly for that component (signal or continuum) and that observable (m_{ES}, ΔE, $\mathcal{F}$, $m_{\rho\pi}$, $m_{K\pi}$, $\mathcal{H}_{a_1}$ or $\mathcal{H}_{K^*}$).

The *sPlot* for the $B \to a_1^+ K^{*0}$ decay shows for the a_1 signal component candidate mass m_{a_1} a flat shape, that does not follow the expected shape for a_1 mesons. By mischance for the presentation, the PDF overlaid for m_{ES} in this case is multiplied with a negative yield. The continuum component seems all over well distributed. In general *sPlot* are not expected to look totally perfect in case the signal is not significant. In summary the *sPlots* show the same behavior as the signal-enhanced projection plots.

4.7.3 Embedding Signal MC into Data

To overcome reservations that the low number of signal events in data is due to misbehavior of the fit routine, 200 signal MC events are added randomly into the data sample on which the ML fit is executed. The longitudinal polarization fraction represented by the embedded signal MC events is $f_L = 0.75$. Running the ML fit on this signal enriched data sample a longitudinal polarization fraction of $f_L = 0.75^{+0.07}_{-0.08}$ is extracted. The fit found 249^{+29}_{-28} signal events with a statistical significance of 12.3. The projection plots for the study are shown in figure 4.21. This study has demonstrated the reliability of the fit routine in terms of finding signal events in data and reproduce the embedded longitudinal polarization fraction.

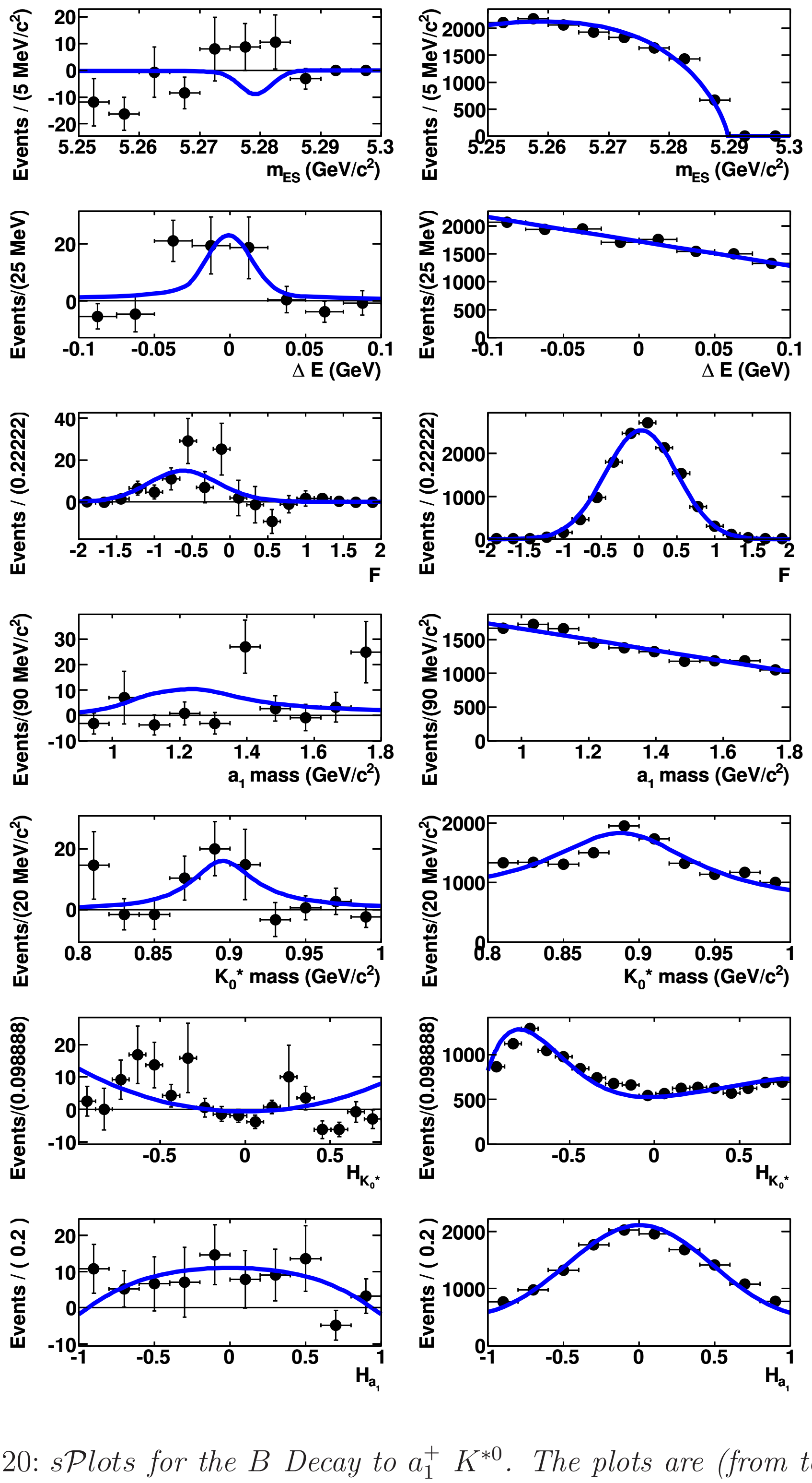

Figure 4.20: *sPlots for the B Decay to* a_1^+ K^{*0}*. The plots are (from top to bottom):* m_{ES}*,* ΔE*,* $\mathcal{F}$*,* $m_{\rho\pi}$*,* $m_{K\pi}$*,* $\mathcal{H}_{K^*}$ *and* $\mathcal{H}_{a_1}$*. The components are signal on the left-hand side and continuum background on the right-hand side. Data points are from the sPlots method and solid line is the PDF from ML fit overlaid.*

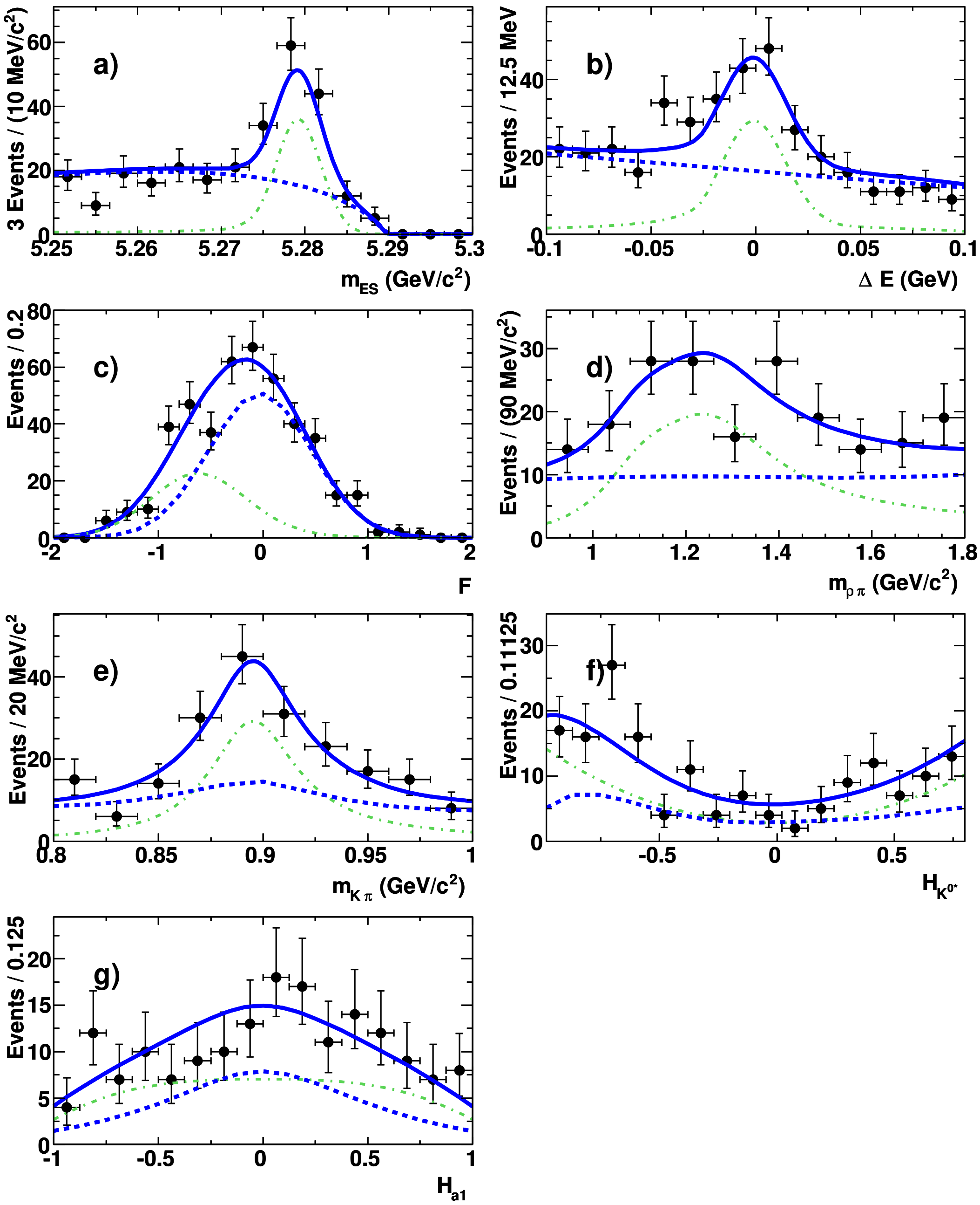

Figure 4.21: *Distributions for signal-enhanced subsets (see text) of the data projected onto the fit observables for the decay $B^+ \to a_1^+ K^{*0}$ where 200 signal MC events with $f_L = 0.75$ have been embedded; (a) $m_{\rm ES}$, (b) ΔE, (c) $\mathcal{F}$, (d) $m(\rho\pi)$ for the a_1 candidate, (e) $m(K\pi)$ for the K^* candidate, (f) $\mathcal{H}_{K^*}$ and (g) $\mathcal{H}_{a_1}$. The solid lines represent the results of the fit and the dashed-dotted and dashed lines the signal and background contributions, respectively. These plots are made with cuts on the ratio of signal to total likelihood.*

4.8 Systematic Uncertainties

The systematic uncertainties on the measured branching fraction come from uncertainties on the variables in equation 4.3 in section 4.6. Within this section the influence of the systematic uncertainties are considered and quantitatively estimated. The systematic uncertainties are summarized in table 4.15.

Table 4.15: *Systematic uncertainties on the branching fraction for the decay $B^+ \to a_1^+ K^{*0}$. In the part with additive uncertainties the uncertainties are given in events while in the part with multiplicative uncertainties the uncertainties are given in percentage. For more details see text.*

Source	
Additive uncertainties (events)	
Charm background	6
Chamless background	12
a_2 background	14
a_1 parametrisation	4
PDF parametrisation	3
f_L variation	2
Fit Bias	14
Total additive (events)	26
Multiplicative uncertainties (%)	
Tracking efficiency	1.2
B counting	1.1
MC statistic (efficiency)	0.6
Simulation a_1 decay	3.3
PID	1.4
Event shape variables	1.0
Total multiplicative (%)	4.1
Total systematic uncertainty [$\mathcal{B}(10^{-6})$]	± 0.7

The uncertainties are divided into additive and multiplicative uncertainties and are tabulated separately. The multiplicative uncertainties are in general uncorrelated and the total multiplicative uncertainty is calculated by adding the uncertainties in quadrature. These uncertainties affecting the efficiency and total number of $B\overline{B}$ events, that are multiplicative with respect to the branching fraction. In contrast, the additive uncertainties are in general correlated and increase or decrease the signal yield. The two types of uncertainties are comparable for modes with substantial yields, but the additive uncertainties dominate when the yields are small, which is the case for this analysis. The final row of the table provides the absolute total systematic uncertainty in the branching fraction.

The different sources are discussed in detail in the following beginning with the multiplicative uncertainties:

- Luminosity, B counting: The number of B meson in the data sample is not known perfectly. The relative systematic uncertainty on the B counting for the Run1 to Run6 integrated luminosity of $423.5\,\mathrm{fb}^{-1}$ collected at the $\Upsilon(4S)$ resonance, that corresponds to a production of (465.0 ± 5.1) million $B\overline{B}$ pairs, is found to be 1.1%.

- Tracking efficiency: In principle the simulation uses the same algorithms that are used in reconstruction for the data. Variations between data and simulation can occur because of incomplete or inaccurate description of the interaction of particles with detector material, noise in the detector components or readout electronics. Such effects have an influence on the reconstruction efficiency and particle identification. The systematic uncertainty due to differences in tracking efficiencies between data and simulation is 0.236% per track, added linearly [54]. This results in a tracking efficiency systematic uncertainty of 1.2%.

- PID: Reasons for systematic uncertainties due to particle identification have been given in the item above. Variations between data and simulation in PID have been balanced out for this analysis by PID weights in simulation. The systematic uncertainty on PID is estimated as the difference in the results when using and when not using PID weights in simulation. This leads to a systematic uncertainty of 1.4%.

- MC statistics (efficiency): The size of the MC sample is finite and thus the efficiency based on this sample does have a systematic uncertainty. The uncertainty is the square root of the number of selected events divided by the number of selected events. The selected number of events in the longitudinal polarized signal sample is used to calculate the uncertainty to 0.6%, since the fit results tends to prefer a longitudinal polarization fraction near 1. Anyhow the difference for the uncertainty between both modes is very small. Using the number of selected events in the transversal polarized signal sample leads to a uncertainty of 0.5%.

- Simulation of the a_1 decay: Throughout the analysis, the a_1 decay is simulated as the decay to $\rho\pi$ only. It is necessary to take into account a systematic uncertainty for the a_1 decays through $f^0(600)\pi$ as well. For the uncertainty estimation it is assumed that about 20% of a_1 decays proceeds through $f^0(600)\pi$, which is considered as a conservative estimation [55]. This a_1 meson decay is simulated as a decay into three pions accordingly to the phase space[7]. The difference in the reconstruction efficiency with this simulation model compared to signal decay is used as basis for the uncertainty. The systematic effect is estimated to be 3.3%. Similar procedures are used in other BABAR analyses [19, 56].

- Event shape variables: The event shape variables used in the analysis to separate signal events from continuum events, that make up the biggest fraction of background, are a source for a systematic uncertainty and is therefore estimated. At two places in the analysis event shape variables are used: $\cos\theta_{\mathrm{T}}$ and $\mathcal{F}$ (see table 4.2 in section 4.2). In the case of the Fisher discriminate $\mathcal{F}$, the systematic uncertainty is included in the systematic uncertainty for the PDF parameterization and is discussed below. In the case of the $\cos\theta_{\mathrm{T}}$ variable and the cut on this variable, the systematic uncertainty is estimated from a special control sample study [57]. Following the recommendations from these studies, the systematic uncertainty due to the usage of $\cos\theta_{\mathrm{T}}$ is 1.0 %.

In total, by adding the uncertainties in quadrature, the multiplicative uncertainties is 4.1%.

The dominating additive uncertainties relevant for the analysis are in details:

- ML fit bias: The systematic uncertainty for the ML fit bias is based on the measured fit bias with the embedded toy experiments in section 4.5. The systematic uncertainty is one-half the fit bias added in quadrature with the uncertainty in the fit bias. Here it is found to be 14 events on the signal yield.

- PDF parameterization: The chosen parameterization is a source of a systematic uncertainty and is estimated by varying all nominal fixed signal PDF parameters in the fit to data. The range in that the PDF parameters are varied depends on the information available. The resonance parameters (width and mean) for the K^* (the a_1 parameterization is discussed in a separated item) are varied within the nominal uncertainty [4]. Concerning

[7]The standard phase space model (`PHSP`) in `EvtGen` is used.

the Fisher discriminate $\mathcal{F}$, the range is estimated from *BABAR* internal recommendations for charmless decays[57]. The ΔE mean value is varied by ± 2 MeV and the m_{ES} mean value by ± 0.3 MeV given by the resolution for the variables. All other signal PDF parameters are varied in the range of the uncertainties taken from the PDF modeling stage. The systematic uncertainty is found to be 3 events on the signal yield, where the uncertainty on the a_1 parameterization is not included. That uncertainty is presented separately in the following item.

- a_1 parameterization: For a systematic uncertainty on the a_1 parameterization, the a_1 width is varied by 60 MeV and the mean by 20 MeV within the signal component parameterization. These values are the errors found in the *BABAR* $B^0 \to a_1^+\pi^-$ analysis where the a_1 meson mass parameters have been extracted from a fit to data [19]. The systematic uncertainty is found to be 4 events on the signal yield.

- Longitudinal polarization fraction f_L: A systematic uncertainty coming from fixing $f_L = 1$ in the nominal ML fit is estimated by varying the f_L from 1 to 0.8. The lower limit is concluded from the error on f_L where f_L was floated in the fit to data. The systematic uncertainty is found to be 2 events on the signal yield.

- Background yields: The different background components in the analysis are not perfectly known, therefore it is necessary to take this into account for the final results. The charm, charmless, and $B^+ \to a_2^+K^{*0}$ background components are fixed in the ML fit to the yields extracted from simulation. These yields are varied and the changes in the result for the signal yield are extracted. The range for the charm background component is estimated from the errors on $b \to c$ branching fractions, these errors are about 20% and thus the charm background component yield is varied by $\pm 20\%$. In case of the charmless background cocktail, many of the branching fraction used are unknown and only estimations can be used. In addition, it is likely that a decay is not included in the cocktail at all. In this case the yield is varied by $\pm 100\%$ to be conservative. The branching fraction for the $B^+ \to a_2^+K^{*0}$ decay is unknown and due to the small signal yield the $B^+ \to a_2^+K^{*0}$ background component was fixed to 0. For the estimation of the systematic uncertainty the yield for this component is varied from 0 to 19 events, where the 19 events correspond to a branching fraction of the same size as what was found for the central branching fraction value for the signal decay. The systematic uncertainty split up into the different components is 6 events for charm background component, 12 events for the charmless background component and 14 events for the $B^+ \to a_2^+ K^{*0}$ background component on the signal yield.

To estimate the total additive systematic uncertainty, the correlations between the different individual uncertainties have to be known. To take the correlations into account the parameters and yields discussed in the items above are varied simultaneously. From this the additive systematic uncertainty is found to be 26 events on the signal yield.

The multiplicative and additive uncertainties are then combined and propagated to the branching fraction result. The total systematic uncertainty on the branching fraction is found to be $\pm 0.7 \times 10^{-6}$, for which the additive uncertainty is dominating.

5 Conclusions

The most amazing progress in particle physics in the last three decades is the construction and the verification of the standard model of elementary particles. The success of the standard model in describing a wide variety of experimental data in the energy range $\mathcal{O}(0.1)$ - $\mathcal{O}(100)$ GeV is impressive. On the other hand, experimental evidence like neutrino oscillations and the presence of dark matter cannot find place in the standard model picture. Moreover, masses and mixing of quarks and leptons, which show a significant hierarchy pattern unexplained from first principles, enter in the standard model as free parameters to be determined experimentally. What is beyond the standard model must be able to explain and justify these features as well.

Soon LHC at CERN will open the doors of an unexplored energy frontier. However, the complementarity of high-precision measurements, which can probe energy scales in virtual loops are important. The study of flavour physics not only could provide hints of the scale of new physics before or in concurrence with LHC, but, more important, it will become crucial once the Higgs bosons and/or supersymmetric particles are discovered, in order to interpret these signal in terms of the underlying theory.

In the flavour sector, some of the most important probes for new physics effects are rare decays. A hadronic rare decay as $B^+ \to a_1^+\ K^{*0}$ is particularly appealing, as the contribution from new physics could be competitive with the standard model amplitude. In this work, the procedure and the result of the experimental search for the decay $B^\pm \to a_1^\pm K^{*0}$ have been presented. The search employs a maximum likelihood fit technique with different discriminating variables to distinguish the signal from different background components. The search is based on data collected with the *BABAR* detector at the Stanford Linear Accelerator Center and represents 465 million $B\overline{B}$ pairs produced in e^+e^- annihilation at the $\Upsilon(4S)$ energy. The result for the branching fraction found is:

$$\mathcal{B}(B^+ \to a_1^+ K^{*0}) \times \mathcal{B}(a_1^+ \to \pi^+\pi^-\pi^+) = (0.7^{+0.5+0.7}_{-0.4-0.7}) \times 10^{-6},$$

corresponding to an upper limit at 90% confidence level of 1.6×10^{-6}. With the assumption of $\mathcal{B}(a_1^\pm(1260) \to \pi^+\pi^-\pi^\pm)$ is equal to $\mathcal{B}(a_1^\pm(1260) \to \pi^\pm\pi^0\pi^0)$, and that $\mathcal{B}(a_1^{\pm}(1260) \to 3\pi)$ is equal to 100%, this leads to:

$$\mathcal{B}(B^+ \to a_1^+ K^{*0}) = (1.5^{+1.0+1.4}_{-0.9-1.4}) \times 10^{-6},$$

corresponding to an upper limit of 3.3×10^{-6}. The first error quoted is statistical, the second systematic. The upper limit was estimated by integrating over a likelihood scan curve for the branching fraction around the likelihood minimum. The signal significance was found to be 0.9 standard deviations, the signal significance when only using the statistical uncertainty is 1.8. Improving the method and reducing the systematic uncertainty will not lead to a significant result for the branching fraction and a polarization measurement.

Finally, the results are compared to the QCD factorization estimations discussed in chapter 2. The branching fraction estimation for $B^+ \to a_1^+ K^{*0}$ according to Calderon et al. 0.51×10^{-6} [12] is in good agreement with the upper limit. The expected branching fraction according to Cheng et al is $9.7^{+4.9+32.9}_{-3.5-2.4} \times 10^{-6}$ with a prediction for the longitudinal polarization fraction $f_L = 0.38^{+0.51}_{-0.40}$ [16]. The branching fraction from the analysis is lower than this estimation though not inconsistent with it. The newest prediction for $B^+ \to a_1^+ K^{*0}$ according to Yang, where especially the focus is on the penguin-annihilation amplitude contribution are for the branching fraction $11.2^{+6.1+31.9}_{-4.4-9.0} \times 10^{-6}$ with penguin annihilation turned on and $4.1^{+2.0+1.7}_{-1.6-0.1} \times 10^{-6}$ without penguin annihilation amplitudes. The corresponding longitudinal polarization fraction is $f_L = 0.37^{+0.48}_{-0.37}$ and $f_L = 0.62^{+0.13}_{-0.34}$, respectively [17]. Here both predictions are not inconsistent with the results from the analysis. Although the estimation with penguin annihilation turned on has a higher central branching ratio value it is still in agreement due to the large errors. A clear statement on the longitudinal polarization fraction is not possible since the measurement is not significant, but it seems that a larger value near 1 is preferred. In summary, the result for the upper limit compared to different QCD factorization estimations are found to be in agreement. No hints for new physics have been found; new physics contribution in particular for this decay can be introduced due to the $b \to s$ loop transition, where new heavy non-SM particles can contribute via loop diagrams and increase the branching fraction. But the QCD calculations will profit from these kinds of measurements since they are sensitive to higher order contributions like penguin annihilation or final-state interaction rescattering. No strong statement on the longitudinal polarization fraction for this $B \to AV$ decay is done, since the measurement is not significant.

In context with other measurements for $B \to AV$ decays the results in this field are interesting since no uniform understanding seems to be availably. On the one hand the first measurement of polarization in a vectoraxial-vector B

meson decay indicates a large fraction of a transverse amplitude: for the decay $B^{\pm} \rightarrow \phi K_1(1270)^{\pm}$ a branching fraction of $6.1 \pm 1.6 \pm 1.1 \times 10^{-6}$ with a $f_L = 0.46^{+0.12+0.06}_{-0.13-0.07}$ was found [58]. And on the other hand for the decay $B^0 \rightarrow \rho^+ b_1^-$ only a upper limit of 1.7×10^{-6} could be set [59]. While in the latter decay the expected branching fraction according to Cheng et al is $32^{+16.5+12.1}_{-14.7-4.7} \times 10^{-6}$ with a prediction for the longitudinal polarization fraction $f_L = 0.96^{+0.01}_{-0.02}$ [16].

A Software

This appendix summarizes the used *BABAR* core software packages for this analysis. Table A.1 lists the used extra tags within the release Analysis-42 (22.3.0) for the reconstruction step. Table A.2 lists the extra tags within release Analysis-40 (22.0.4), that are used for the maximum likelihood fit and all associated procedures.

Table A.1: *List of additional used packages (extra tags) for reconstruction in base release Analysis-42 (22.3.0).*

BTaggingTools	V00-05-03
BetaPid	V00-06-06
BetaPidCalib	V00-09-09
BtaTupleMaker	V00-03-13
CrnBeta	V00-07-01
FilterTools	V00-20-18
NetTagger	V00-04-03
PhysMonSequences	V00-02-19
PidDchSvtDrcCalib	V00-04-02
PidTools	V01-05-04
workdir	V00-04-21

Table A.2: *List of used packages and version for fitting procedure and toy studies in base release Analysis-40 (22.0.4).*

RooFitCore	V02-00-09-03
RooFitModels	V02-00-09
RooRarFit	V00-01-72
workdir	V00-04-21

B EvtGen models

B.1 $B^0 \to D^{*+} a_1^+$ EvtGen model

The source code listed in the following is used to generate $B^0 \to D^{*-} a_1^+$ MC decays with the EvtGen MC generator. This is done to verify the a_1 meson mass shape for the $B^+ \to a_1^+ K^{*0}$ analysis. More information on the the different decay models used is given in the EvtGen documentation[28].

```
Alias MyB0         B0
Alias Myanti-B0    anti-B0
Alias MyD*-        D*-
Alias MyD*+        D*+
Alias MyD0         D0
Alias Myanti-D0    anti-D0
Alias Mya_1+       a_1+
Alias Mya_1-       a_1-
Alias Myrho0 rho0
#
Decay Upsilon(4S)
0.500 anti-B0 MyB0  VSS_BMIX dm;
0.500 B0 Myanti-B0  VSS_BMIX dm;
Enddecay
#
Decay MyB0
1.000 MyD*- Mya_1+  SVV_HELAMP 0.336 0.0 0.88 0.0 0.336 0.0;
Enddecay
#
Decay Myanti-B0
1.000 MyD*+ Mya_1-  SVV_HELAMP 0.336 0.0 0.88 0.0 0.336 0.0;
Enddecay
#
# 67 %
Decay MyD*-
1.000 Myanti-D0 pi- VSS;
Enddecay
```

```
#
Decay MyD*+
1.000 MyD0 pi+      VSS;
Enddecay
#
#  PHSP - Phase Space model
Decay MyD0
1.000 K- pi+        PHSP;
Enddecay
#
Decay Myanti-D0
1.000 K+ pi-        PHSP;
Enddecay
#
Decay Mya_1+
1.0000 rho0 pi+     VVS_PWAVE 1.0 0.0 0.0 0.0 0.0 0.0;
Enddecay
#
Decay Mya_1-
1.0000 rho0 pi-     VVS_PWAVE 1.0 0.0 0.0 0.0 0.0 0.0;
Enddecay
#
End
```

B.2 Longitudinal polarized $B \to a_2^+ K^{*0}$ decay

In order to generate a MC sample for the $B \to a_2 K^*$ background component for the $B^+ \to a_1^+ K^{*0}$ analysis decay models for the longitudinal and transversal polarized $B \to a_2 K^*$ decay are needed. More information on the the used decay models is given in the `EvtGen` documentation[28]. The following `EvtGen` source code listing is used for the longitudinal polarized $B \to a_2^+ K^{*0}$ decay.

```
Alias MyB+ B+
Alias MyB- B-
Alias MyKstar0 K*0
Alias MyantiKstar0 anti-K*0
Alias mya_2+ a_2+
Alias mya_2- a_2-
ChargeConj mya_2+ mya_2-
#
Decay Upsilon(4S)
```

```
0.5000 MyB+ B-              VSS;
0.5000 MyB- B+              VSS;
Enddecay
#
Decay MyB+
1.0000 mya_2+ MyKstar0      HELAMP 0.0 0.0 1.0 0.0 0.0 0.0;
Enddecay
#
Decay MyB-
1.0000 mya_2- MyantiKstar0  HELAMP 0.0 0.0 1.0 0.0 0.0 0.0;
Enddecay
#
Decay mya_2+
1.0000   rho0 pi+           TVS_PWAVE 0.0 0.0 1.0 0.0 0.0 0.0;
Enddecay
#
Decay mya_2-
1.0000   rho0 pi-           TVS_PWAVE 0.0 0.0 1.0 0.0 0.0 0.0;
Enddecay
#
Decay MyKstar0
1.000 K+   pi-             VSS;
Enddecay
#
Decay MyantiKstar0
1.000 K-   pi+             VSS;
Enddecay
#
End
```

B.3 Transversal polarized $B \to a_2^+ K^{*0}$ decay

In order to generate a MC sample for the $B \to a_2 K^*$ background component for the $B^+ \to a_1^+ \; K^{*0}$ analysis decay models for the longitudinal and transversal polarized $B \to a_2 K^*$ decay are needed. More information on the the used decay models is given in the `EvtGen` documentation[28]. The following `EvtGen` source code listing is used for the transversal polarized $B \to a_2^+ K^{*0}$ decay.

```
Alias MyB+ B+
Alias MyB- B-
Alias MyKstar0 K*0
```

```
Alias MyantiKstar0 anti-K*0
Alias mya_2+ a_2+
Alias mya_2- a_2-
ChargeConj mya_2+ mya_2-
#
Decay Upsilon(4S)
0.5000 MyB+ B-              VSS;
0.5000 MyB- B+              VSS;
Enddecay
#
Decay MyB+
1.0000 mya_2+ MyKstar0      HELAMP 1.0 0.0 0.0 0.0 1.0 0.0;
Enddecay
#
Decay MyB-
1.0000 mya_2- MyantiKstar0  HELAMP 1.0 0.0 0.0 0.0 1.0 0.0;
Enddecay
#
Decay mya_2+
1.0000   rho0 pi+           TVS_PWAVE 0.0 0.0 1.0 0.0 0.0 0.0;
Enddecay
#
Decay mya_2-
1.0000   rho0 pi-           TVS_PWAVE 0.0 0.0 1.0 0.0 0.0 0.0;
Enddecay
#
Decay MyKstar0
1.000 K+   pi-             VSS;
Enddecay
#
Decay MyantiKstar0
1.000 K-   pi+             VSS;
Enddecay
#
End
```

C Correlations Matrices

In this appendix the correlation matrices for the different MC input samples and the on peak dataset are shown.

C.1 Correlation Matrices for MC

Table C.1: *Correlation matrix for signal component MC sample. Longitudinal and transversal MC sample have been combined. The correlation matrix is taken from the RooRarFit output, where the configuration for the variables has the following translation:* `mES` *is* m_{ES}*,* `deltaE` *is* ΔE*,* `fisher` *is the Fisher discriminant* $\mathcal{F}$*,* `mA1` *is* m_{a_1} `mK0st` *is* $m_{K^{*0}}$ `hA1` *is* $\mathcal{H}_{a_1}$ *and* `hK0st` *is* $\mathcal{H}_{K^*}$*.*

	mES	deltaE	fisher	mA1	mK0st	hA1
deltaE	0.0036					
fisher	-0.0654	-0.0140				
mA1	-0.0763	0.0240	0.0040			
mK0st	0.0004	0.0249	0.0052	0.0038		
hA1	0.0001	-0.0024	-0.0017	-0.0011	-0.0036	
hK0st	-0.0125	0.0011	0.0028	-0.0069	0.0038	0.0036

Table C.2: *Correlation matrix for $B \to a_2 K^*$ component MC sample. Longitudinal and transversal MC sample have been combined. For more details see caption for table C.1 in this appendix.*

	mES	deltaE	fisher	mA1	mK0st	hA1
deltaE	-0.0169					
fisher	-0.0809	-0.0472				
mA1	0.0343	0.0481	0.0913			
mK0st	-0.0046	0.0027	0.0276	0.0407		
hA1	0.0108	-0.0050	0.0035	0.0437	0.0318	
hK0st	0.0049	0.0128	-0.0135	0.0582	0.0682	0.0303

Table C.3: *Correlation matrix for charmless $B\overline{B}$ background MC sample. For more details see caption for table C.1 in this appendix.*

	mES	deltaE	fisher	mA1	mK0st	hA1
deltaE	0.0814					
fisher	-0.0547	0.0022				
mA1	-0.1214	0.0428	0.0038			
mK0st	0.0185	0.0079	-0.0090	0.0110		
hA1	0.0327	0.0002	0.0179	-0.0289	-0.0122	
hK0st	-0.1019	-0.0170	-0.0040	0.0655	0.1048	0.0045

Table C.4: *Correlation matrix for charm $B\overline{B}$ background MC sample. For more details see caption for table C.1 in this appendix.*

	mES	deltaE	fisher	mA1	mK0st	hA1
deltaE	0.0240					
fisher	-0.0098	-0.0135				
mA1	-0.0063	0.0163	-0.0498			
mK0st	0.0103	0.0134	0.0146	-0.0109		
hA1	0.0124	0.0041	0.0179	0.0005	0.0192	
hK0st	-0.0108	0.0008	0.0412	-0.0564	-0.0574	-0.0109

C.2 Correlation Matrices for Data

Table C.5: *Correlation matrix for on peak dataset. This sample includes* m_{ES} *and* ΔE *signal as well as the sideband range. For more details see caption for table C.1 in this appendix.*

	mES	deltaE	fisher	mA1	mK0st	hA1
deltaE	0.0052					
fisher	-0.0200	0.0121				
mA1	0.0019	-0.0040	-0.0571			
mK0st	0.0004	-0.0058	-0.0026	-0.0251		
hA1	0.0010	0.0156	0.0118	0.0001	0.0125	
hK0st	0.0014	-0.0136	0.0142	-0.0768	0.0140	0.0100

D Summary Tables for Pure Toy Experiments

D.1 Summary tables for $f_L = 0.25$

Table D.1: *Summary table for pulls from pure toy experiments with a generated longitudinal polarization fraction $f_L = 0.25$. The pull for every toy experiment is calculated as the difference between the fitted value and the generated value. The numbers in the table are based on 500 pure toy experiments.*

Pulls	mean	sigma	mean err
deContinuum_P01	0.005 +/-0.046	1.021 +/-0.034	0.1566
f_L_Signal	0.027 +/-0.046	1.019 +/-0.033	0.0771
mA1Continuum_P01	-0.082 +/-0.046	1.028 +/-0.034	0.0180
mK0stContinuumBW_sigma	-0.031 +/-0.047	1.051 +/-0.034	0.0046
mK0stContinuumPoly_P01	-0.174 +/-0.052	1.110 +/-0.040	0.1089
nContinuum	-0.072 +/-0.046	1.016 +/-0.034	125.0572
nSignal	-0.027 +/-0.044	0.994 +/-0.032	32.4302

Table D.2: *Summary table with fitted parameter from pure toy experiments with a generated longitudinal polarization fraction $f_L = 0.25$. The numbers in the table are based on 500 pure toy experiments.*

Parameter	mean	sigma
deContinuum_P01	-2.667 +/-0.007	0.160 +/-0.005
f_L_Signal	0.247 +/-0.004	0.079 +/-0.003
mA1Continuum_P01	-0.215 +/-0.001	0.019 +/-0.001
mK0stContinuumBW_sigma	0.113 +/-0.000	0.005 +/-0.000
mK0stContinuumPoly_P01	-0.444 +/-0.005	0.110 +/-0.004
nContinuum	13307.534 +/-5.692	126.851 +/-4.177
nSignal	369.954 +/-1.446	32.308 +/-1.028

D.2 Summary tables for $f_L = 0.5$

Table D.3: *Summary table for pulls from pure toy experiments with a generated longitudinal polarization fraction $f_L = 0.5$. The pull for every toy experiment is calculated as the difference between the fitted value and the generated value. The numbers in the table are based on 500 pure toy experiments.*

Pulls	mean	sigma	mean err
deContinuum_P01	-0.016 +/-0.045	1.009 +/-0.033	0.1567
f_L_Signal	0.021 +/-0.046	1.030 +/-0.034	0.0662
mA1Continuum_P01	-0.036 +/-0.045	0.999 +/-0.033	0.0181
mK0stContinuumBW_sigma	-0.028 +/-0.047	1.039 +/-0.034	0.0046
mK0stContinuumPoly_P01	-0.127 +/-0.055	1.142 +/-0.043	0.1110
nContinuum	-0.082 +/-0.046	1.026 +/-0.034	125.0931
nSignal	-0.019 +/-0.046	1.036 +/-0.033	32.7210

Table D.4: *Summary table with fitted parameter from pure toy experiments with a generated longitudinal polarization fraction* $f_L = 0.5$. *The numbers in the table are based on 500 pure toy experiments.*

Parameter	mean	sigma
deContinuum_P01	-2.671 +/-0.007	0.158 +/-0.005
f_L_Signal	0.498 +/-0.003	0.069 +/-0.002
mA1Continuum_P01	-0.214 +/-0.001	0.018 +/-0.001
mK0stContinuumBW_sigma	0.113 +/-0.000	0.005 +/-0.000
mK0stContinuumPoly_P01	-0.439 +/-0.005	0.117 +/-0.004
nContinuum	13306.147 +/-5.777	128.174 +/-4.215
nSignal	370.202 +/-1.513	33.764 +/-1.083

D.3 Summary tables for $f_L = 0.75$

Table D.5: *Summary table for pulls from pure toy experiments with a generated longitudinal polarization fraction $f_L = 0.75$. The pull for every toy experiment is calculated as the difference between the fitted value and the generated value. The numbers in the table are based on 500 pure toy experiments.*

Pulls	mean	sigma	mean err
deContinuum_P01	-0.024 +/-0.045	0.996 +/-0.032	0.1567
f_L_Signal	0.014 +/-0.049	1.090 +/-0.035	0.0520
mA1Continuum_P01	-0.063 +/-0.043	0.960 +/-0.031	0.0181
mK0stContinuumBW_sigma	-0.004 +/-0.045	1.010 +/-0.033	0.0046
mK0stContinuumPoly_P01	-0.158 +/-0.054	1.107 +/-0.043	0.1091
nContinuum	-0.092 +/-0.045	1.002 +/-0.033	125.0706
nSignal	0.027 +/-0.044	0.980 +/-0.032	32.7944

Table D.6: *Summary table with fitted parameter from pure toy experiments with a generated longitudinal polarization fraction $f_L = 0.75$. The numbers in the table are based on 500 pure toy experiments.*

Parameter	mean	sigma
deContinuum_P01	-2.672 +/-0.007	0.156 +/-0.005
f_L_Signal	0.747 +/-0.003	0.057 +/-0.002
mA1Continuum_P01	-0.215 +/-0.001	0.017 +/-0.001
mK0stContinuumBW_sigma	0.113 +/-0.000	0.005 +/-0.000
mK0stContinuumPoly_P01	-0.447 +/-0.005	0.117 +/-0.004
nContinuum	13305.000 +/-5.618	124.956 +/-4.085
nSignal	371.551 +/-1.439	32.102 +/-1.030

Bibliography

[1] Ellis, R. K. ; Stirling, W. J. ; Webber, B. R.: *QCD and Collider Physics.* Camb. Monogr. Part. Phys. Nucl. Phys. Cosmol. 8 (1996), 1–435.

[2] Sakharov, A.D.: *Violation of CP Symmetry, C-Asymmetry and Baryon Asymmetry of the Universe.* JETP Lett. 5 (1967), 24–27.

[3] Harrison, P. F. ; Quinn, H. R.: *The BaBar physics book: Physics at an asymmetric B factory.* . – Papers from Workshop on Physics at an Asymmetric B Factory (BaBar Collaboration Meeting), Rome, Italy, 11-14 Nov 1996, Princeton, NJ, 17-20 Mar 1997, Orsay, France, 16-19 Jun 1997 and Pasadena, CA, 22-24 Sep 1997.

[4] Yao, W.-M.: *Review of Particle Physics.* J. Phys. G 33 (2006).

[5] Kramer, G. ; Palmer, W. F.: *Branching ratios and CP asymmetries in the decay $B \to VV$.* Phys. Rev. D 45 (1992), Jan, Nr. 1, 193–216.

[6] Gao, Y. ; Gritsan, A.: *Search for $B^{\pm} \to \phi K_1^{\pm}$ and $B\pm \to \phi K_2^{*\pm}$.* (2005). – BAD #1780 (*BABAR* internal analysis document).

[7] Gao, Y.: *Private communication.*

[8] Beneke, M. ; Neubert, M.: *QCD factorization for $B \to PP$ and $B \to PV$ decays.* Nucl. Phys. B675 (2003), 333–415.

[9] Ball, P. ; Braun, V. M. ; Lenz, A.: *Higher-Twist Distribution Amplitudes of the K Meson in QCD.* JHEP 0605 (2006), 004.

[10] Beneke, M. ; Buchalla, G. ; Neubert, M. ; Sachrajda, C. T.: *QCD Factorization for $B \to \pi\pi$ Decays: Strong Phases and CP Violation in the Heavy Quark Limit.* Phys. Rev. Lett. 83 (1999), 1914.

[11] Beneke, M. ; Buchalla, G. ; Neubert, M. ; Sachrajda, C. T.: *QCD Factorization for Exclusive, Non-Leptonic B Meson Decays: General Arguments and the Case of Heavy-Light Final States.* Nucl. Phys. B 591 (2000), 313.

[12] Calderon, G. ; Munoz, J. H. ; Vera, C. E.: *Nonleptonic two-body B-decays including axial-vector mesons in the final state.* Phys. Rev. D76 (2007), 094019.

[13] Aubert, B. *et al.* (*BABAR* Collaboration): *Observation of B^0 Meson Decay to $a_1(1260)^{\pm}\pi^{\mp}$.* Phys. Rev. Lett. 97 (2006), 051802.

[14] Aubert, B. *et al.* (*BABAR* Collaboration): *Evidence for charged B meson decays to $a_1(1260)^{\pm}pi^0$ and $a_1(1260)^0\pi^{\pm}$.* Phys. Rev. Lett. 99 (2007), 261801.

[15] Aubert, B. *et al.* (*BABAR* Collaboration): *Observation of B^+ Meson Decays to $a_1(1260)^+K^0$ and B^0 to $a_1(1260)^-K^+$.* Phys. Rev. Lett. 100 (2008), 051803.

[16] Cheng, H. ; Yang, K.: *Branching Ratios and Polarization in $B \to VV$, VA, AA Decays.* (2008). – hep-ph/arXiv:0805.0329.

[17] Yang, K.: *Properties of Axial-Vector Mesons and Charmless B Decays: $B \to VV$, VA, AA.* (2008). – hep-ph/arXiv:0810.1782.

[18] Bevan, A. et al.: *Search for $B^0 \to a_1^+\rho^-$.* (2005). – BAD #1132 (*BABAR* internal analysis document) VERSION 10.

[19] Lombardo, V. ; Palombo, F.: *Branching Fraction in B Meson Decay to $a_1^+\pi^-$.* (2006). – BAD #1202 (*BABAR* internal analysis document).

[20] Collins, S. et al.: *Properties of the a_1 Meson from Lattice QCD.* Phys. Rev. Lett. 74 (1995), 4596.

[21] Blatt, J.M ; Weisskopf, V.F.: *Theoretical Nuclear Physics.* John Wiley & Sons, New York, 1952.

[22] *BABAR* Run Coordinators: *BABAR Detector Operations*[1].

[23] Aubert, B. et al.: *The BABAR detector.* Nucl. Instrum. Meth. A479 (2002), 1–116.

[24] Edwards, A.: *BABAR BtaCandidate Lists*[2].

[25] Telnov, A.: *Particle ID Selectors in BABAR*[3].

[1] http://www.slac.stanford.edu/BFROOT/www/Detector/Operations/Operations.html
[2] http://www.slac.stanford.edu/BFROOT/www/doc/workbook/eventinfo/BtaCandInfo/CandLists.html
[3] http://www.slac.stanford.edu/BFROOT/www/Physics/Tools/Pid/PidSelectors

[26] Telnov, A.: *BaBar Particle ID*[4].

[27] Marchiori, G. ; Prencipe, E.: *Skims in BaBar*[5].

[28] Ryd, A. et al.: *A Monte Carlo generator for B-physics*[6]. 2001.

[29] Agostinell, S. et al.: *Geant 4 – a simulation toolkit.* Nucl. Instrum. Meth. A 506 (2003), 250–303.

[30] Bevan, A.: *Source Code see FilterTools/BToA1KstPath.tcl.* 2005.

[31] Bevan, A. et al.: *Search for* $B^0 \to a_1^+ \rho^-$. (2005). – BAD #1132 (*BaBar* internal analysis document) VERSION 1.

[32] Hulsbergen, W. D.: *Decay Chain Fitting with a Kalman Filter.* Nucl. Instrum. Meth. A 552 (2005), 566.

[33] Roat, C. ; Hulsbergen, W. D. ; Cheng, C.: *SimpleComposition User Guide*[7]. 2005.

[34] Roodman, A.: *A short description of the LH selectors*[8].

[35] Cowan, G.: *Statistical Data Analysis.* Oxford Clarendon Press: Oxford Science Publications, 1998.

[36] Blanc, F. ; Bloom, P. ; Ford, W.T. ; Smith, J.G. ; Hoek, M. V.: *Measurements of Branching Fractions and Charge and Time-Dependent asymmetries for charged and Neutral* $B \to \eta' K$ *Decays.* (2004). – BAD #490 (*BaBar* internal analysis document).

[37] Ulmer, K.A. et al.: *Branching fraction and charge asymmetry measurements in B meson Decays to* η' K *and* ω K/π *decays with run1-5 data.* (2007). – BAD #1678 (*BaBar* internal analysis document).

[38] Ulmer, K.A. et al.: *Time-Dependent CP-violating Asymmetries in B meson Decays to* η' K*. Summer 2006 Update.* (2007). – BAD #1509 (*BaBar* internal analysis document).

[4]http://www.slac.stanford.edu/BFROOT/www/Physics/Tools/Pid/pid.html
[5]http://www.slac.stanford.edu/BFROOT/www/Physics/skims/skims.html
[6]http://www.slac.stanford.edu/~lange/EvtGen
[7]http://www.slac.stanford.edu/BFROOT/www/Computing/Offline/AnalysisTools/SimpleComposition/SimpleComposition.html
[8]http://www.slac.stanford.edu/BFROOT/www/Physics/Tools/Pid/Hadrons/Description_of_the_LH_selectors.html

[39] Telnov, A.: *Changes in m_{ES} mean in Run 5 are correlated with PEP-II work*[9]. (2006).

[40] Smith, J.G.: *Private communication and HyperNews tread: m_{ES} mean and enpoint in $B \to a_1 K^*$*[10].

[41] Ritter, H. ; Martinetz, T. ; Schulten, K.: *Neuronale Netze*. Addison-Wesley, 1992.

[42] Wikipedia: The free encyclopedia: *Artificial Neural Network, Retrieved Dezember 20, 2008*[11].

[43] Roe, B.P. ; Yang, H. ; Zhu, J. ; Liu, Y. ; Stancu, I. ; McGregor, G.: *Boosted Decision Trees as an Alternative to Artificial Neural Networks for Particle Identification*. Nucl. Instrum. Meth. A 543 (2005), 577.

[44] Höcker, A. ; Stelzer, J. ; Voss, H. et al.: *TMVA Toolkit for Multivariate Data Analysis with ROOT*[12]. 2005-2008.

[45] L. Zhang: *RooRarFit - A General ML Fitting Package based on ROOT/RooFit*[13]. 2008.

[46] James, F.: *MINUIT - Function Minimization and Error Analysis - Reference Manual*[14]. 1998.

[47] Oreglia, M.J., Ph.D Thesis, SLAC-236(1980), Appendix D; Gaiser, J.E., Ph.D Thesis, SLAC-255(1982), Appendix F and Skwarnicki, T., Ph.D Thesis, DESY F31-86-02(1986), Appendix E. .

[48] Breit, G. ; Wigner, E.: *Capture of Slow Neutrons*. Phys. Rev. 49 (1936), Apr, Nr. 7, 519–531.

[49] Albrecht, H. et al.: *Search for hadronic $b \to u$ decays*. Phys. Lett. B241 (1990), 278–282.

[50] Heavy Flavor Averaging Group: *Averages of b-hadron properties at the end of 2006 and updates*[15]. 2007. – hep-ex/arXiv:0704.3575.

[9] http://babar-hn.slac.stanford.edu:5090/HyperNews/get/recoTracking/1690.html
[10] http://babar-hn.slac.stanford.edu:5090/HyperNews/get/ClHBDecays/545.html
[11] http://en.wikipedia.org/wiki/Artificial_neural_network
[12] http://tmva.sourceforge.net
[13] http://rarfit.sourceforge.net
[14] http://wwwasdoc.web.cern.ch/wwwasdoc/minuit/minmain.html
[15] http://slac.stanford.edu/xorg/hfag/osc

[51] Dickopp, M.: *Measurement of the Partial Widths Ratio $\Gamma(D_s^{*+} \to D_s^+\pi^0)/\Gamma(D_s^{*+} \to D_s^+\gamma)$ at the BABAR Experiment*. (2004).

[52] Pivk, M. ; Diberder, F. R. L.: *sPlot: A Statistical Tool to Unfold Data Distributions*. Nucl. Instrum. Meth. A 555 (2005), 356.

[53] Pivk, M. ; Diberder, F. R. L.: *sPlots*. (2003). – BAD #509 (*BABAR* internal analysis document).

[54] *BABAR* Tracking Task Force: *Tracking Efficiency for Run 1 - Run 5 in R22*[16]. 2007.

[55] Lombardo, V. ; Palombo, F.: *Private communication*.

[56] Lombardo, V. ; Palombo, F.: *Time-Dependent CP-violating Asymetries in B^0 meson decays to $a_1^\pm\pi^\mp$ and branching fraction measurements in B^0 meson decays to $a_1^\pm(1260)K^\mp$ and $B^\pm \to a_1^\pm(1260)K^0$*. (2007). – BAD #1400 (*BABAR* internal analysis document).

[57] Becker, J. et al.: *Exclusive Charmless Two-Body B^0 Decays to $\eta\prime$, $\eta\prime\pi^0$, $\eta\pi^0$ and $\omega\pi^0$*. (2008). – BAD #1772 (*BABAR* internal analysis document).

[58] Aubert, B. *et al.* (*BABAR* Collaboration): *Observation and Polarization Measurements of $B^\pm \to \phi K_1^\pm$ and $B^\pm \to \phi K_2^{*\pm}$*. Phys. Rev. Lett. 101 (2008), 161801.

[59] Olaiya, E. (for the *BABAR* Collaboration): *Measurement of Charmless $B \to VV$ decays at BaBar*. 2008. – presented at ICHEP, Philadelphia, USA.

[16]http://www.slac.stanford.edu/BFROOT/www/Physics/TrackEfficTaskForce/TrackingTaskForce-2007-R22.html

Acknowledgements

First of all I thank the head-coach Prof. Dr. Bernhard Spaan for the opportunity to write this thesis, sending me over to almost ever sunny California to work with the *BABAR* collaboration and for supervision of this work. I thank Prof. James Smith from the University of Colorado for his help at all stages of the analysis. I have to thank him for a lot of good advice. There was also a lot of input from other people, that all helped. Thanks to Yanyan Gao from the Johns Hopkins University for discussions about the two-dimensional helicity angle distributions and help with the implementation. Thanks also to Prof. Brian Meadows from the University of Cincinnati for great help concerning the a_1 mass shape. I say thanks to Dr. Armin Hauke who shares the office with me and we discussed a lot of different aspects of the analysis together. Thanks to all people from E5 for a really good atmosphere here in Dortmund. Thanks to my parents for all kind of support. Finally, thanks Judith for your love!

This work is supported by the Bundesministerium für Bildung und Forschung.